PROTEROZOIC ASSEMBLY OF NORTH AMERICA: INSIGHT FROM THE INTERACTIONS OF DEFORMATION, METAMORPHISM AND MAGMATISM IN THE SOUTHWESTERN UNITED STATES

A Dissertation

Presented to the Faculty of the Graduate School

of Cornell University

In Partial Fulfillment of the Requirements for the Degree of

Doctor of Philosophy

by

Robert Alexander Hunter

August 2013

PROTEROZOIC ASSEMBLY OF NORTH AMERICA: INSIGHT FROM THE INTERACTIONS OF DEFORMATION, METAMORPHISM AND MAGMATISM IN THE SOUTHWESTERN UNITED STATES

Robert Alexander Hunter, Ph. D.

Cornell University

One of the major goals of the geoscience community is to develop an accurate tectonic history of North America. Understanding how our continent evolved through time has numerous implications for our ability to develop accurate models of the tectonic evolution of continents – how they form, deform, and break. The interactions of deformation, metamorphism, and plutonism, three fundamental geological processes at work throughout the evolution of continents, record information that can be used to better understand the mechanisms and events that have shaped our continent. This dissertation employs metamorphic petrology, structural geology, geochemistry and geothermobarometry to interrogate the interactions of deformation, metamorphism and plutonism on multiple scales across the southwest United States.

On a microscope scale, this dissertation shows that deformation and metamorphism can work in a positive feedback loop, facilitated by solution mass transfer, to localize both deformation and metamorphism, producing areas of high strain that have more closely approached metamorphic equilibrium. This result informs our understanding of crustal behavior at mid-crustal depths during orogenesis.

On the mountain range scale, this dissertation combines petrographic analysis, structural geology, geochemistry and geothermobarometry to show that metamorphism in the Tusas and Picuris Mountains of northern New Mexico is consistent with one metamorphic event following a pressure-temperature-time trajectory consistent with progressive loading during the formation of a fold and thrust belt. This result informs our

understanding of the tectonic history of North America, and has implications for the petrogenesis of aluminosilicate triple-point rocks in the region.

Finally, on a continental scale, this dissertation uses previously published geochronologic data to identify spatial patterns in the age of igneous bodies across the southwest United States. These results were used to characterize mesoproterozoic tectonism and develop a model for melt production of these plutons. This result informs not only our understanding of crustal growth and rejuvenation during orogeny, but also provides a comprehensive dataset and novel approach that may both be employed in future research.

BIOGRAPHICAL SKETCH

Robert Alexander (“Sander”) Hunter, born in Alexandria VA, was raised in Madison WI by his parents, Robert McKinley Hunter and Karen Fonda Stowe. He has one older sister, Lorien Rachel Hunter, who currently lives in Long Beach CA while she pursues her PhD in sociology. Robert completed his B.S. in geology at the University of Wisconsin, Madison. During his time there, he worked with Professor Basil Tikoff to determine the structural significance of magma conduits between plutonic intrusions in the Henry Mountains of Utah.

After completing his B.S., Sander began working towards a PhD at Cornell University under professor Chris Andronicos. During his time at Cornell, Sander participated in the graduate student community by taking multiple roles, including president and faculty liaison in the department’s graduate organization, while also acting as treasurer of AAPG for a short period. He also helped to found a chapter of the Society for the Advancement of Native Americans and Chicanos in the Sciences at Cornell, where he again acted as treasurer.

Outside the academic realm, Sander spent his time at Cornell exploring the nature surrounding the University. Through this outlet, he developed an interest in photography, entering several local contests, selling his prints and working as an event photographer. Sander has accepted position as a research scientist with Royal Dutch Shell in Houston, Texas, where he hopes to continue both academic research and amateur photography.

ACKNOWLEDGMENTS

The list of people I wish to thank for helping me achieve my goals is quite long and extends back to a time long before my arrival at Cornell. However, first and foremost, I would like to thank my committee, Professors Christopher Andronicos, Robert Kay, and Karim-Aly Kassam. Professor Kassam, thank you for your willingness to teach me about human ecology. Each discussion with you pushed me to think in completely new ways and challenged me to see things from a different perspective. Professor Kay, thank you for always finding the time to meet with me. Your support throughout my time here, and particularly recently with Chris at another university, has been instrumental in getting me to where I am today. And finally, Chris, thank you. For everything. You took me in, quite literally, out of the cold, and helped me feel at home. And for that, I am endlessly grateful. My experience with you led me to Cornell, and since that time, you have worked hard to leave your boot print on my geological soul – in the best possible way.

Chris, you have shared with me your passion for geology, as well as your endless knowledge on the subject. But my learning did not stop with geology. Over my time at Cornell, I'm pretty sure you taught me something about just about everything: from tarp science, to how to hang a bear bag and how to survive a thundersnow storm at 12,000 feet; from how to tell sillimanite from wollastonite to how to identify graded beds in an amphibolite facies grade pelitic schist. You have had my back every step of the way. Thank you.

I would like to thank my fellow graduate students and friends. I never dreamt I would have such a great group of diverse, caring and fun friends. I would like to thank

you all for the late night G-chat consultations, programming help, pizza Fridays and innumerable other fond memories. I would be remiss if I did not specifically thank a few of you specifically. First, I would like to thank my officemate Ruth Aronoff. From late night office dance party breaks and G-chatted words of support to a long list of inside jokes…I don't know I would have done without you. Second, I would like to thank Greg Kirkpatrick and Scott Henderson. When the chips were down and I was in dire need of help, you guys never let me down. Finally, I would like to thank Kyle Trostle and Gregg McElwee. You two made sure I got out of the office to see the sun, at least for as long as it takes to walk to the Souvlaki House. You two are amazing friends. Thank you.

The importance of my family to my success at Cornell cannot be overstated. Mom and Dad, I would like thank you for always believing in me, encouraging me, and giving me places to call home. To my sister Lorien, thank you. No matter what you were doing, or when I called, you have always been there for me, and have always cheered me on. And no, the "you're a rock star" joke never gets old.

Reaching back to my time before graduate school, I would like to think my undergraduate advisor, Professor Basil Tikoff, and my boss at the University of Wisconsin Madison Geology Museum, both of whom were instrumental in my success as an undergraduate, and both of whom helped me reach Cornell. Also from my time as an undergraduate, I would like thank Mercile Lee, whose grace, wisdom and belief in me saw me through some of my most difficult times.

Finally, I would also like to thank the National Science Foundation and the Diversity Programs in Engineering here at Cornell, both of whom funded me during my quest for knowledge in the form of fellowships.

TABLE OF CONTENTS

LIST OF FIGURES

LIST OF TABLES

1. Introduction

Research Question

Understanding how continents evolve through time has wide-reaching impacts. Developing an accurate tectonic model for the growth of a continent, such as North America, through time requires an understanding of both small scale details that must be observed on a microscopic scale, as well as broad trends and patterns that require observations on the continent-scale. Orogenesis, one of the major processes by which continents grow, is complex, with deformation, metamorphism, and plutonism all taking active roles in reshaping the continent. Mountain building during orogeny produces thickened crust, which involves significant deformation, and produces both metamorphism and plutonism. Thus, careful study of these aspects of orogeny can be used to improve our understanding of not only the mechanics of orogenesis, but also the tectonic history of the orogen being studied (Karlstrom and Williams, 1995).

Understanding the tectonic history of a region may be addressed using many different approaches including metamorphic petrology (e.g. Grambling 1981, 1986; Williams, 1991; Grambling and Dallmeyer, 1993; Karlstrom and Williams, 1996; Williams *et al.*, 1999; Daniel and Pyle, 2006; Barnhart *et al.*, 2012), determination of detrital provenance (e.g. Vigneresse, 2005; Jones *et al.*, 2009, 2011; Doe *et al.*, 2012; Daniel *et al.*, in press), metamorphic geochronology (e.g. Shaw *et al.*, 2001; Daniel and Pyle, 2006; Wolf *et al.*, 2010; Aronoff *et al.*, 2012), igneous geochronology (e.g. Silver, 1965; Silver *et al.*, 1977; Condie, 1981, 1982, 1986), crustal model ages (e.g. DePaolo, 1981; Bennett and DePaolo, 1987), and structural geology (e.g. Karlstrom and Bowring,

1988, 1993; Karlstrom and Daniel, 1993; Karlstrom and Williams, 1995) among others. The key questions that must be addressed when characterizing orogenesis include when it happened, where it happened, and how it happened. The question of when may be addressed directly by geochronology, or indirectly by detrital provenance or cross cutting relationships. The question of where it happened can be addressed by geochronology, structural geology, geophysics, geochemistry or metamorphic petrology. The question of how it happened may be addressed by geochemistry, geophysics, structural geology, or petrology.

The focus of this dissertation is to use the interactions of deformation, metamorphism and plutonism to improve our understanding of the evolution of Proterozoic North America. This is accomplished by combining geochemistry, structural geology, petrology and geochronology on a variety of scales. On the microscopic scale, I use metamorphic petrology, structural geology and geochemistry to characterize the interactions of metamorphism and deformation during plutonic emplacement. On the mountain range scale, I use geochemistry, petrology, structural geology and geothermometry to determine the pressure-temperature-time history of the mountain belt and corroborate a tectonic model for orogenesis. On the continent scale, I use previously published geochronologic and structural data to determine the location of a tectonic boundary and develop a model for plutonic melt production.

Why the southwest United States

The southwestern United States provides an ideal natural laboratory for learning how continents evolve. Composed of a Proterozoic crustal mosaic of distinct juvenile crustal terranes, the region preserves a uniquely complete history of the interactions of

deformation, metamorphism and plutonism that worked in concert during crustal growth. The perforation of this swath of accretionary crust by igneous plutons during orogeny provides a unique record of syntectonic deformation (e.g. Kirby *et al.*, 1995; Karlstrom and Williams, 1995; Nyman *et al.*, 1997). Furthermore, the region has been the subject of extensive research in the geologic community, providing a wealth of information that may be incorporated and applied to new questions and techniques (e.g. Vigneresse, 2005; Goodge and Vervoort, 2006).

Not only is this region ideal for the reasons outlined above, but also for the vast quantity of research that has previously been conducted in the area. Researchers have shown that the growth of Laurentia during the Proterozoic by lateral accretion of off-board terranes is widely accepted as the mechanism for continental growth of North America (e.g. Silver, 1965, 1968; Condie, 1981, 1982, 1987; Bennett and DePaolo, 1987; Karlstrom and Bowring, 1988, 1993; Karlstrom and Daniel, 1993; Shaw and Karlstrom, 1999; Aleinikoff *et al.*, 1993; Magnani *et al.*, 2004; Figure 1-1). These terranes accreted along the southern margin of Laurentia, beginning at ~2 Ga, and growing southward until ~1 Ga. This belt of juvenile continental crust spans more than 1000 km, comprising the majority of the crust in the western United States. Between ~1900 and ~1200 Ma, this evolving crustal mosaic experienced ubiquitous plutonism, with a notable gap in plutonism between 1600 and 1500 Ma, and an episode of voluminous A-type, or Ferroan, magmatism at ~1400 Ma (Anderson, 1983; Shaw and Karlstrom, 1999; Frost and Frost, 2011; Condie, 2012). Although this geologic history shows the impressive knowledge accumulated in the scientific community about Proterozoic North America, outstanding questions remain, and on-going controversies highlight the need for further research.

Finally, the southwestern United States is an ideal natural laboratory because Proterozoic mid-crustal rocks, preserving a record of deformation and metamorphism associated with continent building orogenic events, have been brought to the surface by subsequent uplift with minimal overprinting of fabrics and petrologic textures. Furthermore, the exposure of these units is exceptional because of the rugged landscape and relatively arid climate.

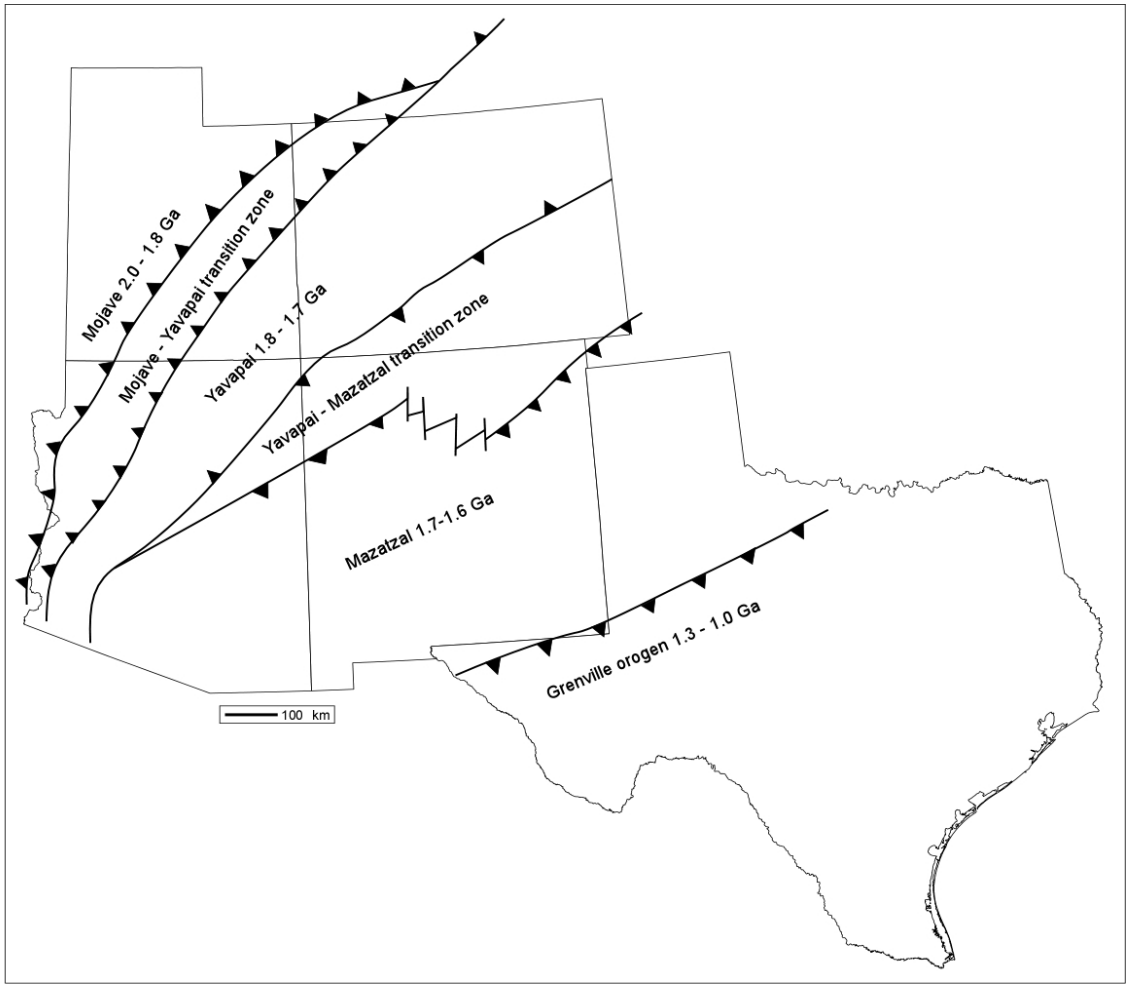

Figure 1-1: A schematic map of the southwest United States showing proposed tectonic boundaries (modified from Shaw and Karlstrom, 1999).

Dissertation Outline

The research presented herein uses deformation, metamorphism and magmatism to improve our understanding of the Proterozoic assembly of North America on multiple scales of magnitude. Each chapter represents an individual manuscript that has been or will be submitted for peer-reviewed publication. The first chapter, *Deformation assisted phase transformation: an example from the sillimanite-in isograd, Eolus batholith, Needle Mountains, Colorado, USA* (Hunter and Andronicos, 2012), addresses the question of how supracrustal rocks partition deformation.

During plutonism, significant strain must be locally accommodated in order to make space for the igneous body. Furthermore, such events are associated with localized metamorphism, producing metamorphic contact aureoles around the intrusion. The interactions of this deformation and metamorphism are central to understanding how crustal rheology changes during plutonism and orogenesis.

Done on the microscopic scale, this chapter presents petrologic, microstructural and geochemical observations linking deformation and prograde metamorphism to strain localization through solution mass transfer in the metamorphic contact aureole around the Eolus Granite in the Needle Mountains, Colorado. Within the contact aureole of the Eolus Granite, outcrops of aluminous schist in the Vallecito Conglomerate locally contain both andalusite and sillimanite. Low strain areas contain both aluminosilicates; however, high strain zones, defined by shear bands of sillimanite, contain almost no andalusite. An isocon analysis (after Gresens, 1967; Grant, 1986) comparing high and low strain sample shows two key observations. First, the ratio of immobile elements between the deformed

and undeformed sample suggest that they have a chemically similar protolith. Second, this same isocon analysis suggests that the deformed sample experienced significant mass loss during deformation and metamorphism. Furthermore, several key petrologic observations lend insight into the mechanism that produced sillimanite-rich shear bands. The first observation is the presence of epitaxial sillimanite in muscovite (e.g. Kerrick, 1990). The second observation is the presence of muscovite overgrowths around andalusite. These observations coupled with the fact that the abundance of muscovite is low in shear bands suggests a Carmichael (1969) type series of reactions produced a net reaction of sillimanite after andalusite through reactions involving the production of muscovite after andalusite in low strain regions, and the production of sillimanite after muscovite in high strain regions. To facilitate this series of reactions we recall the observation that significant mass was lost from the high strain sample, and suggest that the replacement of muscovite by sillimanite produced a solution, used to transport material away from high strain regions, locally producing muscovite in lower strain regions. Finally, we note that the fact that sillimanite is the defining mineral in shear bands implies that sillimanite needle aggregates localized strain during deformation, while at the same time continued metamorphism is localized to regions of high strain, facilitating further sillimanite growth, essentially a reaction softening mechanism (e.g. Vernon, 1987; Goergen *et al.*, 2008). Results of this study show that deformation and metamorphism worked in concert, enhancing both strain localization and metamorphism by locally changing the whole rock chemistry through solution mass transfer.

Looking more macroscopically at mountain ranges in northern New Mexico, the second chapter of this dissertation, *Metamorphic P-T paths across the Al_2SiO_5 triple*

point terrane of northern New Mexico, USA: Metamorphic Constraints on Orogeny in Southern Laurentia, presents petrologic, textural, geochemical and microstructural observations in the Tusas and Picuris Mountains, in an effort to characterize the observed metamorphism and develop a tectonic model for the region. Understanding the nature of metamorphism in these mountain ranges is central to the Proterozoic tectonic history of the southwest United States (e.g. Grambling, 1981, 1986; Williams, 1991; Grambling and Dallmeyer, 1993; Karlstrom and Williams, 1996; Shaw and Karlstrom, 1999; Williams *et al.*, 1999; Shaw *et al.*, 2005; Daniel and Pyle, 2006; Barnhart *et al.*, 2012; Aronoff *et al.*, 2012; Hunter *et al.*, 2012). Having been a subject of debate for over thirty years, the characteristics of this metamorphism contain information about the mechanisms that produced it, holding key details for developing a tectonic history of the area (Grambling 1981, 1986; Williams, 1991; Karlstrom and Williams, 1996; Daniel and Pyle, 2006; Grambling and Dallmeyer, 1993; Williams *et al.*, 1999; Shaw *et al.*, 2005; Aronoff *et al.*, 2012; Barnhart *et al.*, 2012). Some researchers have proposed a poly-metamorphic history for the region, involving initial metamorphism at ~1.7 Ga, followed by a thermal excursion and metamorphic overprinting at ~1.4 Ga (e.g. Karlstrom and Williams, 1996). However, other researchers (e.g. Grambling, 1981; Daniel and Pyle, 2006) have proposed that the observed metamorphism is the result of a single metamorphic event at ~1.4 Ga.

In this study, we combine petrologic and textural observations, isochemical phase diagrams, garnet-biotite geothermometry and a compilation of mapped metamorphic isograds to determine the pressure-temperature-time (P/T/t) history of Proterozoic northern New Mexico (Figure 1-2). Results of this study show that, although all areas in the Picuris and Tusas Mountains experienced clockwise prograde metamorphism, the P/T

conditions of this metamorphism varied systematically across the region. This metamorphism overprints thrust faulting in the area, and metamorphic isograds reflect this gradient in metamorphic conditions, supporting an interpretation of this metamorphism as a result of a single metamorphic event. The P/T/t paths developed through petrographic observations and geochemical modeling are consistent with progressive loading during the development of a fold and thrust belt (e.g. England and Thompson, 1984; Beaumont *et al.*, 2001), supporting the proposed tectonic model of Aronoff *et al.* (2012). Furthermore, these results support a metamorphic history involving a single episode of metamorphism, again consistent with the results of Aronoff *et al.* (2012).

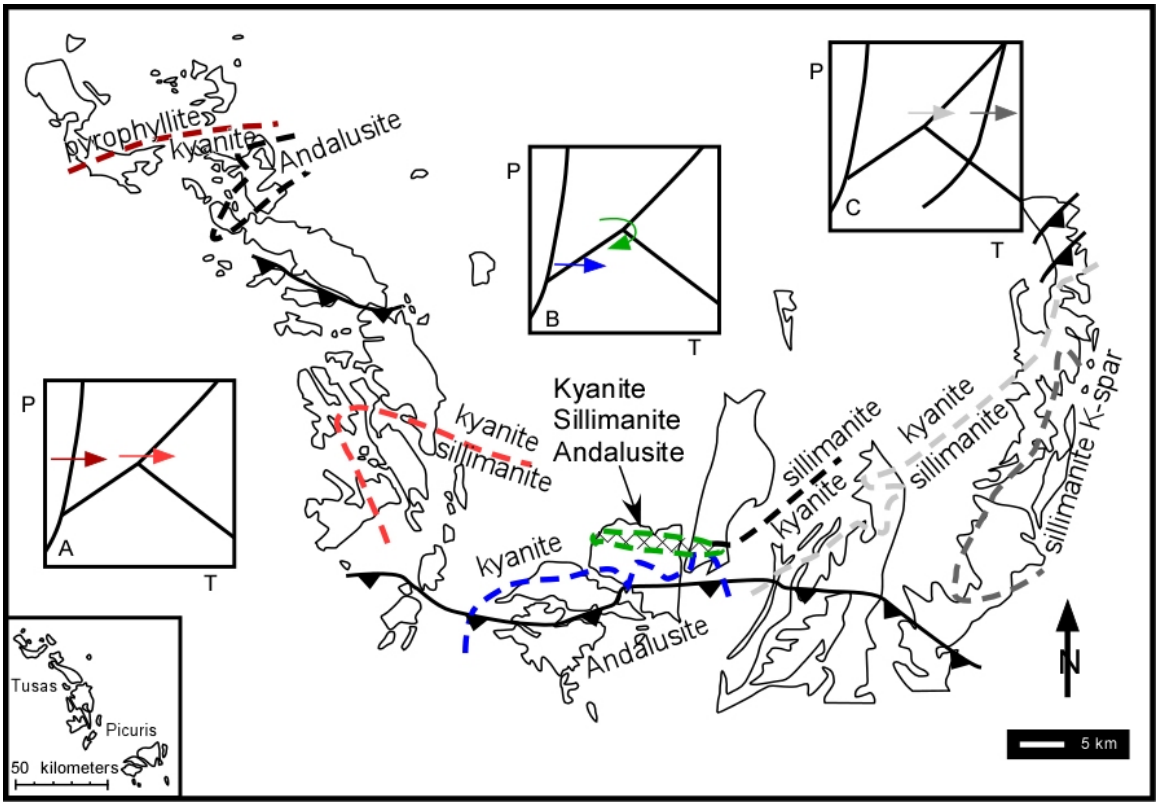

Figure 1-2: A tracing of the reconstructed Proterozoic belt in Northern New Mexico. Aluminosilicate isograds are shown with heavy dashed lines. The color of these isograds is used to correlate the transition with related arrows on inlaid schematic PT diagrams (A, B, C). In the schematic PT diagram (A), the dark red arrow represents the transitions in the northern Tusas from pyrophyllite to kyanite (Williams et al., 1999), and kyanite to andalusite. The orange arrow in (A) represents the transition in the south-central Tusas from kyanite to sillimanite. In the schematic PT diagram (B), the blue arrow represents the transition in the central Picuris from kyanite to andalusite. The green arrow represents metamorphism passing through the aluminosilicate triple point. In the same schematic PT diagram, the black arrow with dashed lines represents the PT path determined for the northern Picuris by Daniel and Pyle (2006). Finally, in the area of the Rio Mora uplift in the east, the schematic PT diagram (C), the light gray arrow corresponds to the transition from kyanite to sillimanite, while the dark gray arrow corresponds to the second sillimanite isograd, producing sillimanite + potassium feldspar assemblages (Read et al., 1999).

Again looking macroscopically at the entire southwestern United States, the third chapter of this dissertation, *Tectonic implications of Proterozoic U/Pb crystallization ages in the southwestern United States,* uses a compilation of previously published geochronologic data to evaluate spatial trends in pluton emplacement through time. These trends are assessed through the lens of the recently revised tectonic model for Proterozoic Laurentia that includes a ~1.4 Ga orogenic event as described in the preceding chapter. During the Paleo and Mesoproterozoic, the region that is now the southwestern United States experienced multiple pulses of magmatism – first between 1.8 and 1.7 Ga, then again between 1.7 and 1.6 Ga, and finally between 1.5 and 1.4 Ga. These plutons comprise a significant portion of the crust in the southwestern United States, regionally making up 20-30% of the crust by volume (Anderson, 1983). Interestingly many of these plutons that are between 1.4 and 1.5 Ga in age have been categorized as A-type based on their chemistry (Loiselle and Wones, 1979; Anderson, 1983; Anderson and Bender 1989; Eby, 1990; Gonzales, 1997; Smith et al., 1999; Goodenough et al., 2000; Dall'Agnol and Oliveira, 2007). Although generation of A-type melt is usually linked to secondary differentiation from basaltic melt and production in extensional settings, structural evidence shows significant evidence for a contractional tectonic regime during their emplacement (Nyman et al., 1994; Kirby et al., 1995; Duebendorfer and Christensen, 1995; Karlstrom and Williams, 1995; Nyman et al., 1997; Ferguson et al., 2004). While multiple models have been proposed to explain these seemingly contradictory lines of evidence, the origins of these ~1.4 Ga A-type plutons remains controversial.

In this chapter, we combine previously published geochronologic studies to estimate the northern extent of the orogenic event described in chapter 2. Furthermore, we compile previously published U/Pb zircon crystallization ages from across Arizona, New Mexico and Colorado to and evaluate spatial trends of ages within this dataset relative to the orogenic event (Figure 1-3). Two groups of plutons are readily apparent within the dataset: an older group of ages over 1600 Ma, and a younger group of data, with ages under 1500 Ma. Looking specifically at the older group of ages, a trend of decreasing age to the southeast is present; however, we identify two populations, whose linear regressions have similar slopes, but are separated by an offset in their y-intercept, or age. This break between these two populations is identified to be at 15 km southeast of the orogeny, and is interpreted as a zone of localized shortening along the northern extent of the orogenic belt.

Focusing on the plutons under 1500 Ma, it is clear that there is a clustering in ages: one set between 1400 and 1500 Ma, and a younger set, separated by a ~25 Ma gap in age that spans a large range in ages. The set of ages between 1400 and 1500 Ma decreases in age to the northwest with a very shallow slope relative to the orogeny. Compositionally, these plutons are predominately A-type. Although numerous mechanisms have been proposed to explain production of these melts, rapid burial, required by new detrital zircon (Jones et al., 2011; Doe et al., 2012; Daniel et al., in press) and Lu/Hf garnet dating (Aronoff et al., 2012; Hunter et al., 2012) evidence, and crustal thickening, consistent with the recent identification of an regional orogenic event, suggest that this A-type magmatic event is the result of crustal thickening and thermal relaxation (e.g. Thompson, 1999).

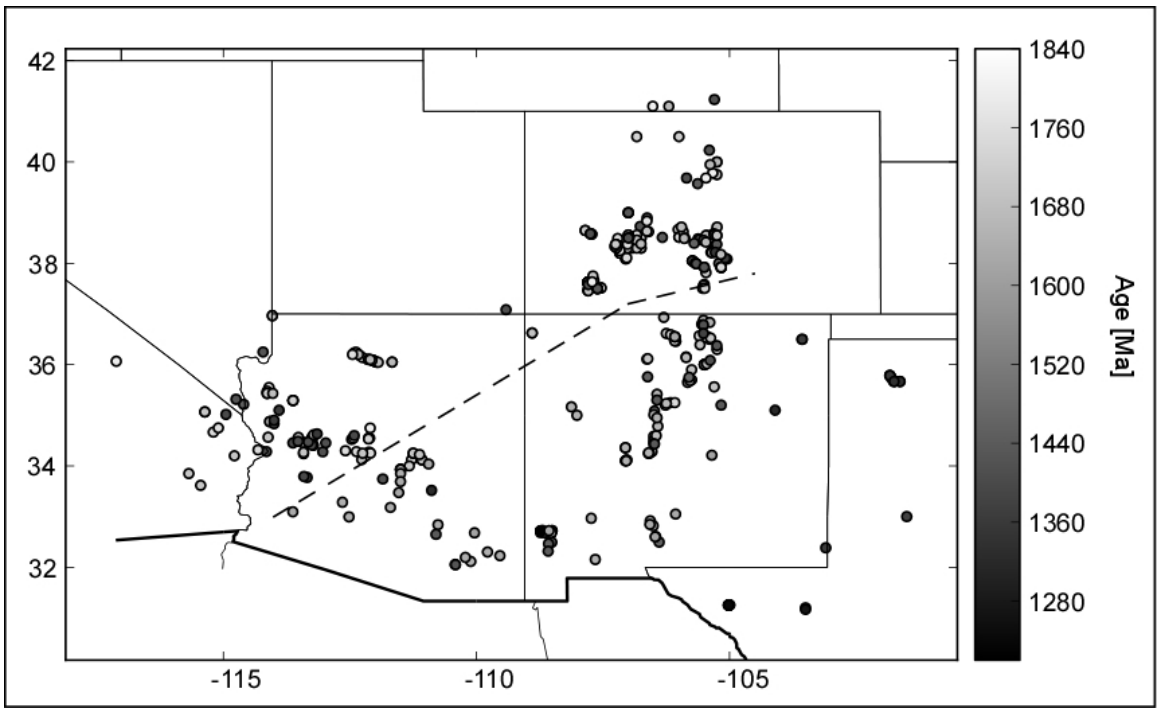

Figure 1-3: A schematic map of the southwestern United States. Shown dashed in black is our estimated location of the Picuris Orogeny as constrained by ~1.4 Ga basins and ~1.4 Ga metamorphism. Circles represent Proterozoic plutons with reported U/Pb zircon crystallization ages, where gray scale of each sample corresponds to the age of that pluton with darker colors representing younger ages.

Dissertation Conclusions

This dissertation provides insight into orogenic processes, and the orogenic history of the southwest United States through studies of deformation, metamorphism and magmatism. The three studies described herein cover a vast spectrum of scales – from micrometers to thousands of kilometers – impacting to our current understanding of crustal deformation, the tectonic evolution of North America, and methodologies for approaching continent-scale questions with existing data.

On the microscopic scale, I show that deformation and metamorphism can work together in a feedback loop to localize both processes and locally helping the reaction volume approach metamorphic equilibrium. Furthermore, I show that this process can produce significant volume loss and that it is facilitated by solution mass transfer. This study informs our understanding of how strain can be localized during prograde metamorphism related, and more generally, how the crust can behave and deform during orogenesis.

On the Mountain range scale, I show that metamorphism in the Tusas and Picuris Mountains followed clockwise pressure-temperature-time paths and that metamorphic isograds across this region record a continue gradient in P/T conditions. I assert that the characteristics of this metamorphism are consistent with a single, progressive metamorphic event and that the trajectory of metamorphism across both the Tusas and Picuris Mountains is consistent with progressive loading in a fold and thrust belt. This study is significant for several reasons. First, along with the work of Aronoff *et al.* (2012) and Daniel *et al.*, (2012, in press), these results help to clarify the tectonic history of the region by showing that only one orogenic event, at ~1.4 Ga (Aronoff *et al.*, 2012; Daniel

et al., 2012, in press), occurred in the study area. Second, this study is significant because it shows that triple point assemblages within the study (e.g. Holdaway, 1978; Grambling, 1981; Holdaway and Goodge, 1990) are the result of this same single metamorphic event, and locally represent equilibrium triple point assemblages.

On the largest scale, I show that it is possible to identify the location of tectonic boundaries and characterize the nature of plutonism on a regional scale by analyzing trends in compiled, previously published geochronologic data. In my study, I use previously published detrital zircon (Jones et al., 2011; Doe et al., 2012; Daniel et al., in press) and Lu/Hf garnet (Aronoff et al., 2012) geochronology studies to estimate the northern extent of the Picuris Orogeny across New Mexico, Colorado and Arizona. I then compile Proterozoic igneous U/Pb zircon crystallization ages from Arizona, New Mexico and Colorado, and measure the distance between each sample and the estimated northern extent of the orogeny. Through this exercise, I identify a zone of shortening that coincides with the northern extent of the orogenic belt as inferred from detrital zircon and Lu/Hf garnet age data, and show that 1400-1500 Ma plutons in the region were emplaced relatively contemporaneously across the region. From these results, we propose a model for their melt production that invokes thermal relaxation of over thickened crust to introduce the heat necessary to yield the A-type chemistries observed in the ~1.4 Ga magmatic event.

In summary, this dissertation highlights the importance and utility of studying the interactions of deformation, metamorphism and plutonism with three studies on varying scale. Each study described herein uses different approach; however, the results of all of

these studies impact our understanding of the evolution of North America and the orogenic process.

References:

Aleinikoff, J.N., Reed, J.C., Jr., Wooden, J.L., 1993. Lead isotopic evidence for the origin of Paleo- and Mesoproterozoic rocks of the Colorado province, U.S.A.. Precambrian Research 63, 97–122.

Anderson, J.L., 1983. Proterozoic inorganic granite plutonism of North America. Geological Society of America Memoir 161, 133–154.

Anderson, J. L., Bender, E. E., 1989. Nature and origin of Proterozoic A-type granitic magmatism in the southwestern United States of America. Lithosphere 23, 19–52.

Aronoff, R.F., Vervoort, J.D., Andronicos, C.L., Hunter, R.A., 2012. Lu-Hf garnet geochronology and microstructural analysis constrain the timing of crustal assembly in southwestern North America. Geological Society of America Abstracts with Programs 44 (7), 525.

Barnhart, K.R., Walsh, P.J., Hollister, L.S., Daniel, C.G., Andronicos, C.L., 2012. Decompression during Late Proterozoic Al_2SiO_5 Triple-Point Metamorphism at Cerro Colorado, New Mexico. The Journal of Geology 120, 385–404.

Beaumont, C., Jamieson, R.A., Nguyen, M.H., Lee, B., 2001. Himalayan tectonics explained by extrusion of a low-viscosity crustal channel coupled to focused surface denudation. Nature 414, 738–742.

Bennett, V.C., DePaolo, D.J., 1987. Proterozoic crustal history of the western United States as determined by neodymium isotopic mapping. Geological Society of America Bulletin 99, 647–685.

Carmichael, D.M., 1969. On the mechanism of prograde metamorphic reactions in quartz-bearing pelitic rocks. Contributions to Mineralogy and Petrology 20, 244–267.

Condie, K.C., 1981. Precambrian rocks of the southwestern United States and adjacent areas of Mexico: New Mexico Bureau of Mines and Mineral Resources Resource Map 13, scale 1:1,500,000, 2 sheets.

Condie, K.C., 1982. Plate-tectonics model for Proterozoic continental accretion in the southwestern United States. Geology 10, 37–42.

Condie, K.C., 1986. Geochemistry and tectonic setting of Early Proterozoic supracrustal rocks in the southwestern United States. Journal of Geology 94, 845–864.

Condie, K.C., 1987. Early Proterozoic volcanic regimes in southwestern North America. *In*: Pharaoh, T.C., Beckinsale, R.D., and Rickard, D. (Eds.), Geochemistry and mineralization of Proterozoic volcanic suites: Geological Society [London] Special Publication 33, 211–218.

Condie, K.C., 2012. Nune to Rodinia: Preservation and recycling of continental crust. Geological Society of America Abstracts with Programs 44 (7), 293.

Dall'Agnol, R., Oliveira, D.C., 2007. Oxidized, magnetite-series, rapakivi-type granites of Carajás, Brazil: implications for classification and petrogenesis of A-type granites. Lithosphere 93, 215–233.

Daniel, C.G., Pfeifer, L.S., Jones, J., McFarlane, C., in press. Detrital zircon evidence for non-Laurentian provenance, Mesoproterozoic (ca. 1490–1450 Ma) deposition and orogenesis in a reconstructed orogenic belt, northern New Mexico, USA: defining the Picuris Orogeny. Geological Society of America Bulletin.

Daniel, C.G., Pyle, J, 2006. Monazite-Xenotime Thermochronometry and Al_2SiO_5 Reaction Textures in the Picuris Range, Northern New Mexico, USA: New Evidence for a 1450-1400 Ma Orogenic Event. Journal of Petrology 47, 97–118.

DePaolo, 1981. Neodymium isotopes in the Colorado Front Range and crust-mantle evolution in the Proterozoic. Nature 291, 193–196.

Doe, M.F., Jones, J.V. III, Karlstrom, K.E., Thrane, K., Frei, D., Gehrels, G., Pecha, M., 2012. Basin formation near the end of the 1.60–1.45 Ga tectonic gap in southern Laurentia: Mesoproterozoic Hess Canyon Group of Arizona and implications for ca. 1.5 Ga supercontinent configurations. Lithosphere 4, 77–88

Duebendorfer, E.M., Christensen, C., 1995. Synkinematic (?) intrusion of the "anorogenic" 1425 Ma Beer Bottle Pass pluton, southern Nevada. Tectonics 14, 168–184.

Eby, G. N., 1990. The A-type granitoids: A review of their occurrence and chemical characteristics and speculations on their petrogenesis. Lithosphere 26, 115–134.

England, P.C., Thompson, A.B., 1984. Pressure-Temperature-Time Paths of Regional Metamorphism I. Heat Transfer during the Evolution of Regions of Thickened Continental Crust. Journal of Petrology 25, 894–928.

Ferguson, C.B., Duebendorfer, E.M., Chamberlain, K.R., 2004. Synkinematic Intrusion of the 1.4-Ga Boriana Canyon Pluton, Northwestern Arizona: Implications for Ca.

1.4-Ga Regional Strain in the Western United States. The Journal of Geology 112, 165–183. Journal of Petrology 52, 39–53.

Frost, C.D., Frost, B.R., 2011. On ferroan (A-type) granites: their compositional variability and modes of origin. Journal of Petrology 52, 39–53.

Goergen, E.T., Whitney, D.L., Zimmerman, M.E., Hiraga, T., 2008. Deformation-induced polymorphic transformation: experimental deformation of kyanite, andalusite and sillimanite. Tectonophysics 454, 23–35.

Goodenough, K.M., Upton, B.G.J., Ellam, R.M., 2000. Geochemical evolution of the Ivgtut granite, South Greenland: a fluorine-rich 'A-type' intrusion. Lithosphere 51, 205–221.

Goodge, J.W., Vervoort, J.D., 2006. Origin of Mesoproterozoic A-type granites in Laurentia: Hf isotope evidence. Earth and Planetary Science letters 243, 711–731.

Gonzales, D.A., 1997. Crustal evolution of the Needle Mountains Proterozoic complex, Southwestern Colorado. Doctoral Dissertation. University of Kansas, Lawrence, Kansas, p. 190.

Grant, J.A., 1986. The isocon diagram–a simple solution to Gresens' equation for metasomatic alteration. Economic Geology 81, 1976–1982.

Grambling, J. A., 1981. Kyanite, andalusite, sillimanite, and related mineral assemblages in the Truchas Peaks region, New Mexico. American Mineralogist 66**,** 702–722.

Grambling, J. A., 1986. Crustal thickening during Proterozoic metamorphism and deformation in New Mexico. Geology 14, 149 –152.

Grambling, J. A., Dallmeyer, R. D., 1993. Tectonic evolution of Proterozoic rocks in the Cimarron Mountains, northern New Mexico, USA. Journal of Metamorphic Geology 11, 739 –755.

Gresens, R.L., 1967. Composition–volume relationships of metasomatism. Chemical Geology 2, 47–65.

Holdaway, M. J., 1978. Significance of chloritoid-bearing andstaurolite-bearing rocks in the Picuris Mountains, New Mexico. Geological Society of America Bulletin 89, 1404–1414.

Holdaway, M. J., Goodge, J. W., 1990. Rock pressure vs. fluid pressure as a controlling influence on mineral stability: an example from New Mexico. American Mineralogist 75, 1043 –1058.

Hunter, R.A., Andronicos, C.L., 2012. Deformation assisted phase transformation: an example from the sillimanite-in isograd, Eolus batholith, Needle Mountains, Colorado, USA. Terra Nova 25 (1), 48–56.

Hunter, R.A., Andronicos, C.L., Vervoort, J.D., Aronoff, R.F., 2012. Refining the Proterozoic history of North America through combined use of Lu-Hf geochronology and Petrologic Analysis. Geological Society of America Abstracts with Programs 44 (7), 526.

Jones, J.V., Connelly, J.N., Karlstrom, K.E., Williams, M.L., Doe, M.F., 2009. Age, provenance, and tectonic setting of Paleoproterozoic quartzite successions in the southwestern United States. Geological Society of America Bulletin 121, 247–264.

Jones, J.III, Daniel, C. G., Frei, D., Thrane, K., 2011. Revised regional correlations and tectonic implications of Paleoproterozoic and Mesoproterozoic metasedimentary rocks in northern New Mexico, USA: New findings from detrital zircon studies of the Hondo Group, Vadito Group, and Marqueñas Formation. Geosphere 7, 974–991.

Karlstrom, K.E., Bowring, S.A., 1988. Early Proterozoic assembly of tectonostratigraphic terranes in southwestern North America. Journal of Geology 96, 561–576.

Karlstrom, K.E., Bowring, S.A., 1993. Proterozoic orogenic history of Arizona, *in* Van Schmus, W.R., Bickford, M.E., and 23 others, Transcontinental Proterozoic provinces. *In* Reed, J.C., Jr., and 6 others (Eds.), Precambrian: Conterminous U.S.: Boulder Colorado, Geological Society of America, The Geology of North America C-2, 188–211.

Karlstrom, K.E., Daniel, C.G., 1993. Restoration of Laramide right-lateral strike slip in northern New Mexico by using Proterozoic piercing points; tectonic implications from the Proterozoic to the Cenozoic. Geology 21, 1139–1142.

Karlstrom, K.E., Williams, M.L., 1995. The case for simultaneous deformation, metamorphism and plutonism: an example from Proterozoic rocks in central Arizona. Journal of Structural Geology 17 (1), 51–81.

Karlstrom, K.E., Williams, M.L., 1996. Looping *P-T* paths and high-*T*, low-*P* middle crustal metamorphism: Proterozoic evolution of the southwestern United States. Geology 24, 1119–1122.

Kerrick, D.M., 1990. The Al_2SiO_5 Polymorphs. Mineralogical Society of America Reviews in Mineralogy, 22.

Kirby, E., Karlstrom, K. E., and Andronicus, C., 1995. Tectonic setting of the Sandia pluton: an orogenic 1.4 Ga granite in New Mexico. Tectonics 14, 185–201.

Loiselle, M.C., Wones, D., 1979. Characteristics and origin of anorogenic granites. Geological Society of America, Abstracts with Programs 11, 468.

Magnani, M.B., Miller, K.C., Levander, A., Karlstrom, K., 2004. The Yavapai-Mazatzal boundary: A long-lived tectonic element in the lithosphere of southwestern North America. Geological Society of America Bulletin 116 (9-10), 1137–1142.

Nyman, M.W., Karlstrom, K.E., Kirby, E., Graubard, C.M., 1994. Mesoproterozoic contractional orogeny in western North America: evidence from 1.4 Ga plutons. Geology 22, 901–904.

Nyman, M.W., Karlstrom, K.E., 1997. Pluton emplacement processes and tectonic setting of the 1.42 Ga Signal batholith, SW USA: important role of crustal anisotropy during regional shortening. Precambrian Research 82, 237–263.

Read, A., Karlstrom, K. E., Grambling, J. A., Bowring, S. A., Heizler, M., Daniel, C., 1999. A mid-crustal cross section from the Rincon Range, northern New Mexico: Evidence for 1.68 Ga pluton-influenced tectonism and 1.4 Ga regional metamorphism. Rocky Mountain Geology 34, 67–91.

Shaw, C.A., Karlstrom, K.E., 1999. The Yavapai- Mazatzal crust boundary in the Southern Rocky Mountains. Rocky Mountain Geology 34 (1), 37–52.

Shaw, C.A., Heizler, M.H., Karlstrom, K.E., 2005. 40Ar/39Ar Thermochronologic Record of 1.45–1.35 Ga Intracontinental Tectonism in the Southern Rocky Mountains: Interplay of Conductive and Advective Heating with Intracontinental Deformation. *In* Karlstrom, K.E., Keller, G.R. (Eds.), The Rocky Mountain Region - An Evolving Lithosphere Tectonics, Geochemistry, and Geophysics: Washington, D.C., American Geophysical Union Monograph 154, 163–184.

Silver, L.T., 1965. Mazatzal orogeny and tectonic episodicity. Geological Society of America Special Paper 82, 185–186.

Silver, L.T., 1968. U-Pb isotope relations and their historical implications in Precambrian zircons from Bagdad Arizona. Geological Society of America Special Paper 101, 420.

Silver, L.T., Bickford, M.E., Van Schmus, W.R., Anderson, J.L., Anderson, T.H., Medaris, L.G., Jr., 1977. The 1.4–1.5 b.y. transcontinental anorogenic plutonic perforation of North America: Geological Society of America Abstracts with Programs 9 (7), 1176–1177.

Smith, D.R., Noblett, J., Wobus, R.A., Unruh, D., Douglass, J., Beane, R., Davis, C., Goldman, S., Kay, G., Gustavson, B., Saltoun, B., Stewart, J., 1999. Petrology and geochemistry of late-stage intrusions of the A-type, mid-Proterozoic Pikes Peak batholith (Central Colorado, USA): implications for petrogenetic models. Precambrian Research 98, 271–305.

Vernon, R. H., Flood, R. H., D'Arcy, W. F., 1987. Sillimanite and andalusite produced by base-cation leaching and contact metamorphism of felsic igneous rocks. Journal of Metamorphic Geology 5, 439–450.

Vigneresse, J.L., 2005. The specific case of Mid-Proterozoic rapakivi granites and associated suite within the context of the Columbia supercontinent. Precambrian Research 137 (1-2), 1–34.

Williams, M.L., 1991. Heterogeneous deformation in a ductile fold-thrust belt: The Proterozoic structural history of the Tusas Mountains, New Mexico. Geological Society of America Bulletin 103, 171–188.

Williams, M.L., Karlstrom, K.E., Lanzirotti, A., Read, A.S., Bishop, J.L., Lombardi, C.E., Pedrick, J.N., Wingsted, M.B., 1999. New Mexico middle-crustal cross sections: 1.65-Ga macroscopic geometry, 1.4 Ga thermal structure, and continued problems in understanding crustal evolution. Rocky Mountain Geology 34, 53–66.

Wolf, D.E., Andronicos, C.L., Vervoort, J.D., Mansfield, M.R., Chardon, D., 2010. Application of Lu-Hf garnet dating to unravel the relationships between deformation, metamorphism and plutonism: An example from the Prince Rupert area, British Columbia. Tectonophysics 485, 62–77.

2. Deformation assisted phase transformation: an example from the sillimanite-in isograd, Eolus batholith, Needle Mountains, Colorado, USA

Abstract

The Paleoproterozoic Vallecito conglomerate of the Needle Mountains, Colorado, experienced deformation and metamorphism during emplacement of the ~1.4 Ga Eolus batholith, producing a contact aureole defined by sillimanite near the pluton, andalusite and sillimanite together ~2 km from the pluton, and andalusite alone at greater distance. In the andalusite-sillimanite zone, sillimanite rich layers, poor in andalusite, define shear bands. In contrast, regions between shear bands contain abundant andalusite and sillimanite. A deformed sample is enriched in immobile elements, with an estimated major element mass loss of 43% relative to a weakly deformed sample. Modal and compositional variation between deformed and undeformed regions indicates that mass transfer was central to shear band development. This process changed the composition of the deformed sample, facilitated the localization of deformation, catalyzed metamorphism and allowed the assemblage to more rapidly approach equilibrium than weakly deformed assemblages.

Introduction

Understanding the feedbacks between deformation and metamorphism is central to understanding high temperature deformation in the middle crust. Although these interactions have been studied in both the laboratory and in nature (e.g. Goergen et al., 2008; Williams, 1999), the relationships remain complex and our understanding is far from complete. This paper describes two samples of aluminous schist, exploring how localization of deformation and metamorphism worked in concert to drive metamorphism toward completion. The samples were collected in a zone of coexisting andalusite and sillimanite along the sillimanite-in isograd within the contact aureole of the Eolus batholith in the Needle Mountains, Colorado. They contain identical mineral assemblages but distinct deformation textures associated with the metamorphic reactions producing sillimanite. The sillimanite growth fostered strain localization, producing feedback between deformation and metamorphism. These processes were facilitated by removal of mass from high strain regions, allowing metamorphism in shear bands to more readily reach equilibrium.

Geologic Background

The Needle Mountains of southwestern Colorado include Paleoproterozoic metaigneous and metasedimentary units, and Paleoproterozoic and Mesoproterozoic plutonic bodies (Barker, 1969; Harris *et al.*, 1987; Tewksbury, 1985; Gibson, 1990) (**Figure 2-1**). The unit of interest in this study is the metasedimentary Vallecito conglomerate, composed of interbedded layers of fine-grained quartzite, pebble to cobble

conglomerates, and narrow layers of aluminous schists (Barker, 1969). Centimeter to decimeter scale sedimentary bedding structures are preserved. The Vallecito conglomerate is younger than 1.706 Ga based on detrital zircon data (Jones *et al.,* 2009) and is older than the ~1.435 Ga Eolus granite (Gonzales *et al.*, 1996). After deposition, the Vallecito conglomerate experienced polyphase deformation, regional greenschist facies metamorphism and subsequent contact metamorphism during emplacement of the Eolus batholith (Barker, 1969; Tewksbury, 1989; Harris, 1990).

The Eolus granite consists of two exposures separated by ~10 km of metavolcanic and metasedimentary rocks, including the sample locality. Both exposures of the Eolus granite are surrounded by contact aureoles (Barker, 1969). Previously, workers studied the metamorphic aureole surrounding the Eolus granite (Gonzales *et al.*, 1996; Noel, 2002; Dean, 2004; Wu, 2006), estimating the pressure during emplacement to be 3-4 kbars. These aureoles have metamorphic field gradients that begin in greenschist facies at distances of 10 kilometers from the pluton and reach upper amphibolite facies near the pluton (Wu, 2006; **Figure 2-1**).

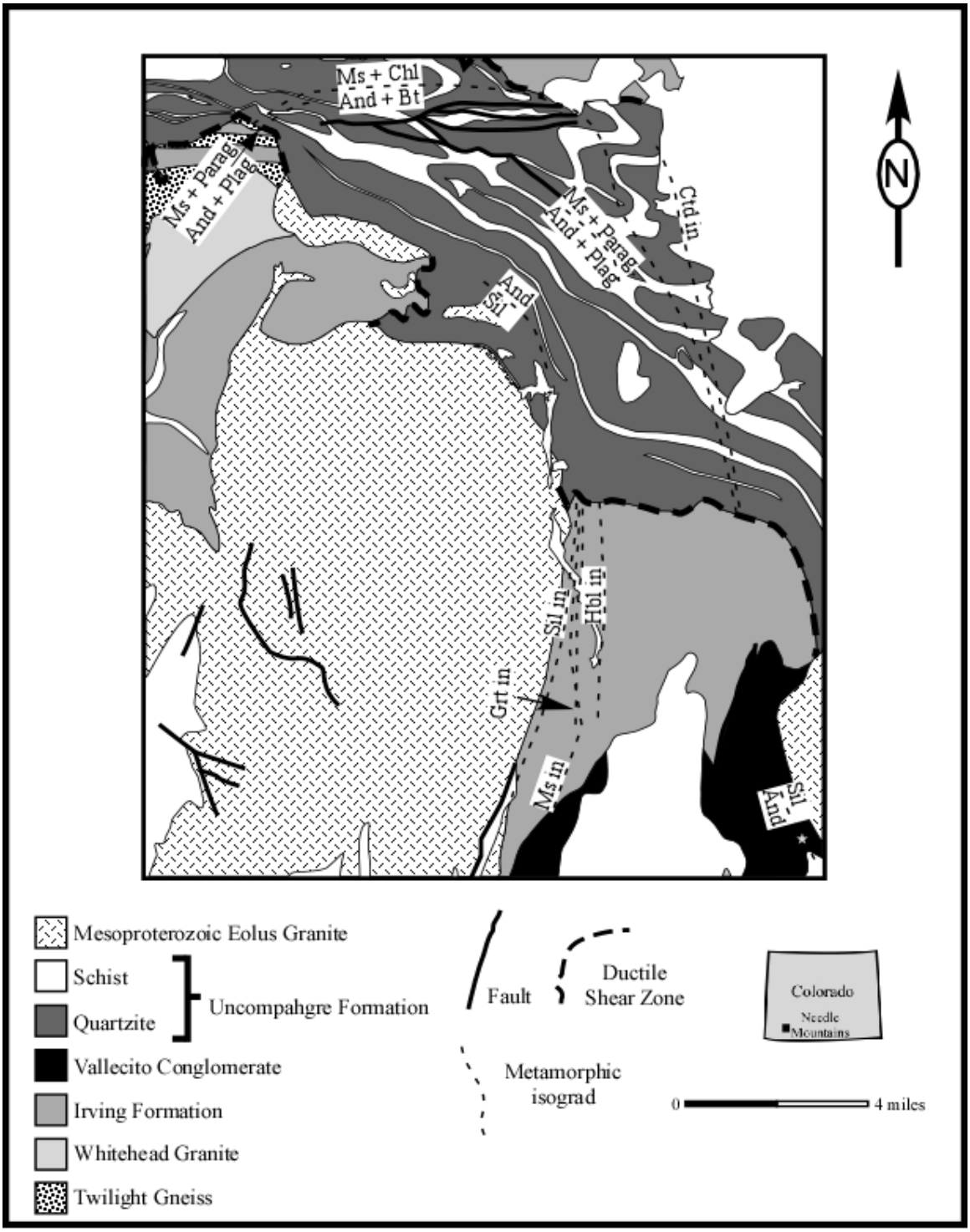

Figure 2-1: Simplified geologic map of the Needle Mountains, Colorado adapted from Barker (1969). The location of both samples is starred. The metamorphic isograds are compiled from Noel (2002), Dean (2004) and Wu (2006), and this study.

Field relationships

Oriented samples were collected from a layer of aluminous schist within the Vallecito conglomerate, in a zone of coexisting andalusite and sillimanite along the sillimanite-in isograd. Here, upright beds dip 81ºS and strike 116º, roughly parallel to the strike of the plutonic contact. Bedding was not folded at the outcrop scale; however, nearby outcrops contain steeply plunging to subvertical upright and steeply inclined folds. Additionally, the unit is folded into a map-scale, upright, gently plunging, north-south trending anticline, although microstructural evidence of this folding is locally overprinted by deformation associated with the pluton emplacement.

C-type shear bands (Berthé *et al.*, 1979), ~0.1 to 2cm in width and several meters in length are common within the studied outcrop. The shear bands form two populations based on their dips: moderately northeast, and steeply southwest. Both groups strike ~116º, parallel to the strike of bedding and the contact with the Eolus granite. This fact, and the observation that the shear bands are composed of metamorphic minerals associated with the contact aureole, suggest syn-emplacement formation of the shear bands.

The two samples (**Figure 2-2**), collected from one outcrop, are aluminous schists with mm scale andalusite prophyroblasts and fibrolitic sillimanite mats (**Figure 2-3**). The mineral assemblage of both samples includes muscovite, quartz, sillimanite, andalusite, chloritoid, chlorite, rutile, ilmenite, paragonite and magnetite. Andalusite and sillimanite are inferred to have formed during contact metamorphism because their isograds parallel

the contact with the granite. Minerals in the samples that may be vestiges of preceding regional metamorphism include chlorite, chloritoid and paragonite.

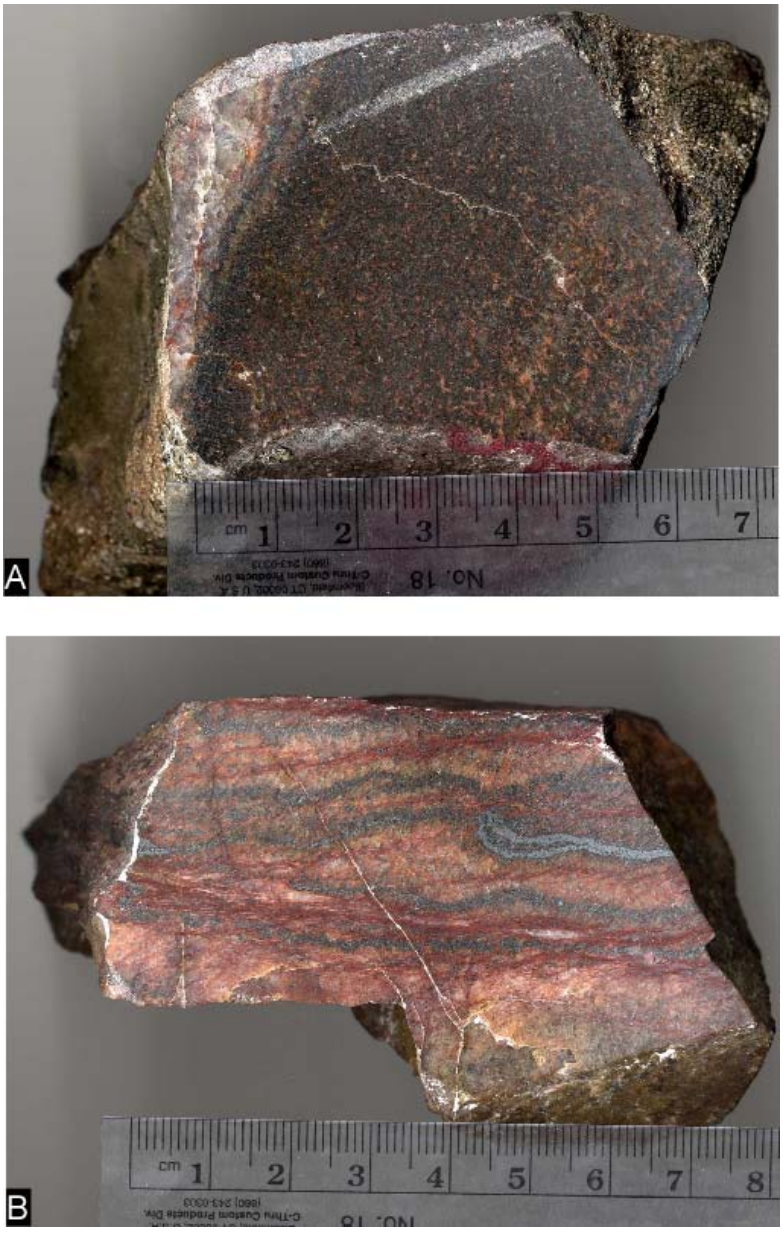

Figure 2-2: Scanned images of the polished surfaces of the weakly deformed (A) and deformed (B) samples. Thin sections for each sample were cut from the surfaces shown. In (A), bedding is defined by compositional variation oriented roughly N-S in this image and is gently folded. Bedding in (B) is also defined by compositional variation oriented roughly E-W in this image; however, bedding planes in (B) are sheared and crenulated. Sillimanite rich shear bands may be identified in hand sample by their deep red color and their orientation parallel to bedding. As viewed here, shearing in (B) is dextral.

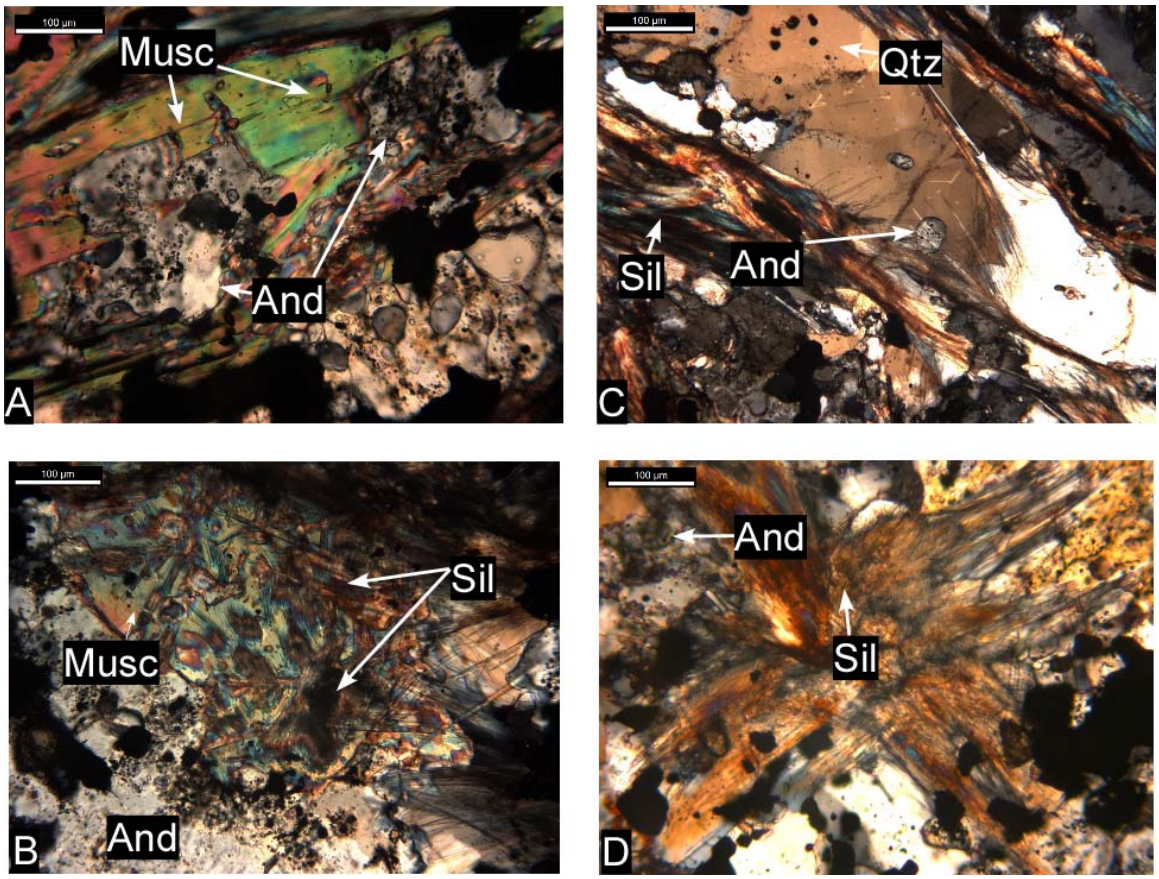

Figure 2-3: Photomicrographs of thin sections from deformed and weakly deformed samples. (A) Muscovite surrounding a poikilitic andalusite grain in the weakly deformed sample. Based on their shared extinction orientation, the andalusite grains are interpreted to be relics of one larger grain. (B) Mats of sillimanite forming triangular patterns within muscovite grains, interpreted to result from epitaxial replacement of octahedral layers in muscovite by sillimanite (Kerrick, 1990). (C) Lozenge-shaped quartz with undulose extinction and andalusite inclusions in a shear band of the deformed sample. Sillimanite needles help to define a foliation parallel to the lozenge-shaped quartz. (D) Coexisting andalusite and sillimanite in the weakly deformed sample, highlighting the lack of grain shape preferred orientation in the sample.

Although both samples contain identical mineral assemblages, one sample is deformed and contains two shear bands in thin section, whereas the other shows little evidence of deformation (**Figure 2-4**). Sillimanite needles in both shear bands curve into the high strain regions, implying progressive deformation during sillimanite growth. Based on their appearance in thin section of the deformed sample, the lower shear band involved lower strain.

Rose diagrams were created to compare the fabrics in the deformed and weakly deformed samples. In the less deformed sample, sillimanite defines a weak foliation parallel to bedding, seen best in the rose diagram (**Figure 2-3** and **Figure 2-4**). In the deformed sample, sillimanite defines two strong preferred orientations: in shear band cores, sillimanite is subparallel to bedding. In areas between the shear bands, sillimanite is at a high angle to bedding (**Figure 2-4**).

Comparing the rose diagrams of the deformed and weakly deformed samples shows that the fabrics are not relict bedding. In the weakly deformed sample, sillimanite has a weak preferred orientation that varies around bedding. In contrast, sillimanite in the deformed sample has a preferred orientation that varies systematically with respect to the shear bands, showing that variation in strain controls sillimanite orientation (**Figure 2-4**). However, bedding may have controlled shear band nucleation because they are sub-parallel to bedding.

The mode of minerals also varies across shear bands. Cores of the shear bands are characterized by aligned aggregates of fibrolitic sillimanite, elongate quartz, and oxides.

Andalusite occurs only as inclusions in quartz. Between shear bands, the foliation is defined by muscovite, fibrolitic sillimanite, abundant andalusite and oxides (**Figure 2-4**).

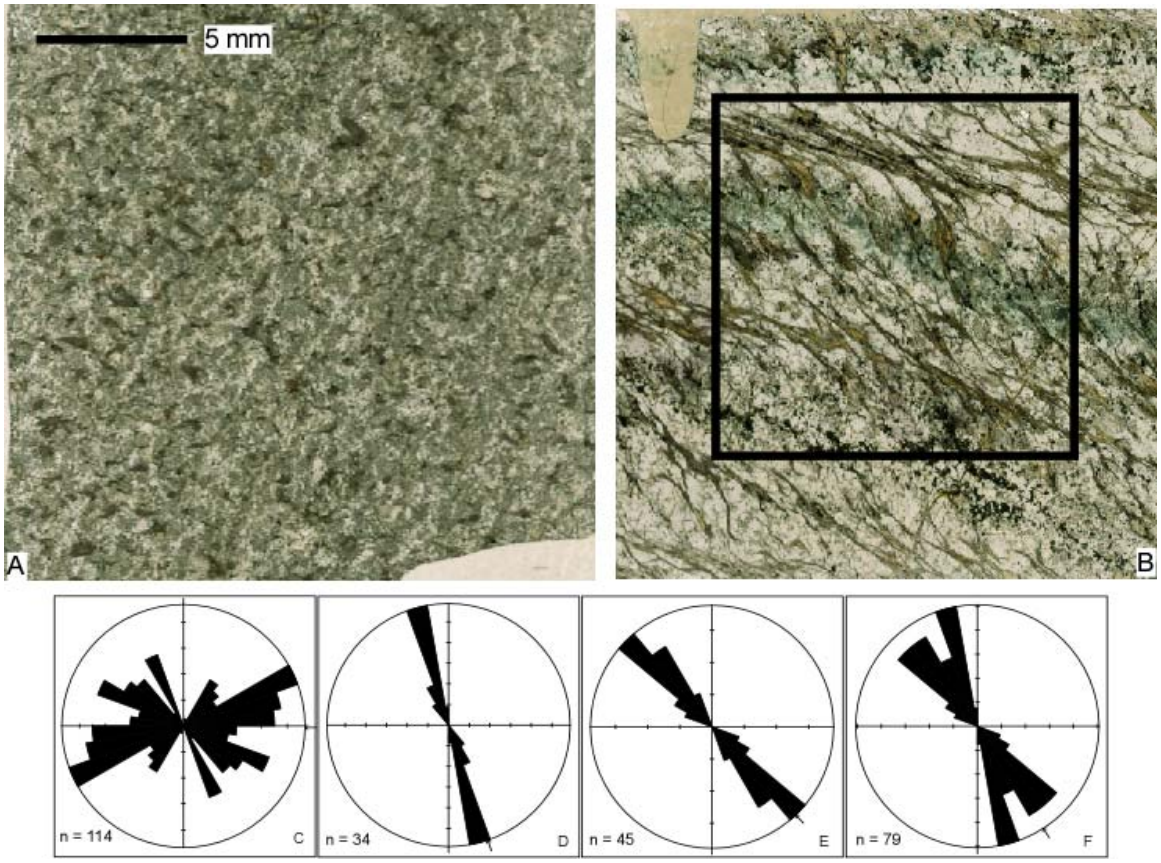

Figure 2-4: Scans of the thin sections from the weakly deformed and deformed samples. Also shown are rose diagrams illustrating sillimanite needle orientations measured relative to bedding for the weakly deformed sample and relative to shear bands for the deformed sample. Each rose petal represents 10 degrees. (A) A scan of the thin section of the weakly deformed sample. Sillimanite mats may be identified in this image as the tabular, opaque objects that are roughly 0.5 mm in length. Bedding is horizontal in this image. (B) A scan of the thin section of the deformed sample. Shear sense is sinistral in this view. Several key features are apparent, including the following: the oxide rich layer, defined by the band of opaque mineral grains; shear bands cored by sillimanite mats; and low strain domains, defined by coexisting andalusite, sillimanite and quartz. Two shear bands are visible in this thin section. The upper shear band records significantly more strain than the lower shear band. Sillimanite fibers form C-S type shear bands (Berthé et al., 1979; Passchier and Trouw, 2005), where the C surface shear zones are at a low angle of ~10º to the bedding surface and S surfaces are at 30º to C surfaces. Bedding runs left-to-right in this image. Oxide rich layers show an asymmetric crenulation cleavage which verges in the direction of shear. The black box indicates the region covered in X-ray element mapping of Figure 2-6. (C) A rose diagram for the weakly deformed sample showing orientation of sillimanite mats. (D) – (F) Rose diagrams showing sillimanite needle orientations for different regions of the deformed sample: (D) high strain regions (E) low strain regions, and (F) the entire sample.

Geochemistry

Comparing the whole rock composition of the samples allows compositional changes resulting from deformation and metamorphism to be evaluated. The samples were not collected from the same bed; however, they were collected two meters apart, and have identical mineral assemblages, suggesting compositionally similar protoliths.

Two approaches – concentration ratio diagrams and isocon diagrams – were used to assess compositional variation between samples. The concentration ratio diagram (**Figure 2-5**) shows the magnitude of compositional variation between samples. It is evident that immobile elements were passively concentrated in the deformed sample whereas major elements were depleted in the deformed sample relative to the weakly deformed sample.

The isocon diagram estimates the mass gained or lost during metamorphism relative to unaltered rock (**Figure 2-5**). For this method to be valid, the two samples must initially have the same composition. As discussed above, we suggest that the two samples roughly meet this criterion, although it is clear from their thin sections (**Figure 2-3**) that there is some variation between them. Ti, La and Ce were chosen as immobile elements for this exercise because these elements, generally considered immobile, have the same ratio between the deformed and weakly deformed samples, (**Figure 2-5**), suggesting that the concentrations of these elements has only varied passively and does not reflect compositional variation between the protoliths. Zr was not chosen because it may have been subject to bias by differences in the amount of zircon between the samples. Similarly, Al was not chosen because it falls along a line below the 1:1 line with most other major elements, suggesting that it, too, was mobile during fluid-present

metamorphism (e.g. Glen, 1979; Vernon, 1979). Using Ti, La and Ce as immobile elements, the deformed sample is depleted in most major elements by ~43%. The fact that most major elements fall along one line suggests systematic removal of elements and is evidence that the compositional differences between the samples does not reflect initial bulk composition variation.

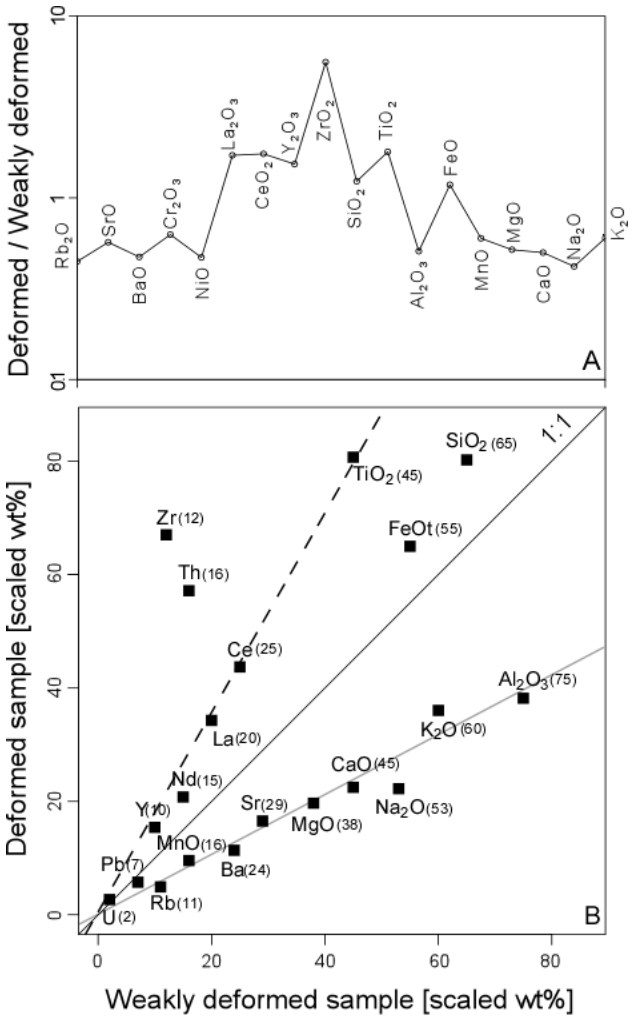

Figure 2-5: (A) A concentration ratio diagram of major elements and REEs (After Ague, 2003). The y-axis is the ratio of concentrations in weight percent of the deformed sample to the weakly deformed sample. Ti, La and Ce are inferred to have been immobile during metamorphism because these three refractory elements have the same concentration ratio in the deformed and weakly deformed samples. The dashed line represents the line of zero mass change based on the constant ratio between these immobile elements. (B) An isocon diagram, following the procedure of Grant (1986), provides a graphical estimate of gains and losses during metasomatic alteration (After Gresens, 1967). Scaling factors for each element are given in parentheses. Assuming the deformed and weakly deformed samples had the same protoliths chemically, Ti, La and Ce may be used as immobile elements to estimate the elements gained and lost in the deformed sample. The immobile isocon is marked by the dashed black line and has a slope of 1.8. Elements that fall above the isocon were concentrated in the deformed sample, while elements falling below the line were depleted. Most major elements fall along the gray line, with a slope of 0.5.

Mineral Chemistry

X-ray maps highlight a change in composition, observed in the K map, between low and high strain regions in the deformed sample (**Figure 2-6**). Shear bands are characterized by lower amounts of K than low strain areas, although the lower shear band, interpreted as lower strain than the upper shear band, still has a small amount of K. In the Na map (**Figure 2-6**), muscovite appears faint with patchy areas rich in Na along the rim. Due to their patchy appearance and presence mainly along rims, this paragonitic component is interpreted as developed during retrograde metamorphism. Representative compositions for muscovite and other minerals in the deformed and weakly deformed samples are presented in **Error! Reference source not found.** and **Table 2-2**.

The Al X-ray map and thin section showcase a change in mineral mode between high and low strain regions of the deformed sample, in contrast with the weakly deformed sample, where there is no modal variation across the thin section. In the X-ray maps, the highest Al concentrations are aluminosilicates: andalusite grains are rounded, whereas sillimanite is fibrous. High strain regions contain fibrolitic sillimanite with andalusite occurring only as inclusions in quartz, whereas low strain regions contain both aluminosilicates. At first glance, the modal abundance of aluminosilicates appears to increase in high strain regions of the X-ray map. However, although the cores of the shear bands have high concentrations of Al, the boundaries of the shear bands are enriched in quartz.

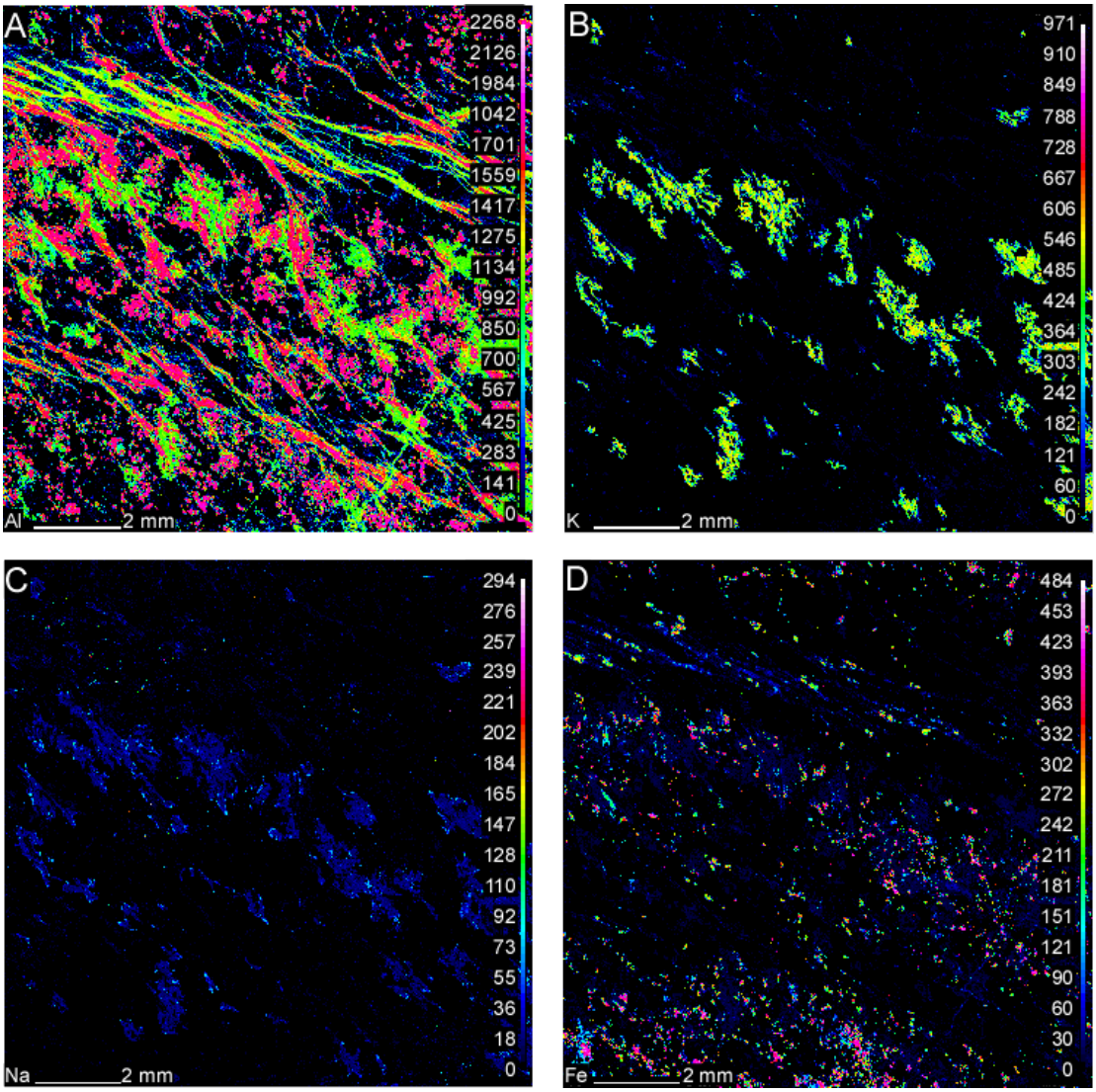

Figure 2-6: Wavelength dispersive scanning (WDS) X-ray element intensity maps for the region outlined by the black box in Figure 2-4. 1024 by 1024 pixel WDS X-ray maps were collected with a fixed beam using an accelerating voltage of 20 KeV, 200 nA beam current, an 8 micron beam diameter, a dwell time of 25 msec, and a 12 by 12 micron pixel size. Color corresponds to the concentration of the element measured, with warm colors indicating higher concentrations. Dashed white lines represent the boundaries of high strain regions. (A) An X-ray map of Al. Pinks and reds correspond to aluminosilicates – fibrous shapes are sillimanite while rounded shapes are andalusite. (B) An X-ray map of K. Here, warm colors correspond to muscovite. Note the absence of muscovite in high strain regions, with the exception of a few grains in the lower strain shear band. (C) An X-ray map of Na. Blue is muscovite, while yellow is paragonite. (D) An X-ray map of Fe. Bright colors correspond to oxide grains.

Metamorphic Reactions

Observing the difference in mineral textures and distributions between deformed and weakly deformed samples is critical to understanding the interactions of deformation and metamorphism. Andalusite and sillimanite occur throughout both samples; however, in the deformed sample, the andalusite to sillimanite transition has progressed to different degrees of completion in shear bands and non-shear band areas as described above. Furthermore, because of the close proximity of the samples, the variation in degree of conversion of andalusite to sillimanite cannot be the result of P/T differences.

Metamorphic textures demonstrate that the andalusite-sillimanite phase transition was accommodated through a series of reactions (**Figure 2-3**; e.g. Carmichael, 1969; Glen, 1979; Vernon, 1987a). In the weakly deformed sample, andalusite inclusions in muscovite grains share a common extinction angle. This shared crystallographic orientation is interpreted as evidence that muscovite replaced andalusite grains (**Figure 2-3**). Elsewhere in the sample, sillimanite forms triangular mats within grains of muscovite, representing epitaxial growth of sillimanite on muscovite, which indicates replacement of muscovite by sillimanite (**Figure 2-3**; Chinner, 1961; Kerrick, 1990). These observations are consistent with a cycle where muscovite replaces andalusite and sillimanite replaces muscovite (e.g. Carmichael, 1969; Kwak, 1971) with minor production of oxides from Fe^{3+} in andalusite. Similar reaction textures have been observed in both samples.

Isochemical phase diagrams were calculated to constrain the P/T conditions during deformation and metamorphism (**Figure 2-7**). Phase diagrams were calculated using Theriak-Domino (de Capitani and Petrakakis, 2010) assuming oxygen fugacity

buffered by hematite-magnetite and using XRF whole rock compositions for each sample (**Table 2-3**). The P/T conditions of metamorphism are constrained by the peak assemblage stability field (**Figure 2-7**), limiting pressures to 4.1-4.5 kbar and temperatures to 550º-570º C. The absence of feldspar, which should be present in small amounts according to the phase diagram, may be explained in several ways. The database used (Holland and Powell, 1998) may imperfectly describe mixing of possible elements in the minerals. For instance, Na, Ca and Fe occur in higher concentrations in muscovite than predicted by the phase diagram calculations. Alternatively, the patchy rims of paragonite on muscovite imply late growth that may signify the decomposition of albite during retrogression.

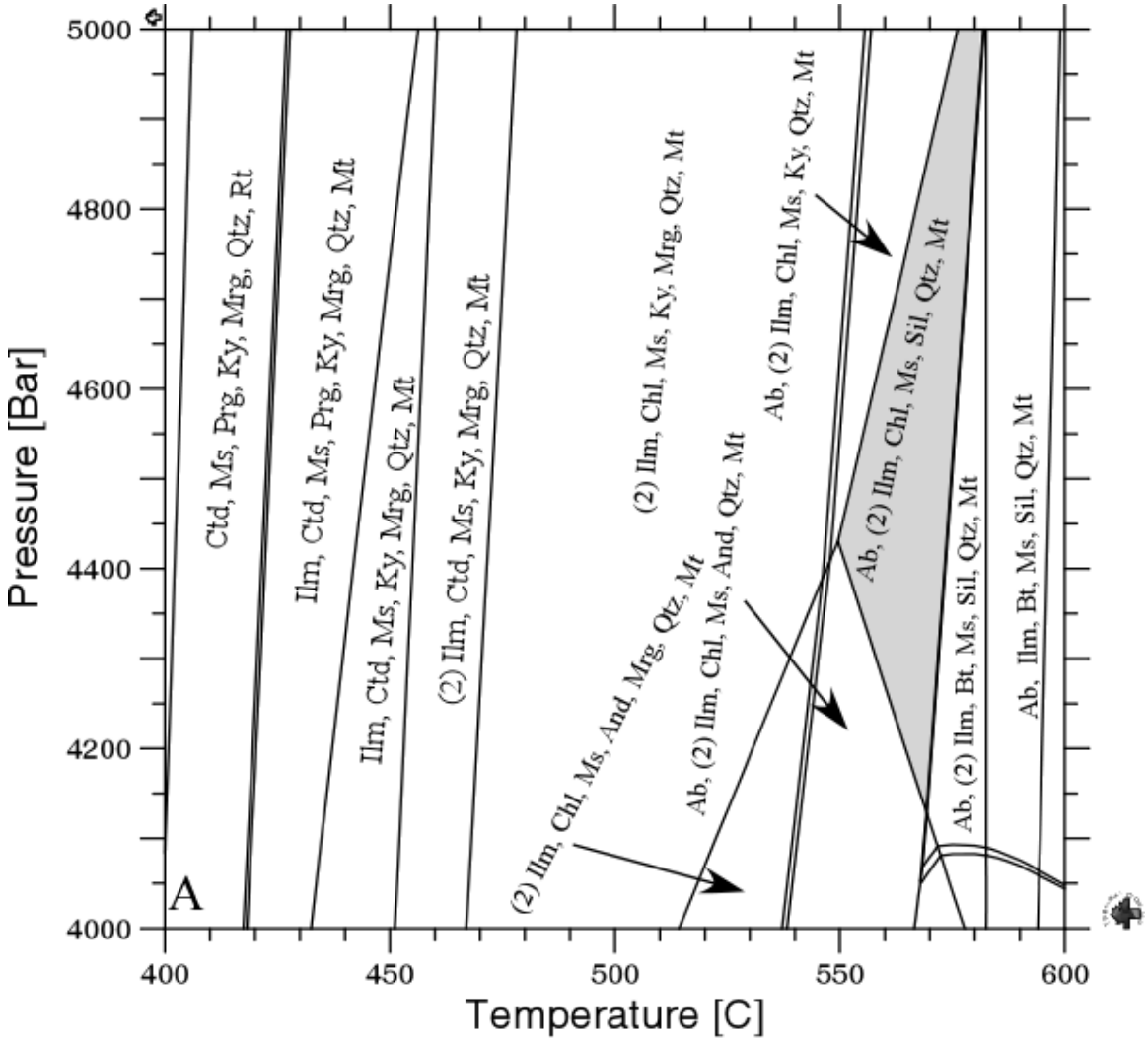

Figure 2-7: An isochemical phase diagram showing the equilibrium mineral assemblages over a range of pressures and temperatures for the deformed sample. The field highlighted in gray is the inferred peak mineral assemblage. The diagram was created using Theriak and Domino software suite (de Capitani and Petrakakis, 2010) using whole rock chemistry determined by X-ray fluorescence (Table 2-3). The internally consistent database of Holland and Powell (1998), including solution models of Mahar et al. (1997), Holland et al. (1998), Coggin and Holland (2002), Baldwin et al. (2005) and White et al. (2007) were used.

Discussion

Comparison of the deformed and weakly deformed samples yields several important observations. First, the transformation from andalusite to sillimanite involved a series of reactions where andalusite was replaced by muscovite and sillimanite replaced muscovite. Second, the mode of sillimanite is higher in shear bands and is uniform in the weakly deformed sample. Third, the change in composition, as reflected by X-ray maps, the concentration ratio diagram and the isocon diagram, suggests depletion of most major elements from the deformed sample. Fourth, most major elements fall along a line with a slope of 0.5 on the isocon diagram, implying mass loss during deformation.

Textural observations in thin section showed that the transformation from andalusite to sillimanite was not a simple phase change. Instead, the net reaction of andalusite to sillimanite was facilitated by growth of muscovite at the expense of andalusite and growth of sillimanite at the expense of muscovite. In the weakly deformed sample, these reactions occurred uniformly; however, in the deformed sample, X-ray mapping showed that muscovite replacement by sillimanite occurred preferentially in high strain regions, forming shear bands.

Noting that the mode of sillimanite increases and the mode of andalusite decreases in shear bands is of fundamental importance. This observation implies that sillimanite aggregates localize strain, while, at the same time, deformation enhances the metamorphic reaction facilitating sillimanite growth. Localization of strain to locations of sillimanite growth (e.g. Vernon, 1987b; Goergen *et al.*, 2008), implies that reaction softening played a role in the development of the shear bands.

The isocon diagram provides further insight into the processes governing deformation and metamorphism in the samples. The isocon diagram shows that the mass lost from the deformed sample is approximately 43%. This result is consistent with the removal of material via solution mass transport as hydrous minerals were removed from shear bands.

Finally, a mechanism is necessary to remove the major elements from high strain regions. Given that the contact aureole is a site of dehydration reactions and that the Eolus granite may have produced fluids, we suggest that the removal of these elements may have involved base leaching and solution mass transfer (e.g. Vernon, 1979; Vernon *et al.*, 1987).

Conclusions

The purpose of this study was to understand what caused the transition from andalusite to sillimanite to be nearer completion in shear bands than in weakly deformed regions of the studied outcrop. Results showed an example of reaction softening where deformation interacted with metamorphic reactions in a positive feedback loop to enhance strain localization while accelerating reactions, similar to the process suggested by Whitmeyer and Wintsch (2005). The localization of deformation and metamorphism was facilitated by solution mass transfer, removing major elements. Textural evidence shows that the transition from andalusite to sillimanite was a series of reactions. These reactions occurred at 4.1-4.5 kbar and 550º-570º C according to the stability field of the peak assemblage in the isochemical section (**Figure 2-7**). Although textural observation confirms that the same metamorphic reactions occurred in both samples, strain

localization correlates with an increase in the amount of sillimanite. These results suggest that mineral assemblages in high strain zones that developed during prograde metamorphism may more closely reflect peak metamorphic conditions because deformation serves to catalyze metamorphic reactions (e.g. Goergen *et al.*, 2008).

References:

Ague, J.J., 2003. Fluid infiltration and transport of major, minor, and trace elements during regional metamorphism of carbonate rocks, Wepawaug Schist, Connecticut, USA. American Journal of Science 303, 753–816.

Baldwin, J.A., Powell, R., Brown, M., Moraes, R., Fuck, R.A., 2005. Modeling of mineral equilibria in ultrahigh-temperature metamorphic rocks from the Anápolis–Itauçu Complex, central Brazil. Journal of Metamorphic Geology 23, 511–531.

Barker, F., 1969. Precambrian geology of the Needle Mountains, southwestern Colorado. United States Geological Survey Professional Paper 644-A, 1–33.

Berthé, D., Choukroune, P., Jegouzo, P., 1979. Orthogenesis, mylonite and non coaxial deformation of granites: the example of the South Armorican Shear Zone. Journal of Structural Geology 1, 31–42.

Carmichael, D.M., 1969. On the mechanism of prograde metamorphic reactions in quartz-bearing pelitic rocks. Contributions to Mineralogy and Petrology 20, 244–267.

Chinner, G.A., 1961. The origin of sillimanite in Glen Clova, Angus. Journal of Petrology 2, 312–323.

Coggon, R., Holland, T.J.B., 2002. Mixing properties of phengitic micas and revised garnet-phengite thermobarometers. Journal of Metamorphic Geology 20, 683–696.

de Capitani, C., Petrakakis, K., 2010. The computation of equilibrium assemblage diagrams with Theriak/Domino software. American Mineralogist 95, 1006–1016.

Dean, R.L., 2004. Aureole structure of 1.4 Ga plutons in southern Colorado and their tectonic implications: M.S. thesis, University of Texas at El Paso.

Gibson, R.G., 1990. Proterozoic contact relationships between gneissic basement and metasedimentary cover in the Needle Mountains, Colorado, U.S.A.. Journal of Structural Geology 12, 99–111.

Glen, R.A., 1979. Evidence for cyclic reactions between andalusite, “sericite” and sillimanite, Mount Franks area, Willyama Complex, N.S.W. Tectonophysics 58, 97–112.

Goergen, E.T., Whitney, D.L., Zimmerman, M.E., Hiraga, T., 2008. Deformation-induced polymorphic transformation: experimental deformation of kyanite, andalusite and sillimanite. Tectonophysics 454, 23–35.

Gonzales, D.A., Karlstrom, K.E., Siek, G.S., 1996. Syncontractional crustal anatexis and deformation during emplacement of ~1435 Ma plutons, western Needle Mountains, Colorado. Journal of Geology 104, 215–223.

Grant, J.A., 1986. The isocon diagram – a simple solution to Gresens' equation for metasomatic alteration. Economic Geology 81, 1976–1982.

Gresens, R.L., 1967. Composition – volume relationships of metasomatism. Chemical Geology 2, 47–65.

Harris, C.W., 1990. Polyphase suprastructure deformation in metasedimentary rocks of the Uncompahgre group – remnant of an early Proterozoic fold belt in southwest Colorado. Geological Society of America Bulletin 102, 664–678.

Harris, C.W., Gibson, R.G., Simpson, C., Eriksson, K.A., 1987. Proterozoic cuspate basement-cover structure, Needle Mountains, Colorado. Geology 15, 950–953.

Holland, T.J.B., Baker, J.M., Powell, R., 1998. Mixing properties and activity-composition relationships of chlorites in the system MgO-FeO-Al2O3-SiO2-H2O. European Journal of Mineralogy 10, 395–406.

Holland T.J.B., Powell R., 1998. An internally consistent thermodynamic data set for phases of petrological interest. Journal of Metamorphic Geology 16, 309–343.

Jones, J.V. III, Connelly, J.N., Karlstrom, K.E., Williams, M.L., Doe, M.F., 2009. Age, provenance, and tectonic setting of Paleoproterozoic quartzite successions in the southwestern United States. Geological Society of America Bulletin 121, 247–264.

Kerrick, D.M., 1990. The Al_2SiO_5 Polymorphs. Mineralogical Society of America Reviews in Mineralogy, 22.

Kwak, T.A.P., 1971. The selective replacement of the aluminum silicates by white mica. Contributions to Mineralogy and Petrology 32, 193–210.

Mahar, E.M., Baker, J.M., Powell, R. Holland, T.J.B., Howell, N., 1997. The effect of Mn on mineral stability in metapelites. Journal of Metamorphic Geology 15, 223–238.

Noel, M.E., 2002. Structure and metamorphism of the Eolus granite, Needle Mountains, Colorado: M.S. thesis, University of Texas, El Paso.

Passchier, C.W., Trouw, R.A.J., 2005. Microtectonics, 366. Springer, Berlin Heidleberg, New York.

Tewksbury, B.J., 1985. Revised interpretation of the age of allochthonous rocks of the Uncompahgre Formation, Needle Mountains, Colorado. Geological Society of America Bulletin 96, 224–232.

Tewksbury, B., 1989. Proterozoic geology of the Needle Mountains; A summary. Geologic Society of America Special Paper 235, 65–73.

Vernon, R. H., 1979: Formation of late sillimanite by hydrogen metasomatism (base-leaching) in some high-grade gneisses. Lithosphere 12, 143–52.

Vernon, R. H., 1987a: Oriented growth of sillimanite in andalusite, Placitas-Juan Tabo area, New Mexico, U.S.A. Canadian Journal of Earth Sciences 24, 580–90.

Vernon, R. H., 1987b: Growth and concentration of fibrous sillimanite related to heterogeneous deformation in K-feldspar–sillimanite metapelites. Journal of Metamorphic Geology 5, 51–68.

Vernon, R. H., Flood, R. H., D'Arcy, W. F., 1987: Sillimanite and andalusite produced by base-cation leaching and contact metamorphism of felsic igneous rocks. Journal of Metamorphic Geology 5, 439–50.

White, R.W., Powell, R., Holland, T.J.B., 2007. Progress relating to calculation of partial melting equilibria for metapelites. Journal of Metamorphic Geology 25, 511–527.

Whitmeyer, S.J., Wintsch, R.P., 2005. Reaction localization and softening of texturally hardened mylonites in a reactivated fault zone, central Argentina. Journal of Metamorphic Geology 23, 411–424.

Williams, M., 1990. Sigmoidal inclusion trails, punctuated fabric development, and interactions between metamorphism and deformation. Journal of Metamorphic Geology 12, 1–21.

Wu, K., 2006. Proterozoic tectonic evolution of the Needle Mountains, Colorado: Integrated structural and petrologic analysis of crustal formation and evolution: Ph.D. thesis, University of Texas, El Paso, 133.

Tables:

	Muscovite	Andalusite	Chrloitoid	Paragonite
		Oxide Wt%		
SiO_2	45.31	36.61	25.34	46.12
TiO_2	0.71	0.14	0.07	0.1
Al_2O_3	34.54	60.71	39.61	39.09
FeO	3.09	2.04	26.28	0.8
MnO	0	0	0.7	0
MgO	0.21	0.01	0.27	0.01
CaO	0.02	0.01	0	0.06
Na_2O	1.44	0.01	0.01	6.29
K_2O	8.43	0.01	0.01	1.4
Total	93.75	99.54	92.29	93.87
		Ions per formula unit		
Si	6.14	1	2.12	6
Ti	0.07	0	0	0.01
Al	5.51	1.96	3.9	5.99
Fe	0.35	0.05	1.83	0.09
Mn	0	0	0.05	0
Mg	0.04	0	0.03	0
Ca	0	0	0	0.01
Na	0.38	0	0	1.58
K	1.46	0	0	0.23
O,OH in Formula	22	5	12	22

Table 2-1: Microprobe analyses and structural formulas of minerals in the deformed sample. The beam conditions used to collect data were 20 KeV, 20 nA and a 5 micron beam. The analyses were conducted at Cornell University. A minimum of ten analyses were averaged for each mineral to produce an average mineral composition for the sample. Chlorite and sillimanite were too fine grained to produce acceptable analyses. Sillimanite fibers were assumed to be pure Al_2SiO_5.

	Muscovite	Andalusite	Chloritoid	Paragonite
	Oxide Wt%			
SiO_2	46.06	36.11	28.56	46.61
TiO_2	0.91	0.06	0.22	0.21
Al_2O_3	35.24	61.13	32.56	39.55
FeO	4.8	1.29	30.82	2.2
MnO	0.03	0.01	0.52	0.02
MgO	0.28	0.03	0.89	0.05
CaO	0.03	0.04	0.01	0.04
Na_2O	1.61	0.02	0.13	6.48
K_2O	7.18	0.01	0.37	1.28
Total	96.14	98.7	94.08	96.44
	Ions per formula unit			
Si	6.09	0.99	2.02	5.94
Ti	0.09	0	0	0.01
Al	5.49	1.98	3.94	6.06
Fe	0.53	0.03	1.98	0.09
Mn	0	0	0.06	0
Mg	0.06	0	0.02	0
Ca	0	0	0	0.01
Na	0.41	0	0	1.56
K	1.21	0	0	0.24
O,OH in Formula	22	5	12	22

Table 2-2: Microprobe analyses and structural formulas of minerals in the weakly deformed sample. The beam conditions used to collect data were 20 KeV, 20 nA and a 5 micron beam. The analyses were conducted at Cornell University. A minimum of ten analyses were averaged for each mineral to produce an average mineral composition for the sample. Chlorite and sillimanite were too fine grained to produce acceptable analyses. Sillimanite fibers were assumed to be pure Al_2SiO_5.

	Weakly Deformed Sample	Deformed Sample
SiO_2	58.82	70.46
TiO_2	1.51	2.63
Al_2O_3	31.18	15.41
FeO_{tot}	5.18	5.94
MnO	0.01	0.01
MgO	0.07	0.04
CaO	0.07	0.04
Na_2O	0.35	0.14
K_2O	0.75	0.44
P_2O_5	0.12	0.14
Sum	98.05	95.23
LOI	1.45	2.46
Ni	20	10
Cr	142	89
Sc	29	26
V	53	55
Ba	329	156
Rb	29	13
Sr	424	242
Zr	547	3054
Y	92	142
Nb	37.6	50.1
Ga	44	20
Cu	6	2
Zn	5	3
Pb	34	28
La	119	204
Ce	250	437
Th	35	125
Nd	114	158
U	14	19

Table 2-3: XRF analysis, conducted at Washington State University, of both deformed and weakly deformed samples. Major elements are shown as non-normalized weight percents. Trace elements are presented as non-normalized ppm

3. Metamorphic P-T paths across the Al_2SiO_5 triple point terrane of northern New Mexico, USA: Metamorphic Constraints on Orogeny in Southern Laurentia

Abstract

Proterozoic rocks in northern New Mexico record amphibolite facies metamorphism and are world-renowned for locales containing all three aluminosilicates. The metamorphic history of these rocks is controversial, with multiple tectonic histories proposed to explain their petrogenesis. Here we present petrologic and microstructural observations that demonstrate that different parts of the study area evolved along distinct P-T paths that locally culminated in metamorphic conditions near the Al_2SiO_5 triple point.

Through this study, we show that Proterozoic metamorphism in this region is characterized by clockwise P-T paths and amphibolite grade metamorphism. The relative timing of metamorphism and deformation varies across the field area; however, a compilation of aluminosilicate isograds shows an uninterrupted variation in metamorphic isograds that overprints ductile deformation structures. Derived pressure-temperature-time paths match the thermal trajectories of numerical models for collisional orogens. Our results suggest that rocks were brought from upper-crustal to mid-crustal levels by contractional deformation,

with resulting peak metamorphic conditions being diachronous across the triple point terrane. These features are most consistent with a model where crustal thickening and heat advection from plutons drives metamorphism. Based on these lines of evidence, we suggest that the triple-point assemblages are the product of a single orogenic event occurring between 1460 and 1400 Ma.

Introduction

The world famous aluminosilicate triple-point assemblages found in northern New Mexico have been the subject of extensive study (e.g. Holdaway, 1978; Grambling, 1981; Grambling and Williams, 1985; Holdaway and Goodge, 1990; Karlstrom and Williams, 1996; Williams *et al.*, 1999; Larson and Sharp, 2003; Daniel and Pyle, 2006). Understanding the petrogenesis of these rocks is of interest for several reasons: the aluminosilicates provide key constraints on the pressure and temperature (P/T) path and tectonic history of the region, central to understanding the growth of southwestern North America; and phase-relation independent estimates of P/T at the time of the formation of these assemblages can be used as a natural-check for experimentally and theoretically based estimates of the aluminosilicate triple point if the aluminosilicates represent equilibrium mineral assemblages (e.g. Grambling, 1981; Pattison, 1992).

Multiple competing tectonic models have been proposed to explain metamorphism in northern New Mexico. One model, proposed by Karlstrom and Williams (1996), involves initial metamorphism during an orogenic event

between 1700 and 1600 Ma and reactivation during a circa1400 Ma metamorphism, plutonism and intracontinental tectonism (e.g. Karlstrom *et al.*, 1997, 2004; Pedrick *et al.*, 1998; Williams *et al.*, 1999; Read *et al.*, 1999; Shaw *et al.*, 2001; McCoy *et al.*, 2005). However, recent geocrhonologic work, including dating of metamorphic monazite (Daniel and Pyle, 2006), detrital zircon in supracrustal metamorphic rocks (Jones *et al.*, 2011), and Lu/Hf garnet growth ages (Aronoff *et al.*, 2012) have produced evidence contradicting accepted tectonic models of Paleoproterozoic accretion followed by overprinting metamorphism at ~1400 Ma. In-situ dating by ion microprobe of monazite inclusions in kyanite from the Picuris Mountains of northern New Mexico yielded no evidence for metamorphism prior to 1440 Ma (Daniel and Pyle, 2006). Similarly, detrital zircon studies from the same supracrustal metamorphic units found a population of 1460 Ma zircons (Jones *et al.*, 2011), implying that these supracrustal rocks were at the surface of the earth as late as 1460 Ma. These observations have lead to the suggestion that a previously unrecognized orogenic event in northern New Mexico, termed the Picuris Orogeny (Daniel and Jones, 2012), produced the metamorphism recorded in the Picuris Mountains. Aronoff *et al.* (*2012*) found similar ages for garnet growth in both the Tusas and Picuris Mountains, which they use to suggest that this ~1400 Ma orogenic event affected both mountain ranges.

In order to clarify the petrogenesis of these unique assemblages, we combine petrologic and microstructural observations, isochemical phase diagram modeling and a regional compilation of aluminosilicate isograds across the

reconstructed orogen. Through this approach, we develop pressure-temperature-time (P/T/t) trajectories of metamorphism across the orogenic belt. These results are compared to thermal models to develop a tectonic history for the region during orogenesis. This tectonic model is then compared with map patterns of aluminosilicate isograds to fully characterize metamorphism and explain the petrogenesis of triple-point assemblages.

Results of this study show that regional amphibolite facies metamorphism in northern New Mexico followed a clockwise P-T-t path, around the aluminosilicate triple point. Although the character of the path is consistent across the Tusas and Picuris Mountains, the peak pressures and temperatures reached vary across the field study area. The nature of the P-T-t path is consistent with progressive loading during thrusting (e.g. Daniel *et al.*, 2003; England and Thompson, 1984; Beaumont *et al.*, 2001). These results are not consistent with previously proposed long-lived polymetamophic history. Instead, we suggest a single metamorphic event produced the aluminosilicate triple-point assemblages, and is an expression of the recently proposed Picuris Orogeny (Daniel *et al.*, 2012) in both the Picuris and Tusas Mountains of northern New Mexico.

Geologic Background

The focus of this study is on the Tusas and Picuris Mountains of northern New Mexico. Paleo-reconstructions removing Laramide-aged right lateral strike slip deformation show that these two mountain ranges were laterally continuous prior to faulting (Karlstrom and Daniel, 1993; Cather *et al.*, 2006; Jones *et al.*,

2011) (**Figure 3-1**).

The key stratigraphic units in our study area are supracrustal metavolcanic and metasedimentary rocks divided into two groups: the Vadito and the Hondo. The Vadito group lays in unconformable or tectonic contact with calcalkaline and greenstone basement rocks and is inferred to be older than the Hondo based on mapping of transitional rocks between the groups by Bauer *et al.* (2005) in the eastern Picuris Mountains. For a detailed description of the stratigraphy of the Vadito and Hondo groups in the Picuris and Tusas Mountains, see Bauer *et al.* (2005), Jones *et al.*, (2011), Bauer and Williams, (1989), Mawer *et al.*, (1990) and Soegaard and Eriksson (1986). Samples were collected in both the Tusas and Picuris Mountains from pelitic schists within the Vadito Group, as well as in the Rinconada Schist, and Ortega Formation in the Hondo Group (see **Figure 3-1** for locations).

Three generations of fabrics (S_1, S_2, and S_3) have been documented (see Williams *et al.*, 1999; Daniel and Pyle, 2006; Barnhart *et al.*, 2012) across the Tusas and Picuris Mountains. The orientation of the dominant fabric across the orogenic belt varies, with no evidence for over printing fabrics in some places, and near complete transposition in others. For detailed structural analysis, see Williams (1991, 1994), Bishop (1997), Williams *et al.* (1999), Daniel and Pyle (2006), Barnhart *et al.* (2012).

Previous field mapping (e.g. Williams, 1991; Lombardi, 1997) has identified a south dipping, east-west striking fault separating the southern Tusas from the central Tusas, which these workers have mapped as being roughly

parallel with F_2 axial surfaces. In a tectonic model proposed by Williams *et al.* (1999), this fault is produced by north-vergent thrusting.

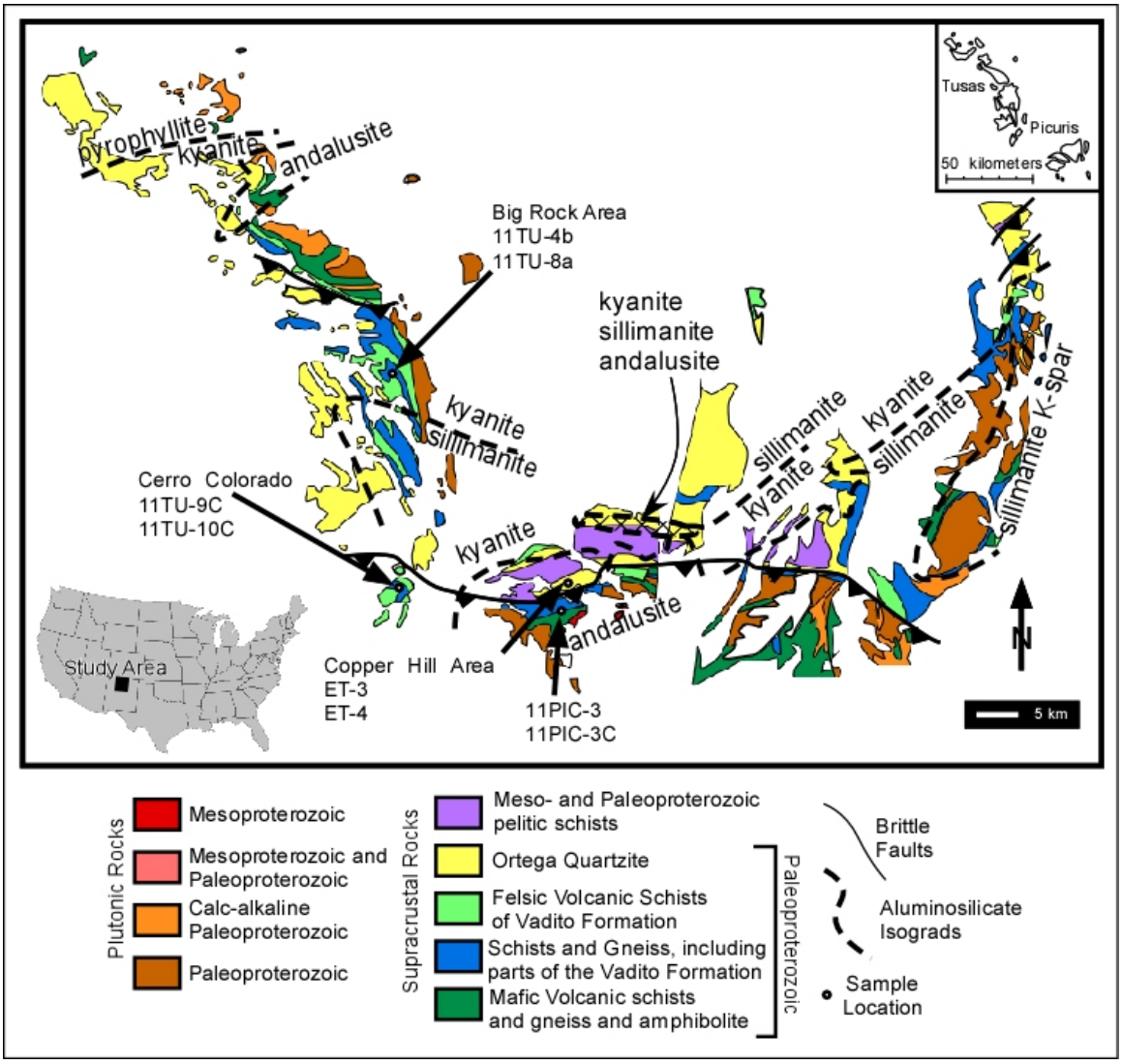

Figure 3-1: A simplified geologic map of the Proterozoic Orogenic belt with post-Proterozoic deformation removed (after Karlstrom and Daniel, 1993; Cather et al., 2006; Jones et al., 2011) is shown with sample locations. Aluminosilicate isograds are shown with heavy dashed lines (After Grambling, 1979, 1981; Read *et al.*, 1999, Holdaway, 1978; Price, 1997; Daniel and Pyle, 2006). Location of study area shown in inset in the lower left.

All of the supracrustal units in the Hondo, Vadito and Marqueñas experienced amphibolite grade metamorphism, although the timing and cause of this metamorphism remain the subject of study (e.g. Holdaway, 1978; Grambling, 1979, 1981; Karlstrom and Williams, 1996; Williams *et al.*, 1999; Shaw *et al.*, 2005; Daniel and Pyle, 2006; Barnhart *et al.*, 2012; Aronoff *et al.*, 2012). The timing of regional metamorphism was inferred by mapping of Ar/Ar cooling ages (Shaw *et al.*, 2005). Based on this mapping, regional high-grade metamorphism affected the central and southern Tusas Mountains, Picuris Mountains, Cimarron and Taos Range, Sangre de Cristo and the Wet Mountains (Shaw *et al.*, 2005) at 1400 Ma. Shaw *et al.* (2005) inferred that this metamorphic event was caused by heat advected by plutons in an intracontinetal tectonic setting.

Triple-point assemblages, described by Grambling and Williams (1985) and Grambling (1979, 1981), are present in the Picuris Mountains and Truchas Mountains. Peak P/T conditions for these assemblages were reported by Holdaway and Goodge (1990) ~530ºC and 4 kbar based on Grt-Bt geothermometry and aluminosilicate phase equilibria. Aluminosilicate isograds, compiled from Williams (1991), Read *et al.* (1999), Grambling (1981) and Grambling and Williams (1985), are shown in **Figure 3-1**. When overlaid on the reconstructed Proterozoic mountain belt (Karlstrom and Daniel, 1993; Cather *et al.*, 2006; Jones *et al.*, 2011), the isograds match up well across mountain ranges (see **Figure 3-1**).

Multiple models have been proposed to explain the metamorphism. The first model, by Karlstrom and Williams (1996), evokes a double loop to explain

the observed metamorphism. In this model, the authors suggests a pressure/temperature/time (P/T/t) path of metamorphism that follows a clockwise loop around the aluminosilicate triple point between ~1700 Ma and ~1600 Ma, followed by isobaric cooling at mid-crustal depths and an isobaric thermal excursion at 1400 Ma. The magnitude of the loop depends on the location. The P/T/t loop is based on observed metamorphic reaction textures, phase relationships and inclusion relationships (e.g. Williams *et al.*, 1991; Karlstrom and Williams, 1996; Williams *et al.*, 1999). The timing of this loop is based the timing of similar events in Arizona, correlated by similar fabrics and deformation textures and is contemporaneous with geochronologic constraints on the age of this deformation provided by other workers (e.g. Bauer and Williams, 1994). The second portion of this model, the thermal excursion at 1400 Ma, is based on the observation of ubiquitous ca. 1400 Ma igneous activity. This observation led Karlstrom and Williams to suggest that initial amphibolite facies metamorphism occurred at ca. 1700 Ma, and was later partially overprinted during plutonism at 1400 Ma. Two subsequent studies found evidence supporting this model. First, Shaw *et al.* (2005) compiled Ar/Ar cooling ages, showing that Proterozoic cooling ages show varying degrees of partial resetting, with biotite ages clustering tightly around 1400 Ma, muscovite ages showing a ~200 Ma spread and hornblende ages ranging from 1700 to 1400 Ma. Also supporting this model, Larson and Sharp (2003) found that oxygen isotopes of the aluminosilicates in triple point rocks at Turchas peak are not in isotopic equilibrium among all three aluminosilicates, implying that it is unlikely that the triple-point assemblage is an

equilibrium assemblage.

The tectonic model proposed by Daniel and Pyle (2006) is based on observations from the northern Picuris Mountains, and contrasts sharply with the model of Karlstrom and Williams (1996). Although both models involve a clockwise metamorphic trajectory that loops around the aluminosilicate triple point, Daniel and Pyle (2006) suggest that metamorphism involved a single loop at ca. 1400 Ma and did not involve a subsequent thermal excursion. This P/T/t trajectory was constructed based on reaction textures combined with ion microprobe U/Pb monazite ages. The timing of deformation relative to metamorphism was determined by careful microstructural observation and comparison of these observations with petrologic textures. Near concordant to concordant U/Pb ages from monazite range from 1434 +/-12 Ma to 1390 +/-20 Ma, consistent with Mesoproterozoic amphibolite facies metamorphism.

Methods

Mineral compositions and X-ray element intensity maps used for geothermobarometry were collected using a JEOL 8900 electron microprobe at Cornell University. X-ray maps were made using an accelerating voltage of 15 KeV, a beam diameter of 5 μm, and a beam current of 200 nA. A stationary beam was used with a dwell time of 20 ms and the stage was moved beneath the beam to make these maps. Mineral analyses were conducted using an accelerating voltage of 15 KeV, a probe current of 20 nA, and a beam diameter of 10 μm for micas and 2 μm for other minerals. Natural and synthetic mineral standards were used for calibration.

Geothermobarometry was conducted using two internally consistent software packages: Thermocalc (Holland and Powell, 1998) and winTWQ (Berman, 1988). Rim temperatures were obtained by pairing garnet rim compositions with minerals immediately in contact with the garnet, and core temperatures were obtained by pairing garnet core compositions with inclusions.

Whole rock chemistry of each sample, presented in Table 1 and used in the construction of isochemical phase diagrams, was determined by X-ray fluorescence (XRF) analysis of a powdered portion of each sample. These analyses were conducted at Washington State University.

Isochemical phase diagrams were created with the Theriak-Domino software suite (de Capitani and Petrekakhis, 2010). The whole rock chemistry presented in Table 1 was used as the input for construction of these sections. Internally consistent databases of Holland and Powell (1998) and Berman (1988) were used. In keeping with the findings of Holdaway (1978), a reduced water activity of 0.7 was used for isochemical phase diagrams created for staurolite bearing samples in the vicinity of aluminosilicate and chloritoid bearing samples

Results

Isograds and Field Gradients

We have compiled aluminosilicate isograds from previous studies (e.g. Grambling, 1981; Grambling and Williams, 1985; Williams, 1991; Read *et al.*, 1999) (see **Figure 3-1**). From this exercise, several interesting details become apparent. First, metamorphic isograds over much of the region have shallow dips,

cross-cutting deformation fabrics and major shear zones implying peak metamorphism outlasted deformation. Second, there is a field gradient preserved by the aluminosilicate isograds across the orogenic belt. The resulting map pattern is strongly controlled by topography, implying that the isograds formed with shallowly dipping isotherms (Grambling, 1981). In the northern Tusas Mountains, Al_2SiO_5 is absent, and pyrophyllite occurs, implying temperatures below ~420ºC (Williams, 1991). Kyanite is the first Al_2SiO_5 mineral to occur up-grade of pyrophyllite, and locally andalusite is present and texturally after kyanite. This is consistent with an increase in temperature to over ~450ºC at pressures below the Al_2SiO_5 triple point. Throughout most of the central Tusas Mountains kyanite is the stable polymorph. In the southern Tusas Mountains, sillimanite occurs and is texturally late with respect to kyanite (Barnhart *et al.*, 2012), indicating P/T conditions above the Al_2SiO_5 triple-point. Temperatures vary across the southern Tusas, but K-feldspar in the presence of sillimanite is not reported, implying temperatures below about 625ºC.

In the Picuris Mountains the distribution of Al_2SiO_5 Polymorphs is distinct form the Tusas. In the northernmost Picuris Mountains sillimanite is inferred to be the stable Al_2SiO_5 polymorph, and is texturally after kyanite. In a narrow band in the northern Picuris Mountains the rocks locally contain all three Al_2SiO_5 polymorphs (Holdaway and Goodge, 1991; Daniel and Pyle, 2006). Textures in these rocks indicate a sequence from kyanite to sillimanite, with andalusite being the texturally latest polymorph of Al_2SiO_5 (Daniel and Pyle, 2006). Daniel and Pyle (2006) inferred that these rocks experienced a clockwise P-T path at

temperatures slightly above the triple point with about 1 kbar of decompression. Immediately south of the region where all three polymorphs occur, kyanite is inferred to be the stable polymorph, although sillimanite is reported with kyanite in at least two localities. Further to the south andalusite occurs with inclusions of kyanite, and in the most southern parts of the Picuris Mountains andalusite occurs alone, with the exception of sillimanite adjacent to the 1.4 Ga Penasco granite. These features suggest that in the Picuris Mountains, the northern part of the range records the highest pressures at, or slightly above the Al_2SiO_5 triple point. Pressure decreases to the south to conditions within the andalusite stability field found in the southern parts of the range.

Further to the east the isograds are continuous with exposures in the Turchas Mountains in the restored configuration (**Figure 3-1**). In both the Truchas and Rio Mora areas, the distribution of the Al_2SiO_5 polymorphs is inferred to be a function of elevation (Grambling 1981; Williams and Grambling, 1990). Sillimanite occurs at the lowest elevations, and kyanite at the highest. Where present, andalusite occurs at intermediate elevations. Grambling (1981) showed that this distribution of minerals is consistent with nearly horizontal isotherms and isobars, with slightly higher pressures occurring towards the north within the Turchas Range.

Farther to the east, proceeding from Rio Mora to the Rincon Mountains, migmatitic gneiss is present, and the assemblage sillimanite + K-feldspar is widespread. Hercynite is locally reported, and the rocks are inferred to have undergone partial melting. Read *et al.* (1999) inferred P-T conditions of ~650ºC

and 4-6 kbar for this region, making this the highest grade portion of the Al_2SiO_5 triple point terrane.

Although the map pattern of aluminosilicate isograds is informative on its own, understanding the metamorphic history that produced these isograds is critical to developing a meaningful tectonic history. To determine the P/T/t trajectory of metamorphism in the Tusas and Picuris Mountains, samples, whose mineralogies are presented in Table 2, were collected from across metamorphic zones.

Petrology

Central Tusas Mountains

In the Vadito of the central Tusas Mountains, both garnet-bearing micaceous schists and kyanite rich quartzites are present (see Table 2). Within kyanite bearing quartzite, pseudomorphs of pyrophyllite were identified by Simmons *et al.* (2011), suggesting that kyanite grew at a relatively low metamorphic grade. Mineralogically, these rocks locally contain muscovite-kyanite-chloritoid consistent with temperatures below ~570ºC. Associated with the kyanite quartzite is a thin coarse grained staurolite bearing quartzite (Schreyer and Chinner, 1966) which contains quartz-staurolite-biotite-muscovite and chlorite, with the chlorite forming at the expense of biotite. It is likely that the staurolite-rich rocks formed a reaction such as kyanite + chloritoid = staurolite + quartz (Schreyer and Chinner, 1966). Oxygen isotope data constrains the peak temperature for this region to be between 530 and 580ºC (Simmons *et al.*, 2011).

A garnet bearing sample (11TU-4B) was collected from pelitic schist stratigraphically several meters below the Big Rock Conglomerate. This schist varies from less than one meter to tens of meters in thickness. Felsic metavolcanic rocks occur on both sides of the schists (Williams *et al.*, 1999; Simmons *et al.*, 2011). X-ray maps and compositional profiles (**Figure 3-2**, **Figure 3-3**) show typical growth zoning patterns for garnets in sample 11TU-4B, with the exception of Ca, whose content in garnets here shows an irregular, patchy zonation. Chernoff and Carlson (1997) suggest that such irregular Ca zoning is not a reflection of a rock-wide event, but rather a reflection of the local extent of a reaction in the vicinity of the growing garnet.

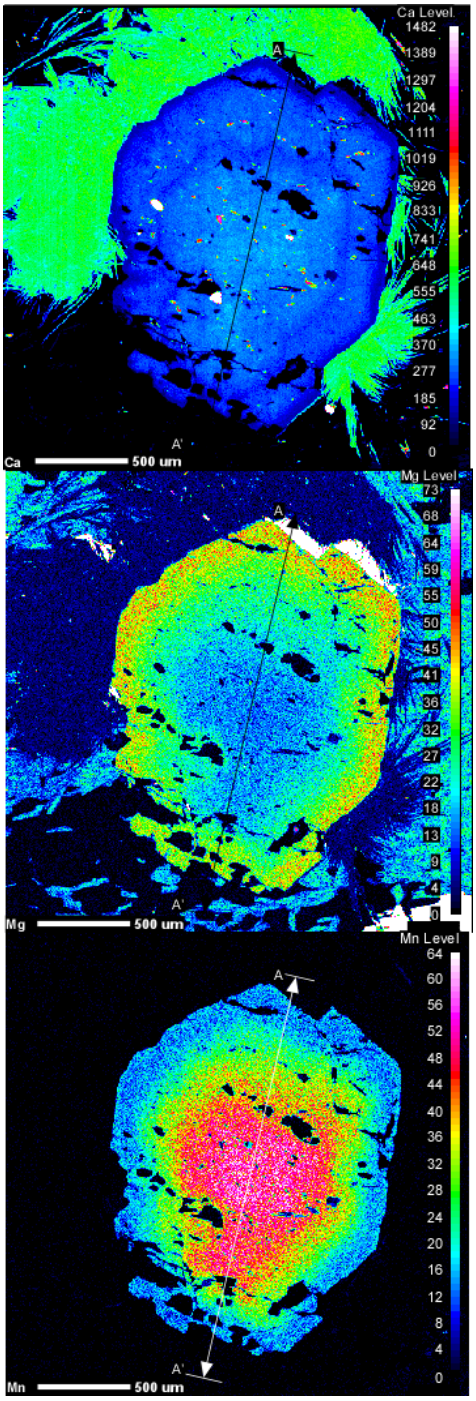

Figure 3-2: Electron microprobe X-ray element intensity maps for sample 11TU-4B in the Tusas Mountains. Color corresponds to the element concentration, with warm colors corresponding to higher concentrations. Transect line A-A' represents the quantitative line scan shown in Figure 3-3.

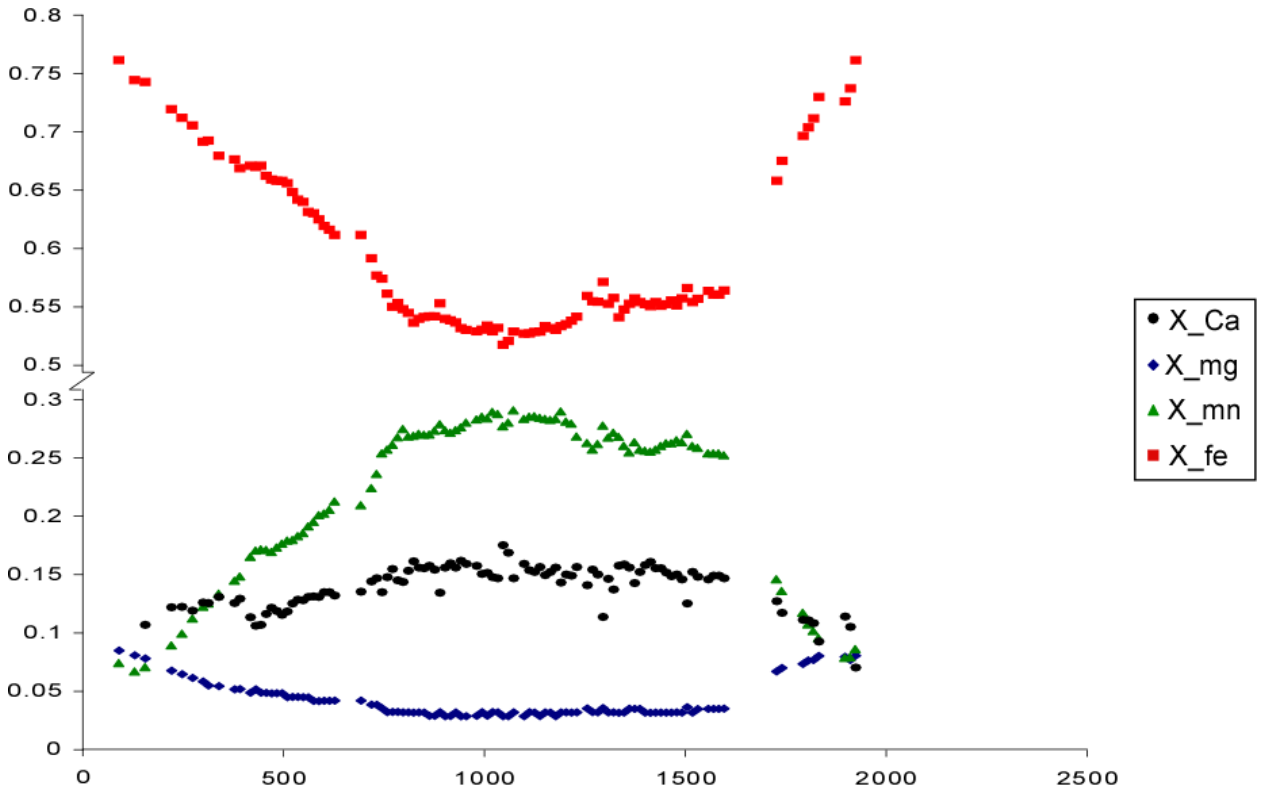

Figure 3-3: A compositional profile across a garnet from sample 11TU-4B. Note bell shaped zoning profile with high Mn concentrations in the core, decreasing the rim. X-ray maps for the same garnet are shown in Figure 3-2.

In this sample, segregated quartz and mica rich domains define the dominant S_2 foliation. An earlier fabric, almost entirely overprinted by the S_2 fabric, is preserved in microlithons (**Figure 3-4**a) and is interpreted to represent the earliest fabric (S_1). The S_2 fabric is crenulated by a third fabric (S_3), which is defined by spaced kink bands and microfolds (**Figure 3-4**a).

Several key textures and phase relationships constrain the P/T conditions in the Big Rock area. One such texture is the presence of zoisite in sample 11TU-4B both as inclusions in garnet and in the matrix. Another important texture in sample 11TU-4B is the presence of unfoliated splays of margarite surrounding garnets (**Figure 3-4**b). These textures indicate the peak mineral assemblage in the schists includes garnet + muscovite + biotite + quartz +/- ilmenite +/- hematite +/- staurolite. Locally, the presence of kyanite and staurolite in the absence of sillimanite limits the maximum temperature in the area, and implies a minimum pressure of 5.5 kbar and a maximum temperature bounded by the kyanite-sillimanite phase transition (**Figure 3-5**). Similarly, the presence of kyanite + chloritoid assemblages in the area provides a maximum constraint on the temperature of ~570ºC (**Figure 3-5**).

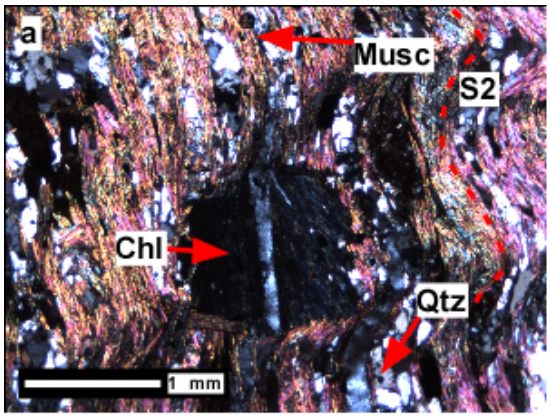
a
Musc
S2
Chl
Qtz
1 mm

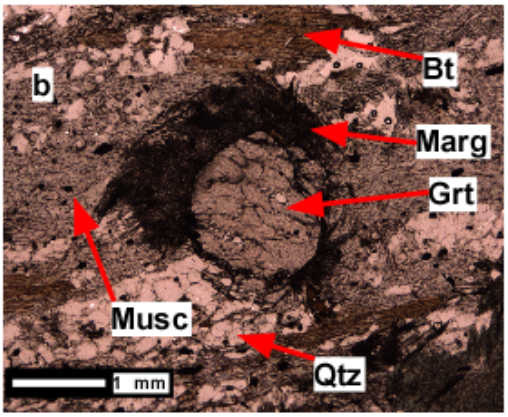
b
Bt
Marg
Grt
Musc
Qtz
1 mm

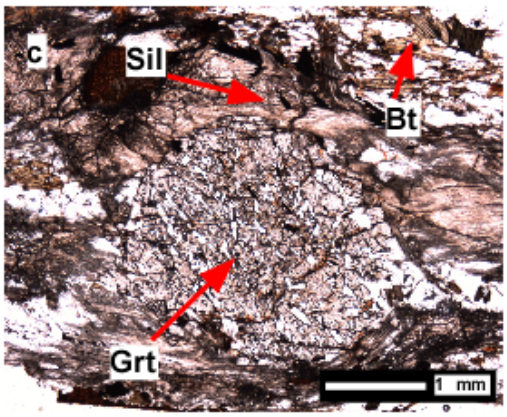
c
Sil
Bt
Grt
1 mm

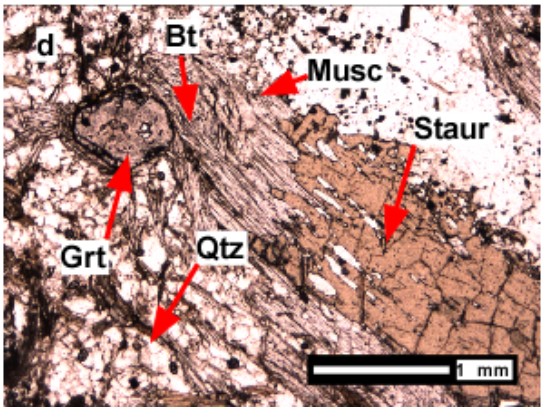
d
Bt
Musc
Staur
Grt
Qtz
1 mm

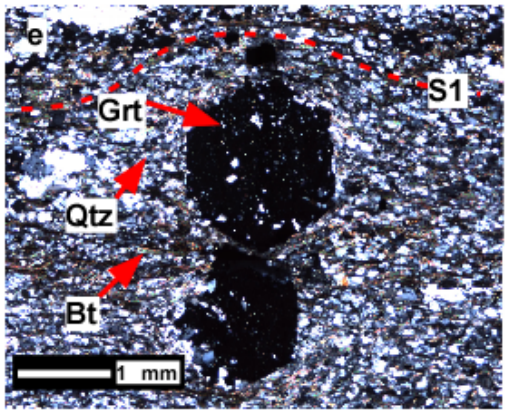
e
S1
Grt
Qtz
Bt
1 mm

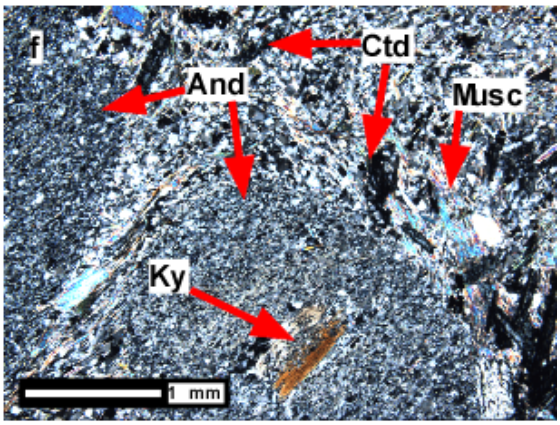
f
Ctd
And
Musc
Ky
1 mm

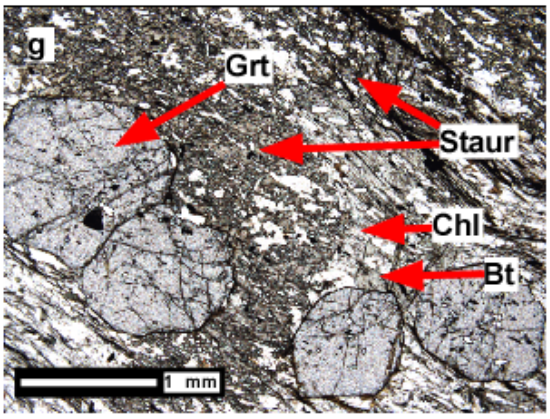
g
Grt
Staur
Chl
Bt
1 mm

Figure 3-4: Photomicrographs from the Picuris and Tusas Mountains showing key petrographic textures and microstructural relationships. A) A cross polarized light photomicrograph of a sample from the central Tusas Mountains showing a pseudomorph of chlorite after garnet. Matrix foliation runs from top to bottom in the image, and is defined by elongate Q and M domains. B) A plain polarized photomicrograph from the central Tusas Mountains. The dominant fabric, running from lower left to upper right is defined by quartz and mica rich layers. At the center of the image, garnet is surrounded by an undeformed halo of margarite. C) A plain polarized photomicrograph of garnet surrounded by a halo of sillimanite in a matrix of quartz, biotite and muscovite from the southern Tusas Mountains. The dominant foliation, S3, is defined here by the orientation of sillimanite needles in the halo. Preserved within the garnet are inclusions of quartz recording an earlier foliation at a high angle to S3. D) A plain polarized photomicrograph from the southern Tusas Mountains. Here, garnet, in the upper left, is separated from staurolite, in the lower left, by interfingering biotite and muscovite. Note that staurolite is replacing muscovite and the garnet is rimmed by biotite. E) A cross-polarized photomicrograph of garnet in a matrix of quartz and biotite from the Picuris Mountains. Matrix foliation, identified as S1, runs left to right in this photomicrograph. Inclusions within the garnet show no discernable orientation. Matrix fabric bends around the garnet. F) A cross-polarized photomicrograph of a sample collected from the Hondo syncline area, central Picuris Mountains. The image shows kyanite included by a large poikilitic andalusite grain in a matrix of quartz, chloritoid and muscovite. G) A plain polarized photomicrograph from the central Picuris Mountains. This image shows garnets included in staurolite grains in a matrix of quartz, biotite, muscovite and chlorite. In this same image, chlorite is part of the dominant fabric (S1), which is overprinted by late biotite.

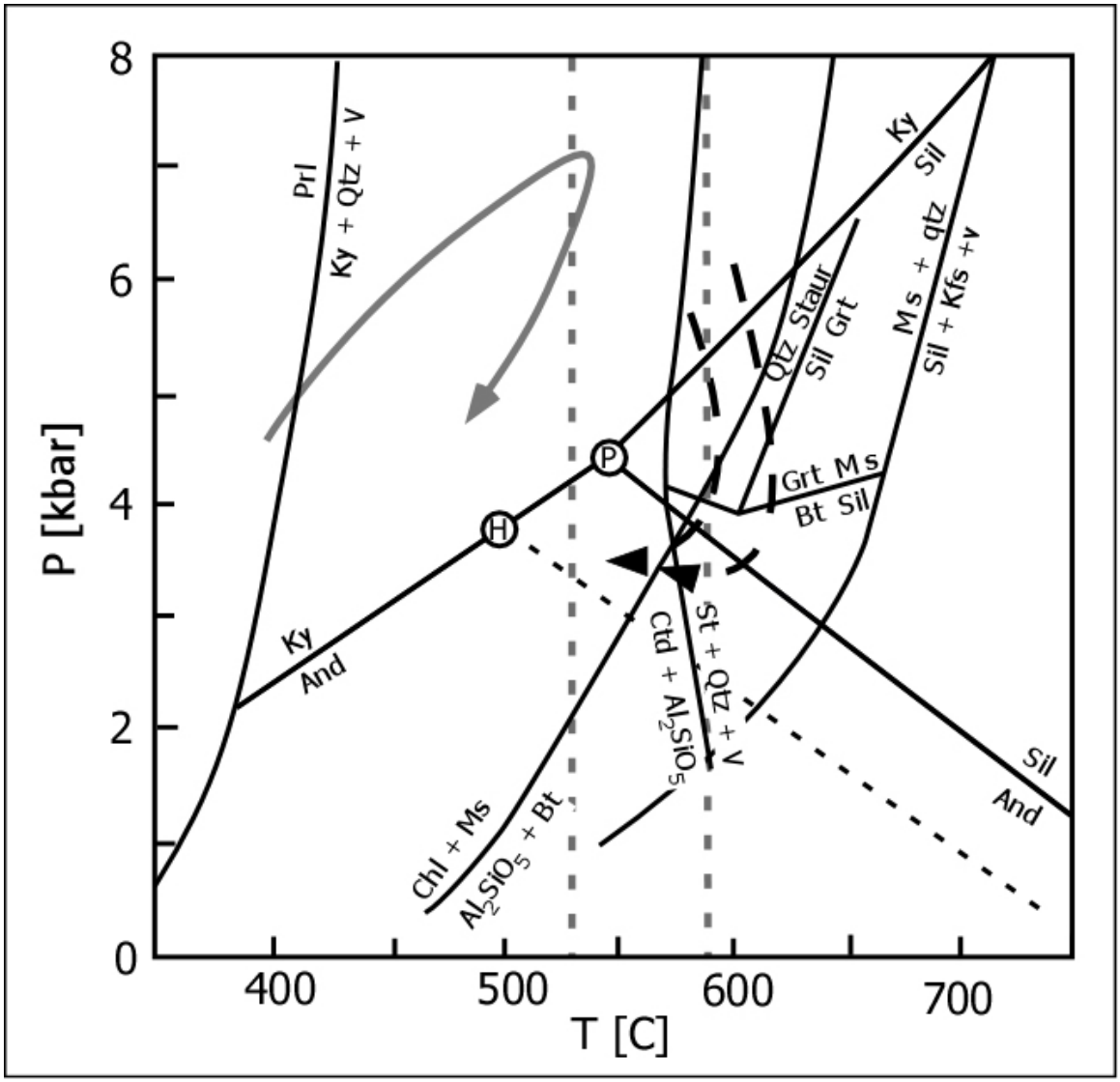

Figure 3-5: A petrogenetic grid of key reactions in the central Tusas Mountains in the Big Rock area. The Holdaway (1978) triple point is marked by an "H", while the Pattison (1992) triple point is marked with a "P". Dashed gray lines are temperature estimates from kyanite-quartz oxygen isotope thermometry for the kyanite quartzites (Simons et al., 2011). The dashed arrows represent the P/T paths determined for the southern Tusas Mountains at Cerro Colorado by Barnhart et al. (2012). The solid black arrow indicates the presence of staurolite after chloritoid in the Big Rock area (Rao & Johannes, 1979). The solid gray arrows represent the P/T paths in the Big Rock area as constrained by both isochemical phase diagram (see Figure 3-6) and reaction textures interpreted on this petrogenetic gird.

Comparison of the observed textures against a isochemical phase diagram for sample 11TU-4B is useful in explaining the textures described above as well as the P/T/t trajectory of metamorphism in the area. The presence of zoisite in 11TU-4B as inclusions in garnet as well as in the matrix of the sample provides a potential garnet growing reaction of chloritoid + zoisite + quartz = garnet + muscovite + H_2O in the presence of biotite and ilmenite as seen in the isochemical phase diagram (Figure 3-6). Comparing the isochemical phase diagram with the halos of margarite around garnet, we can infer that these halos represent the breakdown of biotite and garnet to form margarite and muscovite. The lack of foliation in this reaction texture implies that this is a late, post-D_3 decompression reaction. The textures described here indicate the peak mineral assemblage in the schists includes garnet + muscovite + biotite + quartz +/- ilmenite +/- hematite +/- staurolite. This peak assemblage is consistent with isochemical phase diagram P/T conditions of pressures above 6.2 kbar and temperatures between ~500 and 550ºC (Figure 3-6).

Unfortunately, from these exercises no good constraints on maximum pressure can be derived, although the presence of kyanite and staurolite in the region provides a lower bound of 4.2 kbar. The peak assemblage of 11TU-4B as described above, including garnet, quartz, muscovite, biotite and staurolite, is stable above 6.2 kbar (Figure 6). An identifiable retrograde assemblage in sample 11TU-4B includes garnet, quartz, ilmenite, chlorite, muscovite and margarite. After peak metamorphism, margarite was produced during post-D_3 retrograde metamorphism. The exact path of this retrograde metamorphism is obscured by textural ambiguity; however, regardless of the path between peak and post-peak

assemblages, these two assemblages require decompression of at least 1 kbar and a decrease in temperature of 50º C (Figure 3-6).

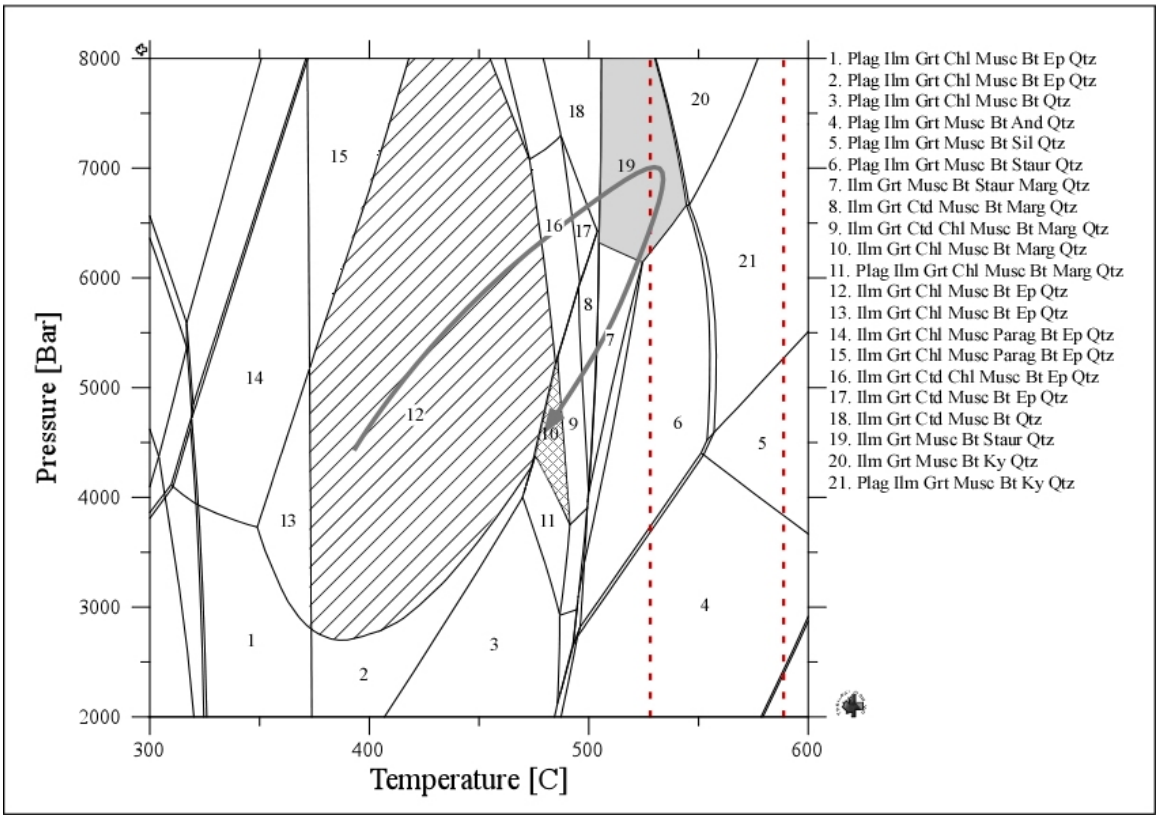

Figure 3-6: An isochemical phase diagram for sample 11TU-4B from the central Tusas Mountains. The P-T path is inferred to begin in the region 12 based on zoisite inclusions in garnet. The peak equilibrium assemblage is shaded in gray, region 19. Margarite rims on garnet and lack of feldspar in the samples indicate decompression from region 19 to region 7, with the path ending in region 10 where chlorite appears in the assemblage (hashed pattern). The path of metamorphism is shown with a solid gray line. Dashed red lines represent estimates of temperature in the vicinity of the collected sample as determined by Simmons *et al.* (2012) based on Oxygen isotope exchange between quartz and kyanite.

Southern Tusas Mountains

The dominant lithology at Cerro Colorado is the red-weathering metarhyolite of the Vadito group, which cores an east-west trending anticline. Samples collected from the Vadito group at Cerro Colorado contain a mineral assemblage of garnet – quartz – plagioclase – biotite – muscovite – staurolite – tourmaline +/- sillimanite, ilmenite and hematite (see Table 2).

Garnet bearing samples were collected from different stratigraphic levels of the metarhyolite in the Cerro Colorado area: garnet-staurolite schist (11TU-10C) was collected from high topography, and garnet-sillimanite schist (11TU-9C) was collected from roughly 200 m below. Fabrics in the area are variably defined, but are locally dominated by S2, a roughly southwest-northeast striking fabric that dips moderately to the south. Where notable, S3, a generally subvertical, east-west striking crenulation, is defined by oriented clots of sillimanite (**Figure 3-4**c).

In the Cerro Colorado area, there are several key textures and phase relationships that help to define the local P/T path. First, pseudomorphs of sillimanite after kyanite imply that the phase transition from kyanite to sillimanite occurred above the aluminosilicate triple-point. Barnhart *et al.* (2012) identified two key reaction textures that place important constraints on the P/T path of metamorphism in the southern Tusas Mountains at Cerro Colorado. Both reactions record decompression at temperatures between 550 and 610º C. The first reaction texture is halos of sillimanite around garnet representing the breakdown of garnet in the presence of muscovite to form sillimanite

and biotite (**Figure 3-4**c). The second reaction texture is garnet surrounded by a halo of inter-fingering biotite, muscovite and staurolite (**Figure 3-4**d) representing the breakdown of garnet in the presence of muscovite to form staurolite and biotite. These reactions both occur in samples in the southern Tusas Mountains, but at different crustal levels (see Barnhart *et al.*, 2012). Based on these observations, we infer that the peak assemblage in these samples includes garnet + quartz + biotite + muscovite + plag + tourmaline + staurolite + hematite. The presence of tourmaline in both 11TU-9C and 11TU-10C prevent construction of meaningful isochemical phase diagrams to corroborate P/T estimates.

As described by Barnhart *et al.* (2012), the P/T/t loop in the Cerro Colorado area loop begins in the kyanite stability field, crosses the staurolite-in reaction and enters the sillimanite stability field (**Figure 3-5**). This prograde metamorphism is then followed by decompression in the sillimanite stability field is recorded by two garnet breakdown reactions, producing staurolite and sillimanite (Barnhart *et al.*, 2012; see **Figure 3-5**).

Picuris Mountains

The mineralogy and metamorphism in the Picuris Mountains has been the subject of much study (e.g. Montgomery, 1953; Long, 1974; Holdaway, 1978; Bell, 1985; Grambling and Williams, 1985; Bauer, 1988, 1993; Holdaway and Goodge, 1990; Bauer and Kelson, 1997; Williams *et al.*, 1999; Daniel and Pyle, 2006). One reason for this is that it has been suggested that the northern Picuris Mountains contain triple-point mineral assemblages (Grambling and Williams, 1985; Holdaway and Goodge, 1990; Daniel and Pyle, 2006). The metamorphic P/T conditions in the area for these assemblages, based on

aluminosilicate phase relationships and garnet-biotite geothermometry, have been estimated to be roughly 525º C and 4.1 kbar (Grambling and Williams, 1985; Holdaway and Goodge, 1990; Daniel and Pyle, 2006).

In the central Picuris Mountains, garnet-bearing schists in both he Hondo and Vadito groups and aluminosilicate-bearing quartzites in the Hondo group are present. Mineralogically, these schists contain garnet + quartz + biotite + chlorite + muscovite + staurolite + ilmenite, whereas quartzites contain quartz + muscovite + aluminosilicate +/- chloritoid. Holdaway (1978) used experimentally derived equilibria to estimate the conditions of metamorphism at 3.7 kbar and ~530ºC. Furthermore, through his study, Holdaway (1978) showed that the juxtaposition of chloritoid bearing assemblages with staurolite bearing assemblages requires that the partial pressure of water in the staurolite samples be 0.88 or less in order to have chloritoid and staurolite bearing rocks interbedded.

In the central Picuris Mountains, samples were collected from both the Hondo and Vadito groups. The sample collected from the Hondo near Copper Hill, 11PIC-3, has a mineral assemblage of garnet – quartz – biotite – chlorite – muscovite – staurolite – ilmenite. X-ray mapping and compositional profiles (**Figure 3-7**, **Figure 3-8**) for 11PIC-3 show typical compositional growth patterns (e.g. Hollister, 1966), with the exception of Ca content, which shows irregular, patchy zoning with relatively small variation. Based on the findings of Chernoff and Carlson (1997), we suggest that this irregular zoning does not reflection a rock-wide event. This sample was collected in the vicinity of two plutons: the 1673 Ma Rana pluton and the ~1435 Ma Peñasco pluton. Locally, andalusite is

the stable aluminosilicate, although it is not present in the sampled schist of 11PIC-3. Sillimanite also occurs in the contact aureole of the Peñasco pluton. Another set of samples, ET-3 and ET-4 were collected from the Ortega Formation in the vicinity of the Hondo syncline. These samples are aluminum-rich quartzites with an assemblage of andalusite, kyanite, quartz, muscovite and chloritoid. Andalusite grains overgrow kyanite and appear in equilibrium with chloritoid, muscovite and quartz.

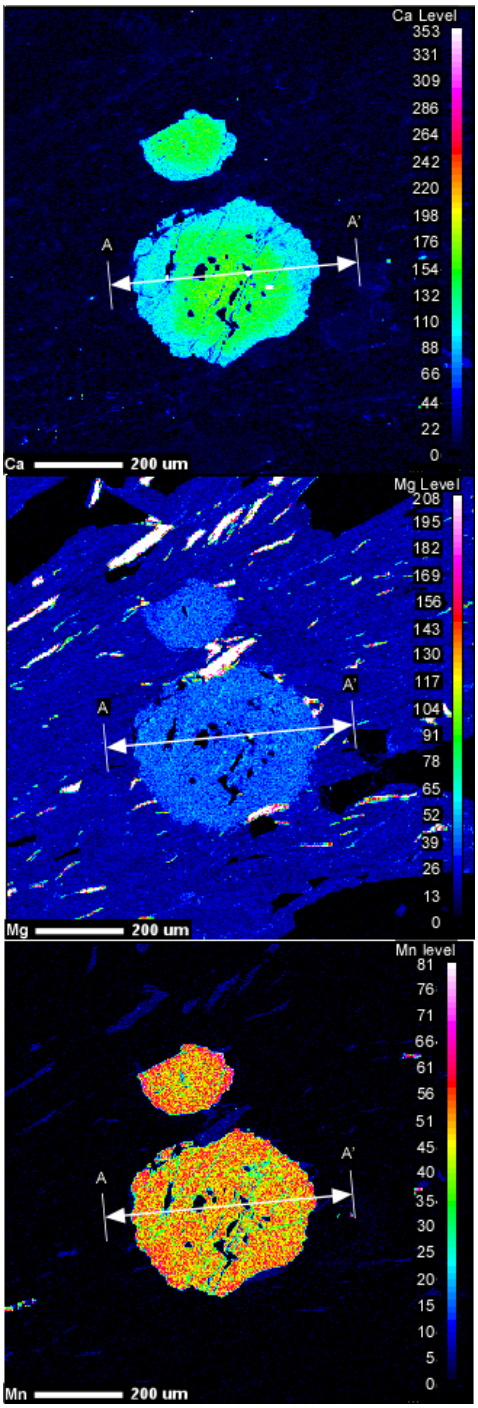

Figure 3-7: Electron microprobe X-ray element intensity maps for a garnet in the Picuris Mountains. Color corresponds to the amount of the measured element present, with warm colors corresponding to higher concentrations. Transect line A-A' represents the quantitative line scan shown in Figure 3-8.

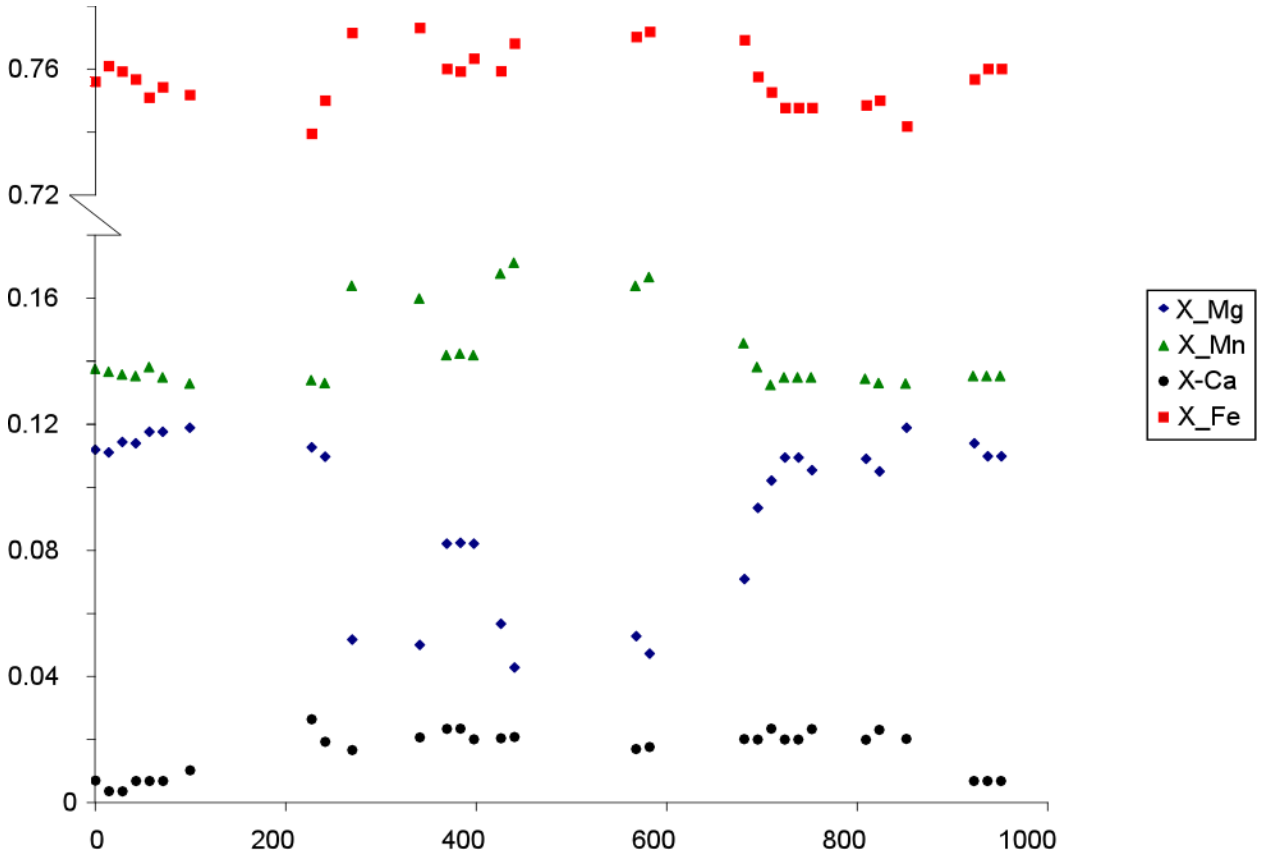

Figure 3-8: A compositional garnet profile across a garnet from sample 11PIC-3. X-ray maps for the same garnet are shown in Figure 3-7.

Limited evidence of deformation is recorded in the samples collected in the central Picuris. Although three generations of fabrics have been reported in the region (e.g. Daniel and Pyle, 2006), the dominant fabric observed in our samples from the central Picuris Mountains is defined by a matrix of aligned micas, representing S_1 (**Figure 3-4**e). Little evidence is present for S_2 or S_3 in these samples, other than the deflection of the fabric around garnets, implying a post-fabric and post-garnet growth episode of deformation.

In the central Picuris Mountains, several key reaction textures and phase relationships lend insight into the path of metamorphism. The first important texture is found in sample ET-3, collected from the Ortega formation near the Hondo snycline, where poikilitic andalusite grains preserve inclusions of kyanite (**Figure 3-4**f). This texture definitively shows that, locally, kyanite was the earliest aluminosilicate. Several textures are critical to identifying the peak assemblage of sample 11PIC-3. First, the presence of staurolite in sample 11PIC-3 implies that the sample crossed the staurolite-in reaction where staurolite and biotite are grown at the expense of chlorite and garnet in the presence of muscovite (**Figure 3-9**). Second, garnet cored by quartz and chlorite, provides evidence that one garnet forming reaction involved the breakdown of chlorite in the presence of quartz. Based on these textural observations, the inferred peak assemblage of sample 11PIC-3 includes garnet, quartz, biotite, muscovite, staurolite and ilmenite. A texture from another sample, 11PIC-3C, collected from the same outcrop, also bears an important texture, where garnets are present as

inclusions in staurolite (**Figure 3-4**g), implying that garnet growth occurred prior to staurolite growth and was likely involved in staurolite growth. In this same sample, chlorite is present as a fabric forming mineral, and is overgrown by biotite. This texture is indicative of a reaction such as chlorite and garnet producing staurolite and biotite.

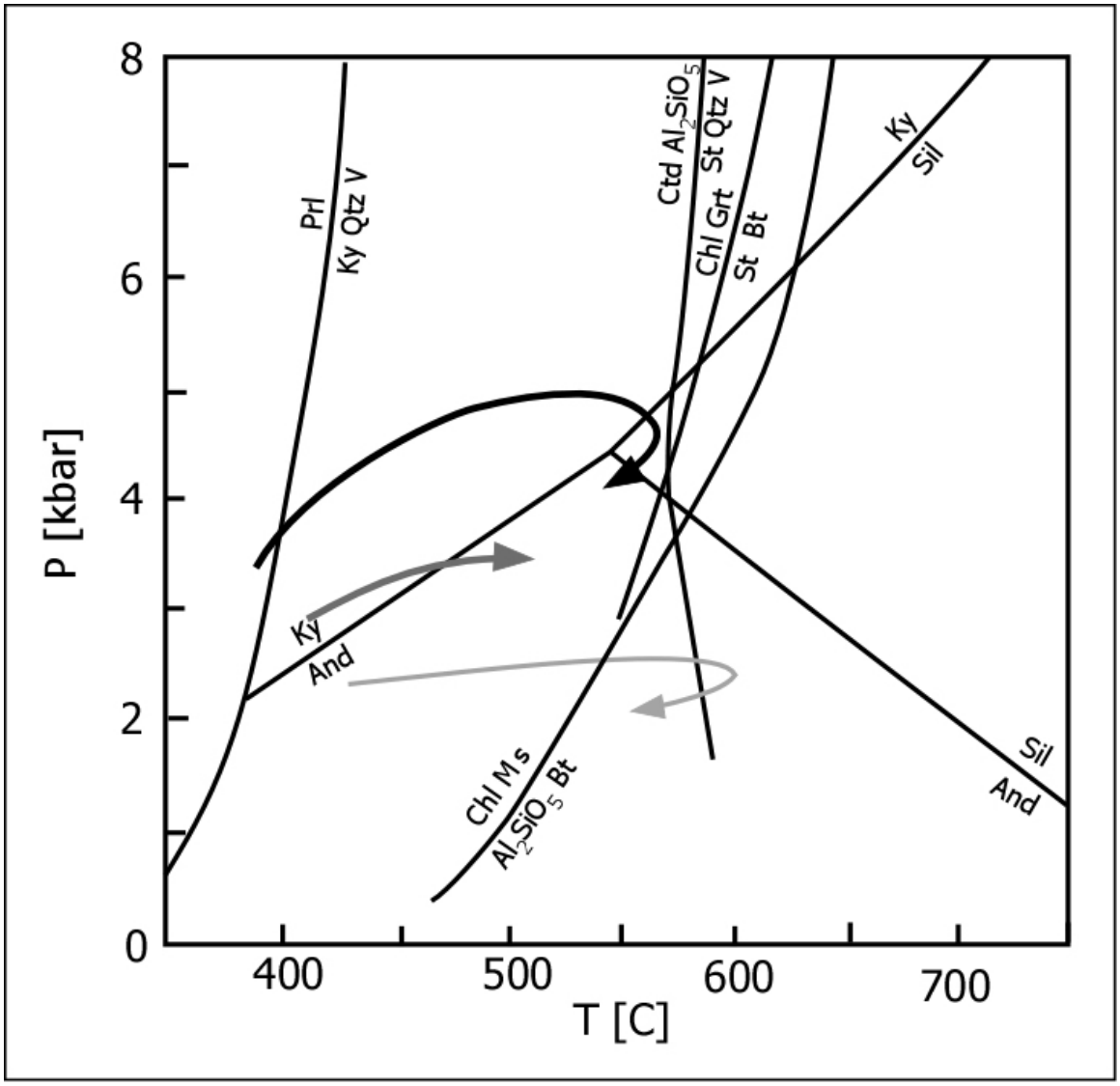

Figure 3-9: A summary of important reactions across the Picuris Mountains. Arrow 1 refers to a texture observed in the Ortega Quartzite near Hondo syncline, which preserves andalusite overgrowing kyanite in the presence of chloritoid. Arrow 2 refers to a texture observed in the central Picuris, where garnets are overgrown by staurolite and biotite. Shown with the heavily weighted gray arrow is the P/T path for the northern Picuris determined by Daniel and Pyle (2006) for rocks with all three aluminosilicates. Shown in dark gray is the P/T path determined by reaction textures in the central Picuris. Finally, in light gray is the P/T path reported by Williams et al. (1999) for the southern Picuris. Reactions curves are taken from Pattison (1992) and Pattison et al. (2002). The ctd reaction assumes an oxidation state at the hematite-magnetite buffer. The aluminosilicate triple point of Holdaway (1971) is shown with a dashed line.

In the northern Picuris Mountains, the presence of andalusite after sillimanite after kyanite provides the constraint that prograde metamorphism passed above the triple point (Daniel and Pyle, 2006). It is of note that the retrograde portion of paths in both the Tusas Mountains and Northern Picuris Mountains passes near the aluminosilicate triple-point and begin at vastly different crustal depths: as deep as 20 km in the central Tusas Mountains and as shallow as 12 km depth in the Picuris Mountains.

Comparison of the observed textures in sample 11PIC-3 with an isochemical phase diagram made for the sample is again useful in explaining the textures described above as well as the P/T/t trajectory of metamorphism in the central Picuris Mountains. The peak assemblage as determined above is stable over a range of pressures from ~3 to 7 kbar, and a range of temperatures from ~490 to 560ºC (**Figure 3-10**). However, because andalusite is the stable aluminosilicate, this P/T range is tightly constrained to a range of pressures between ~3 to 3.5 kbar and a temperature range between ~490 and 520ºC (**Figure 3-10**).

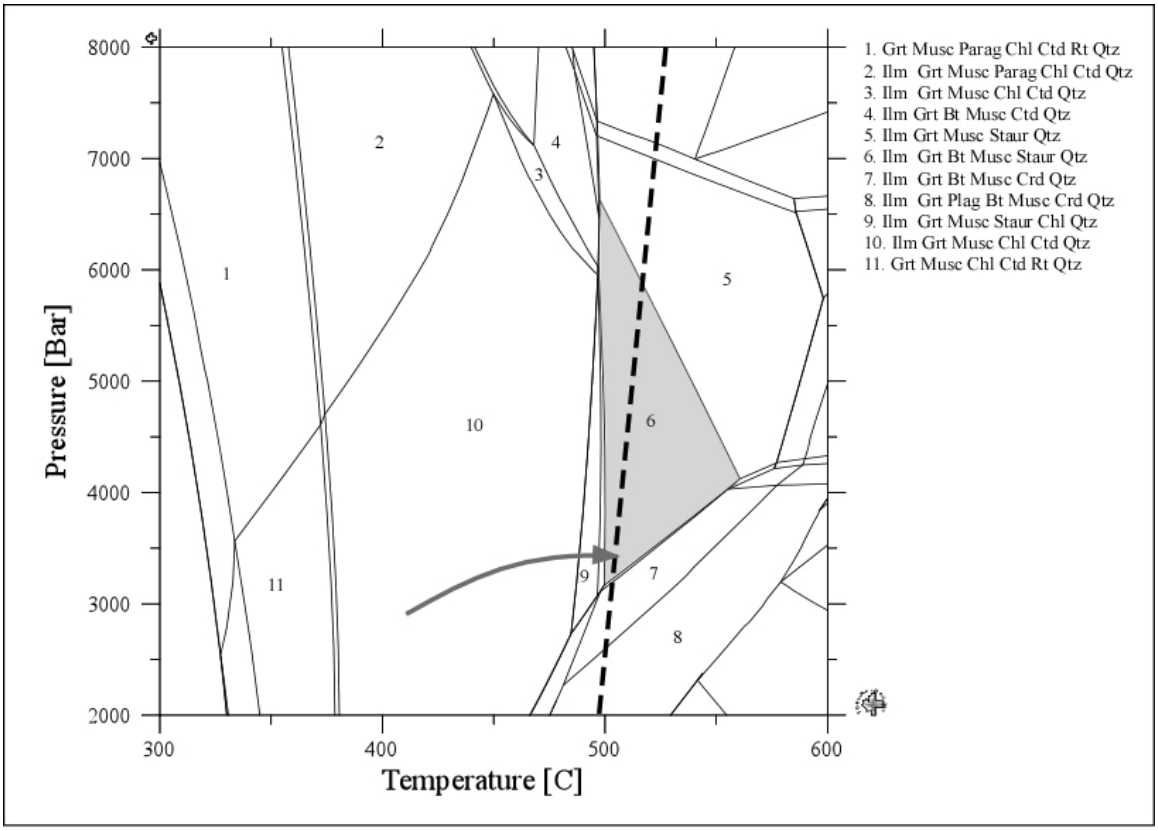

Figure 3-10: Isochemical phase diagram for sample 11PIC-3 made using the internally consistent database of Berman (1988) and a water activity of 0.7 (after Holdaway, 1978). The peak equilibrium assemblage is shaded in gray. Peak temperature for the garnet rim was calculated using winTWQ (Berman, 1988), shown with a dashed black line. Mineral compositions used for this analysis are shown in Table 4. Aluminosilicate stability fields are shown with the heavily weighted solid line. The P/T/t loop of Daniel and Pyle (2006) is shown with the dark gray arrow. The equilibrium assemblage of numbered stability fields is provided in Table 5.

Discussion

From the work of Aronoff *et al.* (2012), Daniel and Pyle (2006), and Jones *et al.* (2011), it is clear that high-grade metamorphism in the Tusas and Picuris Mountains occurred between 1460 and 1390 Ma. The absolute timing of the onset of amphibolite facies metamorphism is well constrained through multiple geocrhonologic dating techniques including the dating of metamorphic monazite (Daniel and Pyle, 2006), detrital zircons associated with pre-metamorphism sedimentary deposition (Jones *et al.*, 2011), and dating of garnet growth (Aronoff *et al.*, 2012). However, the tectonic environment which produced this metamorphism has remained enigmatic.

By combining the petrologic and isochemical phase diagram observations in both the Tusas and Picuris Mountains, we show that metamorphism in both the Tusas and Picuris Mountains followed clockwise P/T/t trajectories. In the Big Rock area of the central Tusas Mountains, metamorphism remained in the kyanite stability field, locally crossing into stability field of staurolite + kyanite reaching pressure of ~6.5 kbar and temperatures of at most ~570ºC (**Figure 3-5**). Further to the south in the Tusas Mountains at Cerro Colorado, Barnhart *et al.* (2012) show that metamorphism reached higher temperatures of ~610ºC at pressures of between ~4 to 6 kbar, crossing into the sillimanite stability field before decompressing with the breakdown of garnet (**Figure 3-5**). Moving to the south and east, we show that the P/T/t trajectory in the southern Picuris Mountains

reached peak metamorphism at P/T conditions of ~4 kbar and at most 550ºC.

The work in this paper supports the hypothesis put forward by Aronoff *et al.* (2012) and much of Williams *et al.* (1999). The clockwise P/T/t trajectories determined by the combination of petrogenetic grid and isochemical phase diagrams is consistent with the models of the thermal history of a fold and thrust belt during progressive loading and burial (e.g. England *et al.,* 1984; Beaumont *et al.,* 2001). This result is in keeping with north-vergent thrusting during orogenesis, as proposed by Williams *et al.* (1999) and Aronoff *et al.* (2012).

As other works have asserted, regional amphibolite facies metamorphism is associated with the orogenic event that formed the observed thrust faults, with garnet growth occurring variably between D_1 and D_3 fabric forming events (e.g. Williams *et al.*, 1999; Aronoff *et al.,* 2012). The duration of this metamorphism has been limited to between ~1450 and 1400 Ma based on Lu/Hf garnet growth ages (Aronoff *et al.,* 2012). Several observations about the distribution of aluminosilicate isograds help to further refine our understanding of the timing of deformation relative to metamorphism. First, the compilation of mapped metamorphic isograds presented here for both mountain ranges after the removal of post-Proterozoic deformation (Karlstrom and Daniel, 1993; Cather *et al.,* 2006; Jones *et al.,* 2011) shows that metamorphic isograds overprint fault boundaries (**Figure 3-1**). The trajectory of metamorphism in each region is different; however, these continuous isograds suggest that metamorphism did not conclude until after thrusting ceased. Second, the gently dipping nature of these isograds suggests, as Grambling (1981) pointed out, that isotherms were shallowly dipping, which implies that these tectonic blocks reached a local thermal equilibrium. Finally, the metamorphic

isograds show a map-scale gradient in P/T conditions. In the northern Tusas, textures record increasing temperatures across the pyrophyllite to kyanite and kyanite to andalusite isograds (**Figure 3-11**; Williams et al., 1999). Moving southward in the Tusas Mountains, the kyanite to sillimanite transition is crossed, indicating an increase in both pressure and temperature to the south (**Figure 3-11**). In the northern Picuris, aluminosilicate phase relationships record a P/T loop that passes above the aluminosilicate triple point (**Figure 3-11**; Daniel and Pyle, 2006). Directly south of this region, metamorphic conditions that pass through the triple point, as inferred by Grambling (1981) based on assemblages that contain all three aluminosilicates (**Figure 3-11**). Moving south from here in the Picuris, metamorphism passes below the triple point, going from kyanite to andalusite at pressures lower than those inferred in the northern Picuris. Continuing eastward, into the Rio Mora uplift and Rincon Range, crossing from the kyanite to sillimanite stability field represents metamorphism at pressures above the aluminosilicate triple point, with peak metamorphism crossing the second sillimanite isograd, locally producing migmitites (**Figure 3-11**; Read et al., 1999). One other isograd must be noted: the northeast-southwest striking isograd between the Picuris and Rio Mora areas, where sillimanite is to the northwest and kyanite is to the southeast. Although this appears to be contradictory to other isograds on the map, it can be explained by topography: lower topographic levels experienced higher pressures, the kyanite stability field, while higher topographic levels experienced lower pressures, where sillimanite would be stable.

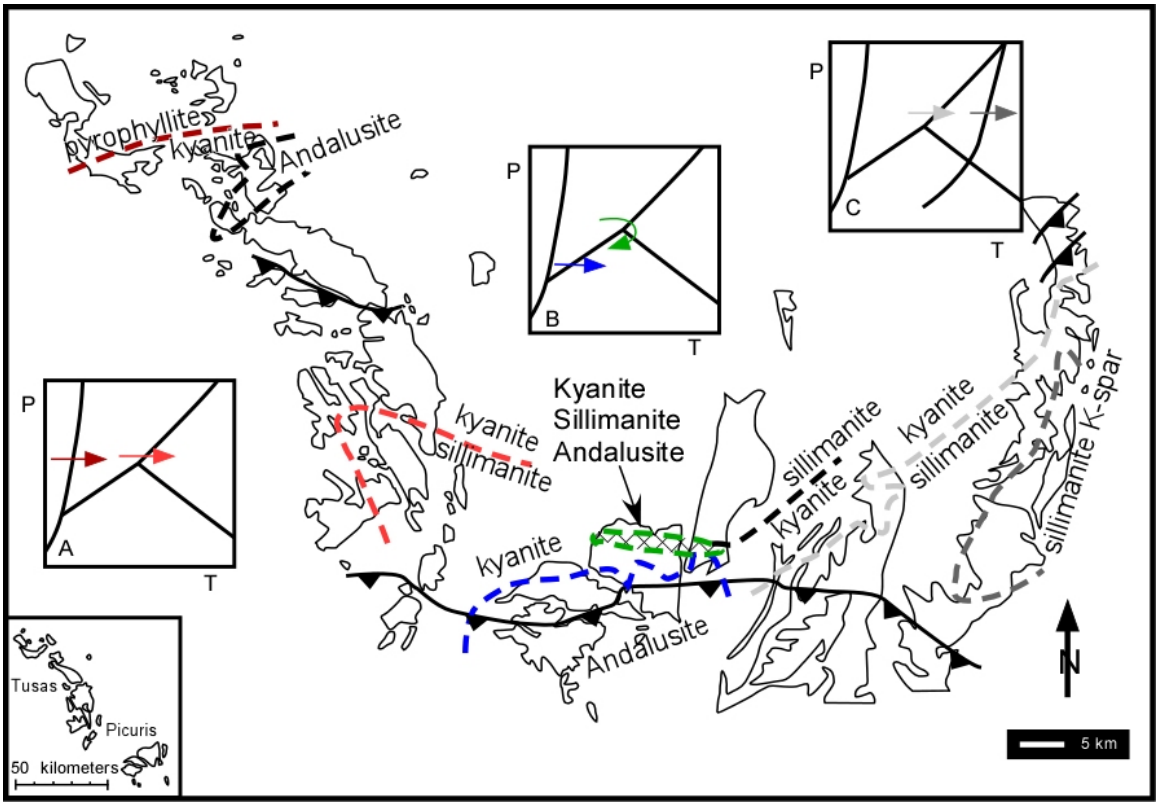

Figure 3-11: A tracing of the reconstructed Proterozoic belt in Northern New Mexico. Aluminosilicate isograds are shown with heavy dashed lines. The color of these isograds is used to correlate the transition with related arrows on inlaid schematic PT diagrams (A, B, C). In the schematic PT diagram (A), the dark red arrow represents the transitions in the northern Tusas from pyrophyllite to kyanite (Williams et al., 1999), and kyanite to andalusite. The orange arrow in (A) represents the transition in the south-central Tusas from kyanite to sillimanite. In the schematic PT diagram (B), the blue arrow represents the transition in the central Picuris from kyanite to andalusite. The green arrow represents metamorphism passing through the aluminosilicate triple point. In the same schematic PT diagram, the black arrow with dashed lines represents the PT path determined for the northern Picuris by Daniel and Pyle (2006). Finally, in the area of the Rio Mora uplift in the east, the schematic PT diagram (C), the light gray arrow corresponds to the transition from kyanite to sillimanite, while the dark gray arrow corresponds to the second sillimanite isograd, producing sillimanite + potassium feldspar assemblages (Read et al., 1999).

The gradient in metamorphic grade described above shows a continuous variation in pressure and temperature conditions across the reconstructed orogenic belt. The mapped isograds are relatively flat lying (Grambling 1981), and they also overprint Proterozoic deformation associated with the metamorphic event. Furthermore, P/T/ t loops for each region, summarized in **Figure 3-12** show the same P/T/t trajectory, characteristic of progressive loading during the formation of a fold and thrust belt (England *et al.*, 1984; Beaumont *et al.*, 2001). These observations strongly support the tectonic model proposed for this orogenic belt by Aronoff *et al.* (2012).

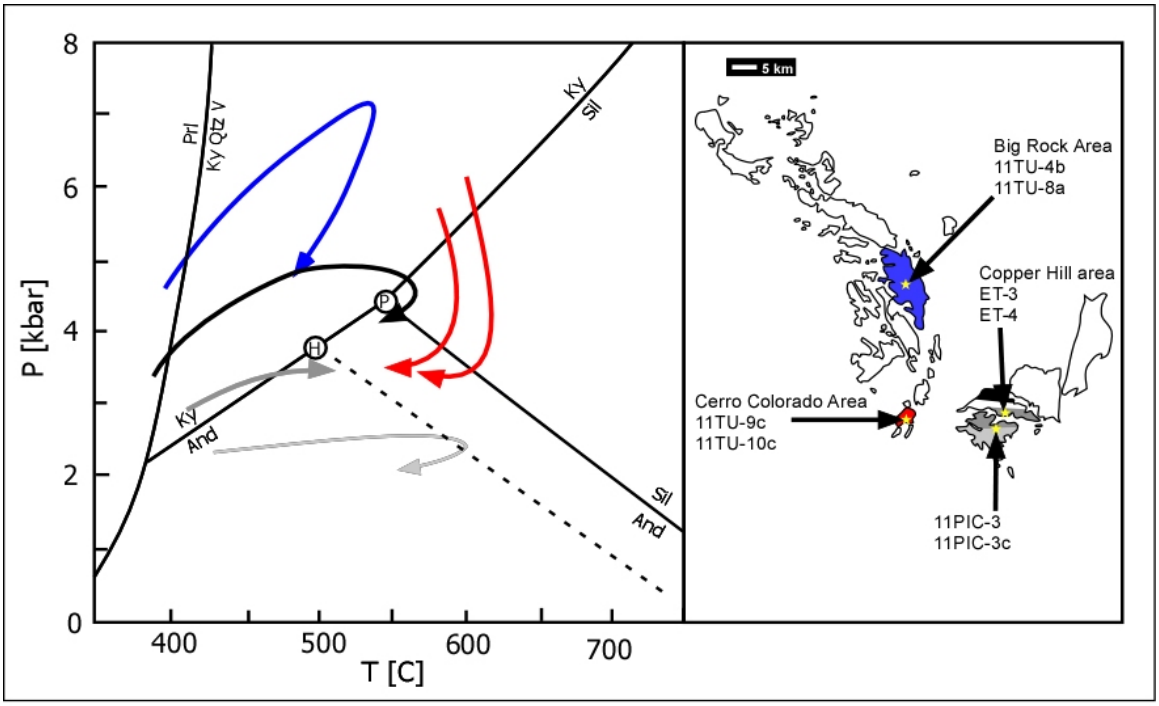

Figure 3-12: Left - A summary of all P/T/t curves from the central Tusas Mountains (blue), the southern Tusas Mountains (after Barnhart et al., 2012; red), the southern Picuris (after Williams et al., 1999; black), the central Picuris (Gray), and the northern Picuris (after Daniel and Pyle, 2006; green). Right - An outline of the Tusas and Picuris Mountain exposures with subsequent strike-slip deformation removed (after Karlstrom and Daniel, 1993; Cather et al., 2006; Jones et al., 2011). Here, sample locations are shown with yellow stars. Colored regions correspond to the color of the P/T/t path shown on the left.

Conclusions

Understanding the metamorphic history in the Tusas and Picuris Mountains is critical to the tectonic history of North America. In this paper, we present results that show that metamorphism in both the Tusas and the Picuris Mountains followed clockwise metamorphic trajectories consistent with a progressively loaded fold and thrust belt. Furthermore, we show that the variation in metamorphic grade moving from northwest to southeast in the orogenic belt is consistent with progressive north-vergent thrusting. Moving northward, tectonic blocks were uplifted from increasing depths, left to cool at the same crustal level after reaching peak metamorphic conditions. Compiled aluminosilicate isograds across the orogenic belt further emphasize the P/T gradient between east and west, supporting a petrogenesis based in a single metamorphic event.

Although several outstanding questions remain, such as the origin of the elevated geotherm in the region, our results are significant. Clockwise P/T/t paths throughout the orogenic belt highlight that this regional metamorphism is consistent with a single, contractional orogenic event. Furthermore, unbroken metamorphic isograds support the assertion that this metamorphism was associated exclusively with a single orogenic event. Finally, these results show that the triple point terranes found therein represent a single progressive metamorphic event.

References:

Aronoff, R.F., Vervoort, J.D., Andronicos, C.L., Hunter, R.A., 2012. Lu-Hf garnet geochronology and microstructural analysis constrain the timing of crustal assembly in southwestern North America: Geological Society of America Abstracts with Programs 44 (7), 525.

Barnhart, K.R., Walsh, P.J., Hollister, L.S., Daniel, C.G., Andronicos, C.L., 2012. Decompression during Late Proterozoic Al_2SiO_5 Triple-Point Metamorphism at Cerro Colorado, New Mexico. The Journal of Geology 120, 385–404.

Bauer, P.W., 1988. Precambrian geology of the Picuris Mountain, north-central New Mexico: New Mexico Bureau of Mines and Mineral Resources Open-File Report 325, 260.

Bauer, P.W., Williams, M. L., 1989. Stratigraphic nomenclature of Proterozoic rocks, northern New Mexico: revisions, redefinitions and formalization. New Mexico Geology 11, 45–52.

Bauer, P.W., 1993. Stratigraphic and structural evolution of Proterozoic rocks in the Picuris Range, Northern New Mexico. Journal of Geology 101, 483–500.

Bauer, P.W., Williams, M. L., 1994. The age of Proterozoic orogenesis in New Mexico, USA. Precambrian Research 67, 349–356.

Bauer, P. W., Kelson, K. I., 1997. Preliminary geologic map of the Taos SW 7.5-minute quadrangle. New Mexico Bureau of Geology and Mineral Resources Open File GM 12, scale 1:24 000.

Bauer, P.W., Kelson, K.I., Aby, S.B., 2005. Preliminary Geologic Map of the Penasco 7.5-minute quadrangle: New Mexico Bureau of Geology and Mineral Resources Open-File Report OF-GM 62, scale 1:24,000, 1 sheet.

Beaumont, C., Jamieson, R.A., Nguyen, M.H., Lee, B., 2001. Himalayan tectonics explained by extrusion of a low-viscosity crustal channel coupled to focused surface denudation. Nature 414, 738–742.

Bell, D. A., 1985. Structural and age relationships in the Embudo Granites, Picuris Mountains, New Mexico: M.S. thesis, University of Texas, Dallas, 175.

Berman, R. G., 1988. Internally-consistent thermodynamic data for minerals in the system Na2O–K2O–CaO–MgO–FeO–Fe2O3–Al_2O_3–SiO_2–TiO_2–H_2O–CO_2. Journal of Petrology 29, 445–522.

Bishop, J., 1997. The determination of a quantitative PT- t-D history for Proterozoic rocks of the Cerro Colorado area, north central New Mexico: M.S. thesis, Amherst, University of Massachusetts, 348.

Cather, S. M., Karlstrom, K. E., Timmons, J. M., and Heizler, M. T., 2006. Palinspastic reconstruction of Proterozoic basement-related aeromagnetic features in north-central New Mexico: implications for Mesoproterozoic to late Cenozoic tectonism. Geosphere 2 (6), 299–323.

Chernoff, C.B., Carlsom, W.D., 1997. Disequilibrium for Ca during growth of pelitic garnet. Journal of Metamorphic Geology 15, 421–438.

Daniel. C.G., Hollister, L.S., Parrish, R.R., Grujic, D., 2003. Exhumation of the Main Central Thrust from Lower Crustal Depths, Eastern Bhutan Himalaya. Journal of metamorphic Geology 21, 317–334.

Daniel, C.G., Pyle, J, 2006. Monazite-Xenotime Thermochronometry and Al_2SiO_5 Reaction Textures in the Picuris Range, Northern New Mexico, USA: New Evidence for a 1450-1400 Ma Orogenic Event. Journal of Petrology 47, 97–118.

Daniel, C. G., Jones, J.V. III., 2012. Unraveling the Mazatzal orogeny: Geochronologic constraints and speculation on the nature and timing of Paleoproterozoic and

Mesoproterozoic orogenesis in the Picuris Mountains, northern New Mexico. Geologic Society of America Abstracts with Programs 44 (6), 25.

Daniel, C.G., Pfeifer, L.S., Jones, J., McFarlane, C., 2012. Detrital zircon evidence for mesoproterozoic deposition, orogenesis and non-Laurentian Provenance in the Picuris Mountains, New Mexico, USA. Geological Society of America Abstracts with Programs 44 (7), 36.

de Capitani, C., Petrakakis, K., 2010. The computation of equilibrium assemblage diagrams with Theriak/Domino software. American Mineralogist 95, 1006–1016.

England, P.C., Thompson, A.B., 1984. Pressure-Temperature-Time Paths of Regional Metamorphism I. Heat Transfer during the Evolution of Regions of Thickened Continental Crust. Journal of Petrology 25, 894–928.

Grambling, J. A., 1979. Precambrian geology of the Truchas Peaks region, north-central New Mexico, and some regional implications. New Mexico Geological Society Guidebook, 30th Field Conference, 135–143.

Grambling, J. A., 1981. Kyanite, andalusite, sillimanite, and related mineral assemblages in the Truchas Peaks region, New Mexico. American Mineralogist 66**,** 702–722.

Grambling, J. A., Williams, M. L., 1985. The effects of Fe^{3+} And Mn^{3+} on aluminum silicate phase relations in north-central New Mexico, USA. Journal of Petrology 26, 324–354.

Holdaway, M. J., 1978. Significance of chloritoid-bearing andstaurolite-bearing rocks in the Picuris Mountains, New Mexico. Geological Society of America Bulletin 89, 1404–1414.

Holland, T., Powell, R., 1998. An internally consistent thermodynamic data set for phases of petrological interest. Journal of Metamorphic Geology 16, 309–334.

Holdaway, M. J., Goodge, J. W., 1990. Rock pressure vs. fluid pressure as a controlling influence on mineral stability: an example from New Mexico. American Mineralogist 75, 1043–1058.

Jones, J. V. III, Daniel, C. G., Frei, D., Thrane, K., 2011. Revised regional correlations and tectonic implications of Paleoproterozoic and Mesoproterozoic metasedimentary rocks in northern New Mexico, USA: New findings from detrital zircon studies of the Hondo Group, Vadito Group, and Marqueñas Formation. Geosphere 7, 974–991.

Karlstrom, K.E., Daniel, C.G., 1993. Restoration of Laramide right-lateral strike slip in northern New Mexico by using Proterozoic piercing points: Tectonic implications from the Proterozoic to the Cenozoic. Geology 21, 1139–1142.

Karlstrom, K.E., Williams, M.L., 1996. Looping *P-T* paths and high-*T*, low-*P* middle crustal metamorphism: Proterozoic evolution of the southwestern United States. Geology 24, 1119–1122.

Karlstrom, K. E., Dallmeyer, R. D., Grambling, J. A., 1997. 40Ar/39Ar evidence for 1.4 Ga regional metamorphism in New Mexico: implications for thermal evolution of lithosphere in Southwestern USA. Journal of Geology 105, 205–223.

Karlstrom, K. E., Amato, J. M., Williams, M. L., Heizler, M., Shaw, C., Read, A., Bauer, P., 2004. Proterozoic tectonic evolution of the New Mexico region: a synthesis. *In*: Mack, G. H. & Giles, K. A. (Eds), The Geology of New Mexico. New Mexico Geological Society Special Publication 11, 1–34.

Larson, T.E., Sharp, Z.D., 2003. Stable isotope constraints on the Al_2SiO_5 'triple-point' rocks from the Proterozoic Priest pluton contact aureole, New Mexico, USA. Journal of metamorphic Geology 21, 785–798.

Lombardi, C.E., 1997. Proterozoic geology of the Las Madera Quadrangle, north-central New Mexico: M.S. thesis, Amherst, University of Massachusetts, 100.

Long, L. E., 1974. Contrasting types of Precambrian granitic rocks in the Dixon–Penasco area, northern New Mexico. New Mexico Geological Society Guidebook 25, 101–108.

McCoy, A.M., Karlstrom, K.E., Shaw, C.A., Williams, M.L., 2005. The Proterozoic ancestery of the Colorado Mineral Belt: 1.4 Ga shear zone system in central Colorado. *In:* Karlstrom, K.E., Keller, G.R. (Eds.), The Rocky Mountain Region – An Evolving Lithosphere: Tectonics, Geochemistry and Geophysics: Geophysics Monograph Series 154, 71–90.

Montgomery, A., 1953. Precambrian geology of the Picuris Mountains, north-central New Mexico. New Mexico Bureau of Mines and Mineral Resources Bulletin 30, 89.

Pattison, D. R. M., 1992. Stability of andalusite and sillimanite and the Al_2SiO_5 triple point: constraints from the Ballachulish aureole, Scotland. Journal of Geology 100, 423–446.

Pedrick, J. N., Karlstrom, K. E.,Bowring, S. A., 1998. Reconciliation of conflicting tectonic models for Proterozoic rocks of northern New Mexico. Journal of Metamorphic Geology 16, 687–707.

Price, N.A., 2007. Petrology, structural geology and significance of Mn-andalusite from the lower Ortega Quartzite, Tusas Mts., NM, USA: M.S. thesis, Amherst, University of Massachusetts, 322.

Rao, B. B., Johannes, W., 1979. Further data on the stability of staurolite and quartz and related assemblages. Neues Jahrbuch für Mineralogie, Monatshefte 10, 437–447.

Read, A., Karlstrom, K. E., Grambling, J. A., Bowring, S. A., Heizler, M., Daniel, C., 1999. A mid-crustal cross section from the Rincon Range, northern New Mexico: Evidence for 1.68 Ga pluton-influenced tectonism and 1.4 Ga regional metamorphism. Rocky Mountain Geology 34, 67–91.

Schreyer, W., Chiner, G.A., 1966. Staurolite-quartzite bands in kyanite quartzite at Big Rock Rio Arriba County, New Mexico. Contributions to Mineralogy and Petrology 12 (3), 223–244.

Shaw, C.A., Karlstrom, K.E. Williams, M.L., Jercinovic, M.J., McCoy, A.M., 2001. Electron microprobe monazite dating of ca. 1.71 - 1.65 Ga and ca. 1.45–1.38 Ga

deformation in the Homestake Shear Zone, Colorado: Origin and early evolution of a persistent intracontinental tectonic zone. Geology 29 (8), 739–742.

Shaw, C.A., Heizler, M.H., Karlstrom, K.E., 2005. 40Ar/39Ar Thermochronologic Record of 1.45–1.35 Ga Intracontinental Tectonism in the Southern Rocky Mountains: Interplay of Conductive and Advective Heating with Intracontinental Deformation. *In* Karlstrom, K.E., Keller, G.R. (Eds.), The Rocky Mountain Region - An Evolving Lithosphere Tectonics, Geochemistry, and Geophysics: Washington, D.C., American Geophysical Union Monograph 154, 163–184.

Simmons, M. C., Karlstrom, K. E., Williams, M. W., Larson, T. E., 2011. Geology and mineral resources in the Hopewell and Bromide No. 2 districts, northern Tusas Mountains, Rio Arriba County, New Mexico. *In* Koning, D. J., Karlstrom, K. E., Kelley, S. A., Lueth, V. W., Aby, S. B. (Eds.), Geology of the Tusas Mountains and Ojo Caliente. New Mexico Geologic Society Guidebook, 359–378.

Soegaard, K., Eriksson, K.A., 1985. Evidence of tide, storm, and wave interaction on a Precambrian siliciclastic shelf: The 1,700 m.y. Ortega Group, New Mexico. Journal of Sedimentary Petrology 55, 672–684.

Williams, M.L., Grambling, J.A., 1990. Manganese, ferric iron, and the equilibrium between garnet and biotite. American Mineralogist 75, 886–908.

Williams, M.L., 1991. Heterogeneous deformation in a ductile fold-thrust belt: The Proterozoic structural history of the Tusas Mountains, New Mexico. Geological Society of America Bulletin 103, 171–188.

Williams, M.L., Karlstrom, K.E., Lanzirotti, A., Read, A.S., Bishop, J.L., Lombardi, C.E., Pedrick, J.N., Wingsted, M.B., 1999. New Mexico middle-crustal cross sections: 1.65-Ga macroscopic geometry, 1.4 Ga thermal structure, and continued problems in understanding crustal evolution. Rocky Mountain Geology 34, 53–66.

Tables:

	11PIC-3	11TU-4B
SiO_2	64.35	60.76
TiO_2	0.810	0.544
Al_2O_3	14.05	19.22
FeO_{tot}	14.95	7.55
MnO	2.205	0.138
MgO	1.57	2.15
CaO	0.18	0.41
Na_2O	0.14	0.48
K_2O	1.29	5.25
Sum	99.55847	96.49939
LOI (%)	-0.04	3.13

Table 3-1: XRF analysis, conducted at Washington State University, of both deformed and weakly deformed samples. Major elements are shown as non-normalized weight per cents.

	grt	qtz	plag	bt	chl	ctd	musc	marg	staur	sill	and	ky	tourm	epidote
11TU4-B	X	X		X	X		X	X	X					X
11TU9-C	X	X	X	X			X		X	X			X	
11TU-10C	X	X	X	X			X		X	X			X	
11PIC-3 ET-4	X	X X		X	X	X	X X		X		X	X		
ET-3		X				X	X				X	X		

Table 3-2: A list of minerals present in samples collected in the Tusas and Picuris Mountains.

Number	Plag	Ilm	Grt	Chl	Musc	Parag	Bt	Cz	Qtz	Zo	And	Sil	Ky	Staur	Marg	Ctd
1	X	X	X	X	X		X	X	X							
2	X	X	X	X	X		X		X	X						
3	X	X	X	X	X		X		X							
4	X	X	X		X		X		X		X					
5	X	X	X		X		X		X			X				
6	X	X	X		X		X		X					X		
7		X	X		X		X		X					X	X	
8		X	X		X		X		X						X	X
9		X	X	X	X		X		X						X	X
10		X	X	X	X		X		X						X	
11	X	X	X	X	X		X		X						X	
12		X	X	X	X		X		X	X						
13		X	X	X	X		X	X	X							
14		X	X	X	X	X	X	X	X							
15		X	X	X	X	X	X		X	X						
16		X	X	X	X		X		X	X						X
17		X	X		X		X		X	X						X
18		X	X		X		X		X							X
19		X	X		X		X		X					X		
20		X	X		X		X		X				X			
21	X	X	X		X		X		X				X			

Table 3-3: Minerals present in each equilibrium assemblage field for the isochemical phase diagram of sample 11TU-4B (see Figure 3-6).

		11PIC-3					
		Grt		Musc	Chl	Biot	Staur
		Rim	Core				
Weight Percent	Na_2O	0.05	0.06	1.17	0.1	0.23	0.04
	MgO	2.59	1.98	0.46	14.08	9.79	1.49
	MnO	6.11	6.39	0.01	0.15	0.08	0.26
	CaO	0.21	0.68	0.03	0.04	0.04	0
	SiO_2	37.5	38.25	46.9	24.76	35.68	29.77
	$Al2O_3$	21.45	20.74	34.76	23.61	19.49	52.32
	FeO_{tot}	34.4	33.72	0.67	25.03	18.91	13.27
	K_2O	0.01	0.02	9.2	0.07	8.72	0.01
	TiO_2	0.02	0.07	0.27	0.08	1.53	0.45
	Total	102.34	101.91	93.47	87.93	94.47	97.61
O in unit formula		12	12	22	28	22	48
Cations in unit formula	Na_2O	0.01	0.01	0.3	0.04	0.07	0.02
	MgO	0.31	0.23	0.09	4.4	2.22	0.64
	MnO	0.41	0.43	0	0.03	0.01	0.07
	CaO	0.02	0.06	0	0.01	0.01	0
	SiO_2	2.98	3.05	6.29	5.19	5.44	8.49
	Al_2O_3	2.01	1.95	5.51	5.83	3.5	17.92
	FeO	2.29	2.25	0.08	4.39	2.41	3.22
	K_2O	0	0	1.58	0.02	1.69	0
	TiO_2	0	0	0.03	0.01	0.17	0.1

Table 3-4: Microprobe WDS mineral analyses and structural formulas for samples 11TU-8A, 11TU-4B, and 11PIC-3. Analyses for matrix minerals are presented here. Analyses were conducted on a JEOL8900 microprobe at Cornell University using an accelerating voltage of 15 KeV, a probe current of 20 nA, and a beam diameter of 10 µm for micas and 2 µm for other minerals. A minimum of 10 analyses were averaged for each mineral to produce an average mineral composition for the sample.

Number	Grt	Musc	Parag	Chl	Ctd	Rt	Qtz	Ilm	Bt	Staur	Crd	Plag
1	X	X	X	X	X	X	X					
2	X	X	X	X	X		X	X				
3	X	X		X	X		X	X	X			
4	X	X			X		X	X	X			
5	X	X		X			X	X		X		
6	X	X					X		X		X	
7	X	X					X		X		X	X
8	X	X		X	X	X	X					

Table 3-5: Minerals present in each equilibrium assemblage field for the isochemical phase diagram of sample 11PIC-3 (see Figure 3-10).

4. Tectonic implications of Proterozoic U/Pb crystallization ages in the southwestern United States

Abstract

The recent identification of the ~1.4 Ga Picuris Orogeny in northern New Mexico requires a reexamination and reinterpretation of pre-existing geochronolgical data. Here, we present a compilation of previously published U/Pb concordia zircon ages from across the southwest United States. Using this dataset, we evaluate spatial trends in the distribution of plutonic ages within the reference frame of the Picuris Orogeny. An estimate of the geographic location and extent of the Picuris Orogeny is made using a combination of detrital zircon ages, Lu/Hf garnet geochronology, and Ar/Ar cooling ages. The detrital zircon ages identified regions that experienced deposition and subsequent burial prior to ~1.45 Ga, whereas garnet ages and Ar cooling ages identified regions that experienced high grade metamorphism at ~1.4 Ga. Using this estimated location for the orogeny, the spatial distribution of U/Pb zircon ages is reevaluated.

Results of this study show several important characteristics of Proterozoic plutonism in the southwest US. First, as has been previously documented, there is a ~100 Ma gap in plutonism between 1600 and 1500 Ma in the region. Second, the dataset of ages over 1600 Ma shows that plutons young from northwest to the southeast, consistent with magamatism during the Yavapai and Mazatzal orogenies. Analysis of this trend shows a discontinuity in the trend that coincides with the southern edge of the Yavapai-

Mazatzal transition zone. This offset results in two populations, each with a similar relationship between age and location, but with the population of data to the southeast of the orogeny having a regression intercept that is 9 Ma younger than the population to the northwest. Third, the data set of ages between 1400 and 1500 Ma shows a spatial trend in plutonic age where age increases to the southeast.

The implication of these spatial trends in plutonic age across the southwest have bearing on our understanding of the Proterozoic tectonic history of the southwest, and the origins of the enigmatic ~1.4 Ga A-type magmatic episode. First, the trends recorded by plutons over 1600 Ma are indicative of arc migration, consistent with previously reported rates for slab roll back. Second, the discontinuity in this trend that coincides with the northwestern extent of the Picuris Orogeny may record localized shortening along the margin of the orogen. Third, the trend in pluton ages between 1400 and 1500 Ma is not consistent with arc migration; instead, plutonism occurred relatively contemporaneously across the region, yielding a trend with a very shallow slope. The A-type chemical composition of these plutons, reports of crustal contamination in some locales, as well as new evidence for crustal thickening during the Picuris Orogeny, is consistent with melt production by crustal over-thickening followed by thermal relaxation and crustal melting.

Introduction

The tectonic evolution of a continent is the result of complex interactions between deformation, metamorphism, plutonism and sedimentation. Understanding how these processes work to shape an evolving continent is a central goal of the geologic community. In the case of North America, it has been generally accepted that between 2

and 1 Ga, continental growth involved lateral accretion of juvenile island arcs to the southern margin of Laurentia, producing a swath of crust stretching roughly 1000 km across strike (Karlstrom et al., 2004 and references therein). Accretion began in the north with the Trans-Hudson and Penokean orogenies between 1.9 and 1.8 Ga (Hoffman, 1989), followed by subsequent accretion, including the Yavapai orogeny from 1.8 to 1.7 Ga and the Mazatzal orogeny from 1.7 to 1.6 Ga (Figure 4-1; Silver *et al.*, 1977; Van Schmus and Bickford, 1981; Nelson and DePaolo, 1985; Bennett and DePaolo, 1987; Van Schmus *et al.*, 1987, 1993; Karlstrom and Bowring, 1993; Magnani *et al.*, 2004). Punctuating these periods of continental growth are periods of voluminous plutonism during the Paleoproterozoic and Mesoproterozoic (Figure 4-2).

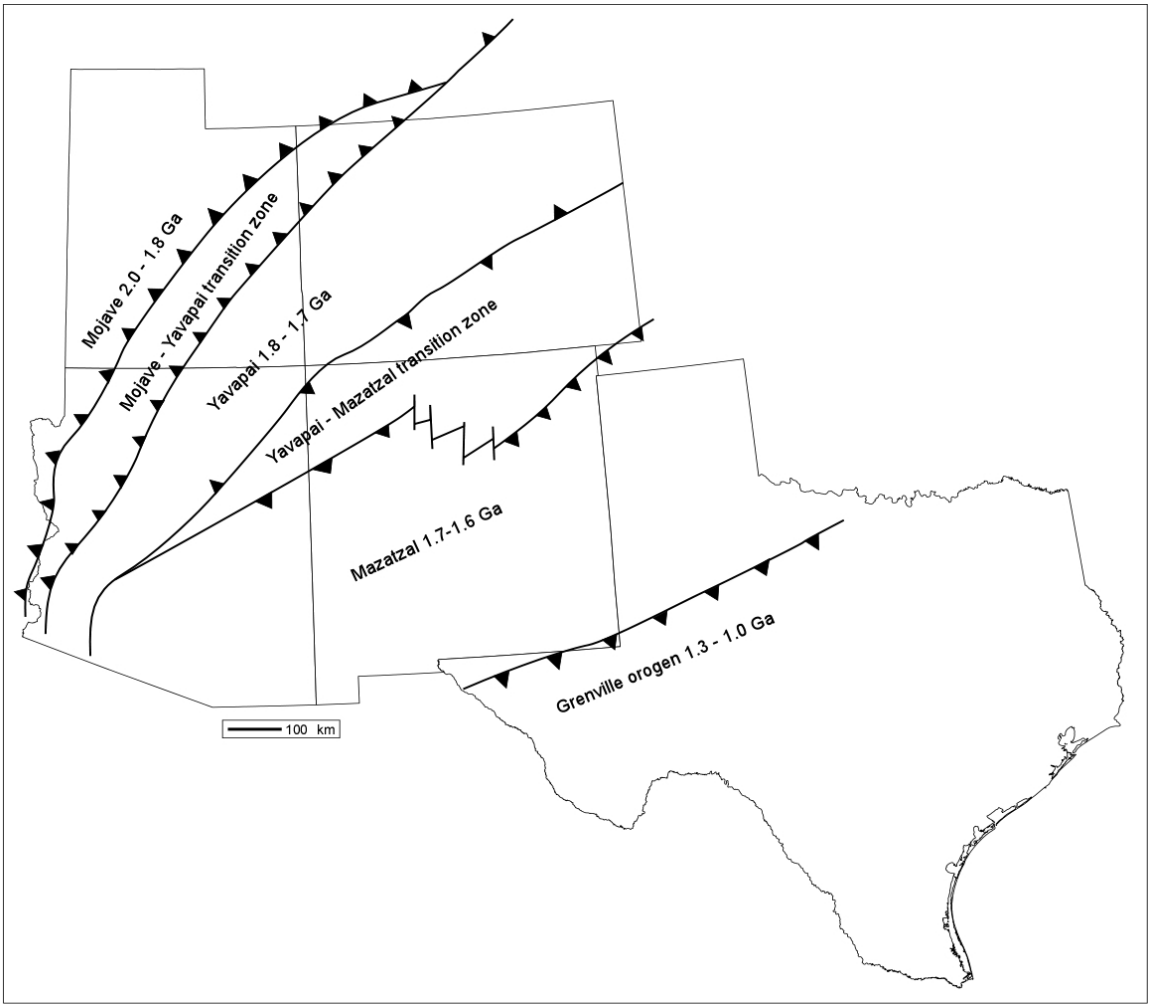

Figure 4-1: A schematic map of the southwest United States showing the traditionally accepted tectonic boundaries after Shaw and Karlstrom (1999), beginning with the Mojave in the northwest between 2.0 and 1.8 Ga, and ending with the Grenville between 1.3 and 1.0 Ga. Heavy black lines represent deformation fronts between terranes.

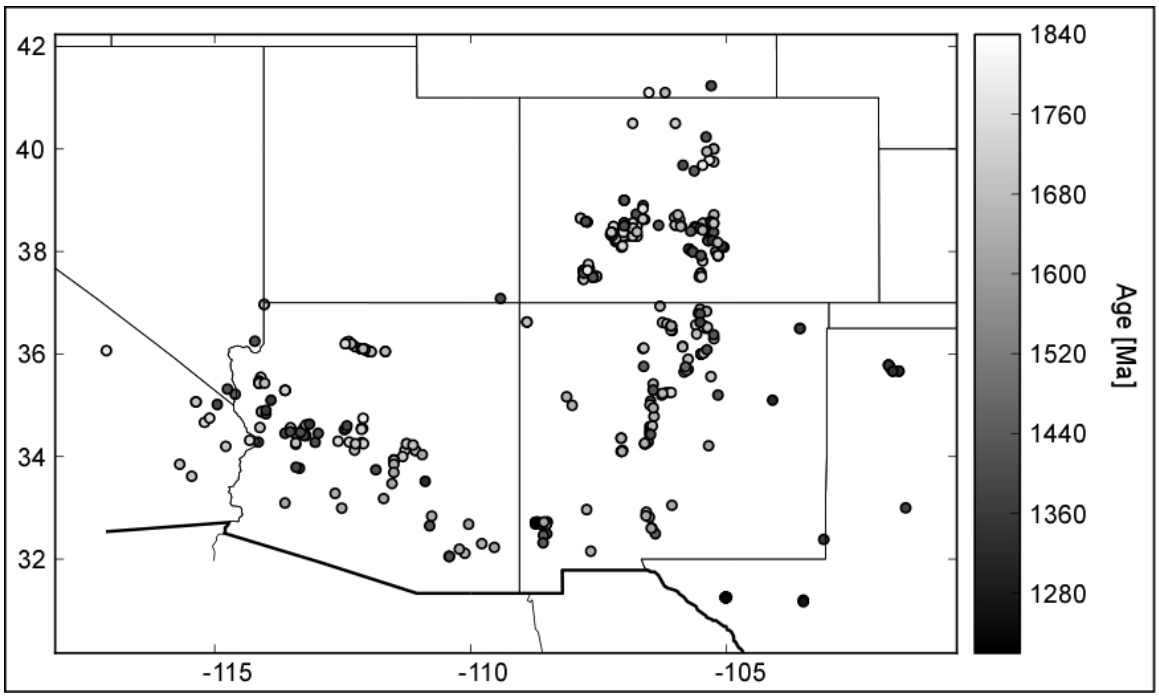

Figure 4-2: A schematic geologic map of the southwest US. Plutons are shown in grayscale, with darker colors corresponding to younger plutons.

In the Four Corners region of the southwestern United States, distinct Paleo- and Mesoproterozic magmatic events are separated by a ~100 Ma period of magmatic quiescence between 1600 and 1500 Ma. The Mesoproterozic plutons perforate the southwest United States, comprising as much as 20 to 30% of the exposed basement in the region (Anderson, 1983), and have largely been viewed as a single magmatic event stretching from 1480 Ma to 1350 Ma. Understanding the origins of the Mesoproterozic plutons and their relation to the tectonic evolution of Laurentia is central to developing a model for continental growth and rejuvenation. The origin of the Mesoproterozic suite of plutons remains enigmatic. Geochemical studies infer a hot spot or extensional tectonic setting (e.g. Loiselle and Wones, 1979; Anderson, 1983; Frost and Frost, 2011). In contrast, structural studies have inferred a compressional stress field, with varying, but locally intense deformation associated with 1.4 Ga plutons (e.g. Nyman et al., 1994; Kirby et al., 1995; Duebendorfer and Christensen, 1995; Karlstrom and Williams, 1995; Nyman et al., 1997; Ferguson et al., 2004).

Recently, the tectonic history of Proterozoic Laurentia was revised with the identification of the Picuris Orogeny (referred to as PO throughout the remainder of this chapter) in northern New Mexico at 1.4 Ga (Daniel and Pyle, 2006; Daniel and Jones, 2012; Aronoff *et al.*, 2012; Daniel *et al.*, in press). The timing of this newly recognized orogenic event was constrained using detrital zircon, monazite and Lu/Hf garnet geochronology. This newly identified tectonic event is a previously unrecognized contractional tectonic event in southwestern North America. In this paper, we revisit previously published geochronologic datasets with this new geologic context. Analysis of the spatial distribution of dated plutons shows two significant trends in ages with respect

to the orientation of the Picuris Orogeny. Using the results of this analysis in combination with published detrital zircon and Ar/Ar cooling age studies, we constrain the location of the Picuris Orogeny and further describe the nature of the orogenic event. Furthermore, we use this new tectonic setting and trends observed in Mesoproterozic plutons to further the discussion of the origin of these igneous bodies, proposing an alternative model for their melt generation.

Geologic Background

Traditional tectonic evolution of Proterozoic North America

The accepted model for the growth of Laurentia during the Proterozoic involves repeated accretion of off-board terranes to the southern margin of the Archean Wyoming craton. Sm-Nd isotopic studies of these terranes have shown that they are first generation, mantle-derived juvenile crustal additions (e.g. Nelson and De Paolo, 1985). Accretion began with the Mojave province, followed by the Yavapai between 1.8 and 1.7 Ga and the Mazatzal between 1.7 and 1.6 Ga. After 500 Ma of relative quiescence, a final stage of accretion along the southern margin of this continent occurred during the Grenville orogeny. This long-lived period of continental growth produced a ~1000 km wide swath of juvenile crust stretching from Wyoming to Mexico (Karlstrom et al., 2004 and references therein). Mesoproterozic Plutons are viewed as being intraplate, possibly related to convergence along the proto-Grenville plate margin. There, chemistry of the plutons and lack of obvious chemical or age trends has made their genesis enigmatic.

Recent identification of the Picuris Orogeny

Although the tectonic history described above has generally been accept, details remain controversial. For over thirty years, the tectonic history of the Four Corners region between 1.7 and 1.4 Ga has been disputed. In northern New Mexico and southern Colorado, wide-spread regional amphibolite facies metamorphism has been explained by competing tectonic models (e.g. Grambling, 1981; Karlstrom and Williams, 1996;Williams et al., 1999; Daniel and Pyle, 2006; Aronoff et al., 2012; Hunter et al., 2012). One of the most widely cited tectonic models was proposed by Karlstrom and Williams (1996). In northern New Mexico, most deformation and metamorphism occurred during the Mazatzal orogeney between ~1.7 and 1.6 Ga. Rocks of northern New Mexico then cooled to a steady state geotherm and remained in the mid-crust. The region was then reheated during emplacement of ca. 1.4 Ga plutons. Deformation associated with Mesoproterozic plutons is attributed to far field stresses affecting the thermally softened aureoles of the plutons. In contrast, Daniel and Pyle (2006) showed that in the Picuris Mountains of northern New Mexico there is only evidence for only one metamorphic event between 1440 and 1390 Ma, based on monazite geochronology. This was a view point championed earlier by Grambling (1981) and Grambling and Dallmeyer (1993), although these authors favored late orogenic extension for the tectonic setting.

The evidence for the contrary model, the Picuris Orogeny, is outlined here. First, 40Ar/39Ar ages from northern New Mexico have ages younger than 1.4 Ga (e.g. Grambling and Dallmeyer, 1993). In a comprehensive study of Ar cooling ages, Shaw et al., 2005 showed that most of northern New Mexico and part of southeastern Colorado

experienced temperatures over 500 ^{o} C until ~1.4 Ga. Shaw et al., 2005 argued that this amphibolite facies metamorphic event was due to heat advection by 1.4 Ga plutons.

Second, metamorphic monazite ages indicate metamorphic mineral growth in the amphibolite facies between 1430 and 1400 Ma (Pedrick et al., 1998; Daniel and Pyle, 2006; Shaw et al., 2005). In an integrated microstructural and geochronologic study, Daniel and Pyle (2006) dated monazite inclusions Al_2SiO_5 polymorphs from the northern Picuris Mountains. In this study, the authors showed that the earliest aluminosilicate, lineated kyanite, contained monazite inclusions with concordant U/Pb ages of 1434 +/- 12 Ma. They also reported concordant and near concordant monazite ages that extended to 1390 +/- 20 Ma. They argued that these ages were consistent with a single metamorphic event between 1434 Ma and 1390 Ma in the Picuris Mountains.

Third, Jones et al. (2011) analyzed detrital zircons and found that deposition of the Marquenas conglomerate in the southern Picuris Mountains of northern New Mexico occurred until 1460 Ma based on statically significant populations detrital zircon. This requires that the Marquenas formation was being supplied with detritus at the surface of the earth as late as ~1460 Ma. A similar detrital zircon study published by Doe et al. (2012) showed that the Yankee Joe and Black Jack basins of Arizona also experienced sedimentation until ~1450 Ma. Daniel et al. (in press) have extended this work, showing that the Piedra Lumbre schist and Pilar Phyllite both have protolith ages younger than 1480 Ma, again requiring sedimentation of metamorphic protoliths just prior to metamorphism.

Fourth and finally, Aronoff et al. (2012) used Lu/Hf isotopic dating of garnet to constrain the timing of the onset of metamorphism in both the Picuris and Tusas Mountains to have occurred after 1456 Ma. This is a particularly significant result because these garnet ages overlap detrital zircon ages, requiring metamorphism to have occurred with a few millions years of deposition of the Marquenas formation. Daniel et al., (in press) argued based on these lines of evidence that northern New Mexico experienced major contractional deformation between 1460 and 1400, and termed this the Picuris Orogeny.

Plutonism in the Mesoproterozoic

Overlapping in time with the Picuris Orogeny, ubiquitous plutonism was occurring, eventually contributing an estimated 20% to 30% of the crust across the region (Anderson, 1983). Plutons in the Four Corners region have crystallization ages spanning from older than 1900 Ma, down to 1100 Ma and younger. However, three periods of particularly voluminous plutonism occurred between 1800 and 1700 Ma, again between 1700 and 1600 Ma, and again between 1500 and 1400 Ma. Furthermore, the chemistry of plutons from the third, younger pulse of magmatism is largely A-type (Loiselle and Wones, 1979; Anderson, 1983), or Ferroan (Frost and Frost, 2011) granites, which are traditionally associated with rifting and extensional settings. However, structures in and around 1500 to 1400 Ma plutons have been documented as showing contractional or transpressional fabrics (e.g. Kirby et al., 1994; Nyman et al., 1994; Karlstrom and Williams, 1995; Nyman et al., 1997; Amato et al., 2011). These contradicting lines of evidence have led to significant controversy over the origins of this massive pulse of magmatism. Further complicating the picture, A-type plutonism spanning from 1500 to

1350 Ma has been documented from California, through the US, into Labrador (Anderson, 1983).

Explanations for the conflicting chemical and structural characteristics of these plutons have produced numerous possible models of their origins (e.g. Anderson, 1983; Clemens et al., 1986; Foley et al., 1987; Landenberger and Collins, 1996; Anderson and Bender 1989; Frost and Frost, 1997; Duchesne et al., 1999; Vigneresse, 2005). These explanations have ranged from delamination of over thickened crust (e.g. Thompson, 1999), to thermal instability and an inverse plume below a super continent (e.g. Vigneresse, 2005). Previously, no spatial trends have been identified to lend insight into how these plutons fit into the evolutionary story of Laurentia (Anderson, 1983). Although a significant amount of work and body of knowledge exists regarding these plutons, how they relate to the tectonic history of Laurentia remains largely ambiguous, particularly in light of a contemporaneous orogenic event at ~1.4 Ga.

Methods

In order to evaluate the spatial distribution of plutons through time across the southwest United States, we plot reported U/Pb zircon crystallization ages, omitting inherited components and xenolithic samples, on a map of the southwest United States (Figure 4-2). The data, including the location, age, error, and lithology is presented in Appendix 1. For the references used to construct the database, see Appendix 2.

We plotted the U/Pb crystallization ages against distance from the southern extent of the Yavapai-Mazatzal transition zone as defined by Karlstrom and Daniel (1993). The southern extent of the transition zone coincides well with the distribution of

Mesoproterozic basins identified by detrital zircon studies, $^{40}Ar/^{39}Ar$ cooling age data, and distribution of Lu/Hf garnet ages indicate that the PO affected regions to the south and east of this boundary (Figure 4-3). The northern extent of the PO is best defined in northern New Mexico and southern Colorado, and is constrained in Arizona only by the Yankee Joe-Black Jack basins, which require sedimentation, burial and metamorphism post 1450 Ma (Doe et al., 2012).

The across-strike distance between each sample and the samples age was plotted by minimizing the distance between each point and the reference line using the haversine distance, calculated using Python (see Appendix 3 for code). The margin is slightly curvilinear, so for the purposes of simplifying the computing process, it was approximated as a series of linear segments. The minimum distance to each of these segments was calculated for each point, and from these, the global minimum distance to the deformation front was selected for each sample.

Regression lines for the data were determined using the Regression function in the data analysis package of Microsoft Excel. A P-value of 0.05 was used as a test of statistical significance, with P-values less than or equal to 0.05 being statistically significant. Pearson Correlation Coefficients (PCC) were also used in order to evaluate the probability that X, in this case distance, and Y, in this case age, are related. A PCC value of +/-0.5 or greater is considered a strong correlation between variables, with +/-0.4 being moderately strong (Rodgers and Nicewander, 1988; Buda and Jarynowski, 2010). A p value (referred to as a PCCp) for each PCC is also calculated, and represents the statistical significance of the correlation, with values between 0.05 and 0 being statistically significant (Rodgers and Nicewander, 1988; Buda and Jarynowski, 2010).

Error was not accounted for in this statistical analysis because such a study would require a rigorous statistical methodology that is beyond the scope of this dissertation.

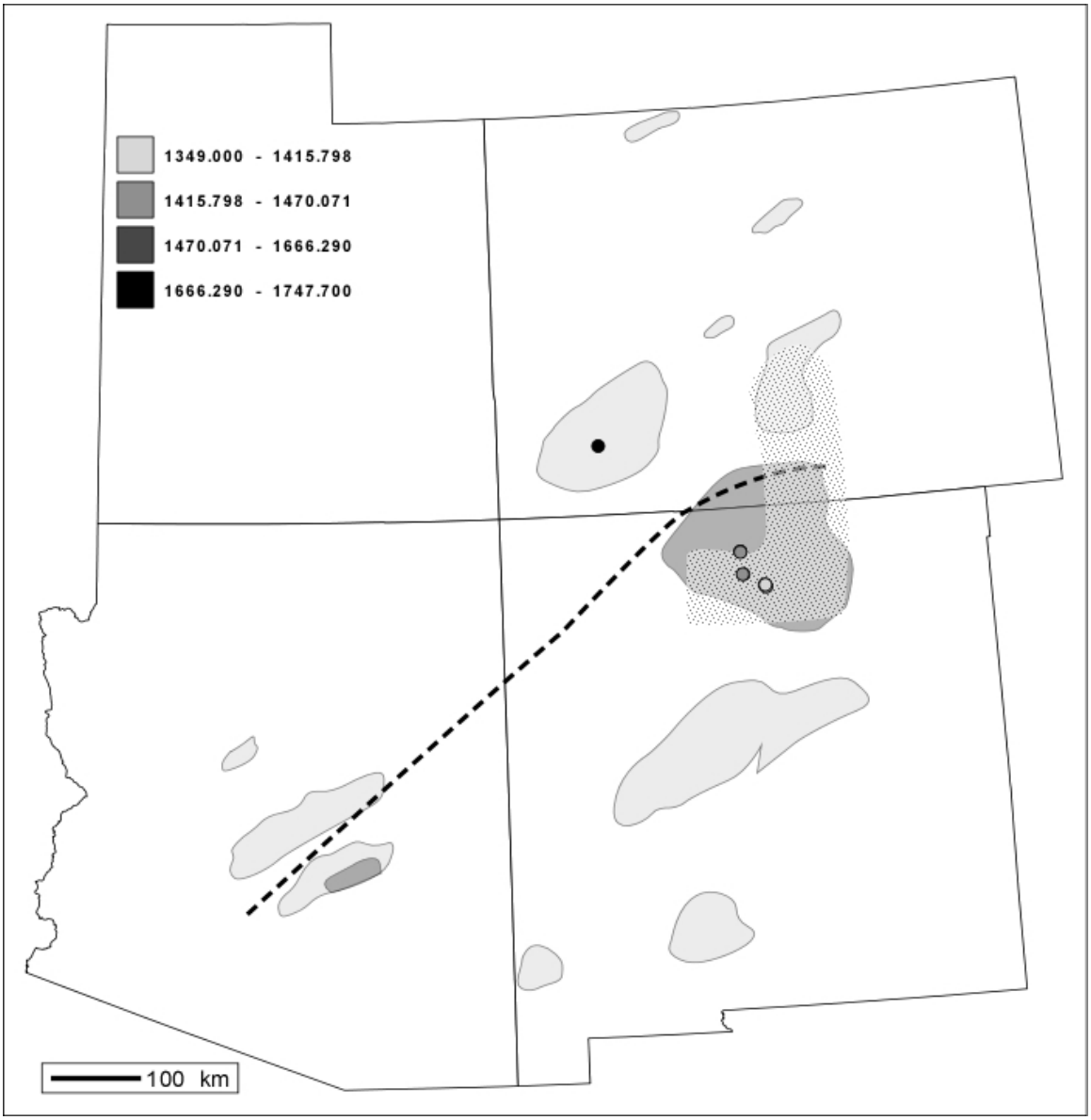

Figure 4-3: A schematic map of the southwest US showing constraints used to identify the approximate boundary of the Picuris Orogeny. Shaded in gray are Proterozoic basins (after Jones et al., 2011; Doe et al., 2012), with light gray representing basins over 1.6 Ga in age, and dark gray representing basins of ages between 1.4 and 1.45 Ga. The area shaded with a stippled pattern is inferred to have experienced temperatures over 500 C at 1.4 Ga based on Ar/Ar cooling ages (Shaw et al., 1999). Finally, circles colored with gray scale represent Lu/Hf garnet ages, with darker colors corresponding to older ages. The dashed line is the boundary separating basins over 1.6 Ga, and garnet ages over 1.6 Ga from younger ages, and is the estimated location of the Picuris Orogeny.

Results

Older Plutons

There are two distinct groups of zircon crystallization ages: igneous bodies older than 1600 Ma, and igneous bodies younger than 1500 Ma. These groups are separated by a ~100 Ma magmatic gap (Figure 4-4). Fitting a linear regression to the older dataset yields a slope of -0.17 Ma/km and an intercept of 1708 km (Figure 4-5). Although there is clearly a correlation between age and distance from the PO in this older dataset, it is not necessarily the case that these data represent a single trend. Visual inspection of this distribution suggests that there may be two distinct populations within this distribution. One population defined by ages at distances less than ~0 (i.e. to the northwest) from the PO is characterized by a distribution of ages that is uniform above and below the trend line. In contrast, at distances greater than ~0 km, there are significantly fewer ages older than the regression line, with the vast majority of ages below the regression line (Figure 4-6).

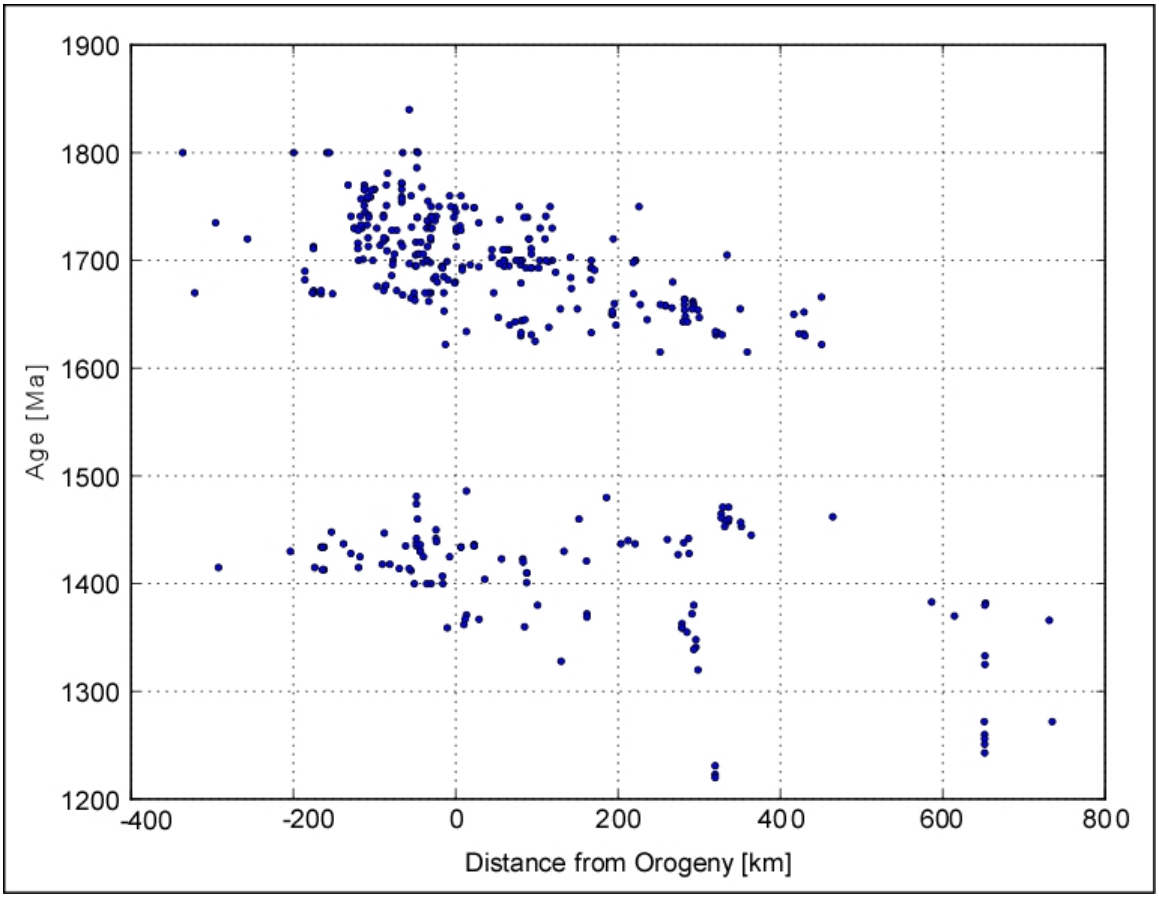

Figure 4-4: A scatter plot showing age [Ma] on the y-axis and distance from the PO [km] on the x-axis for 378 plutons in the southwest US. Negative distances are to the north and west, and positive distances to the south and east.

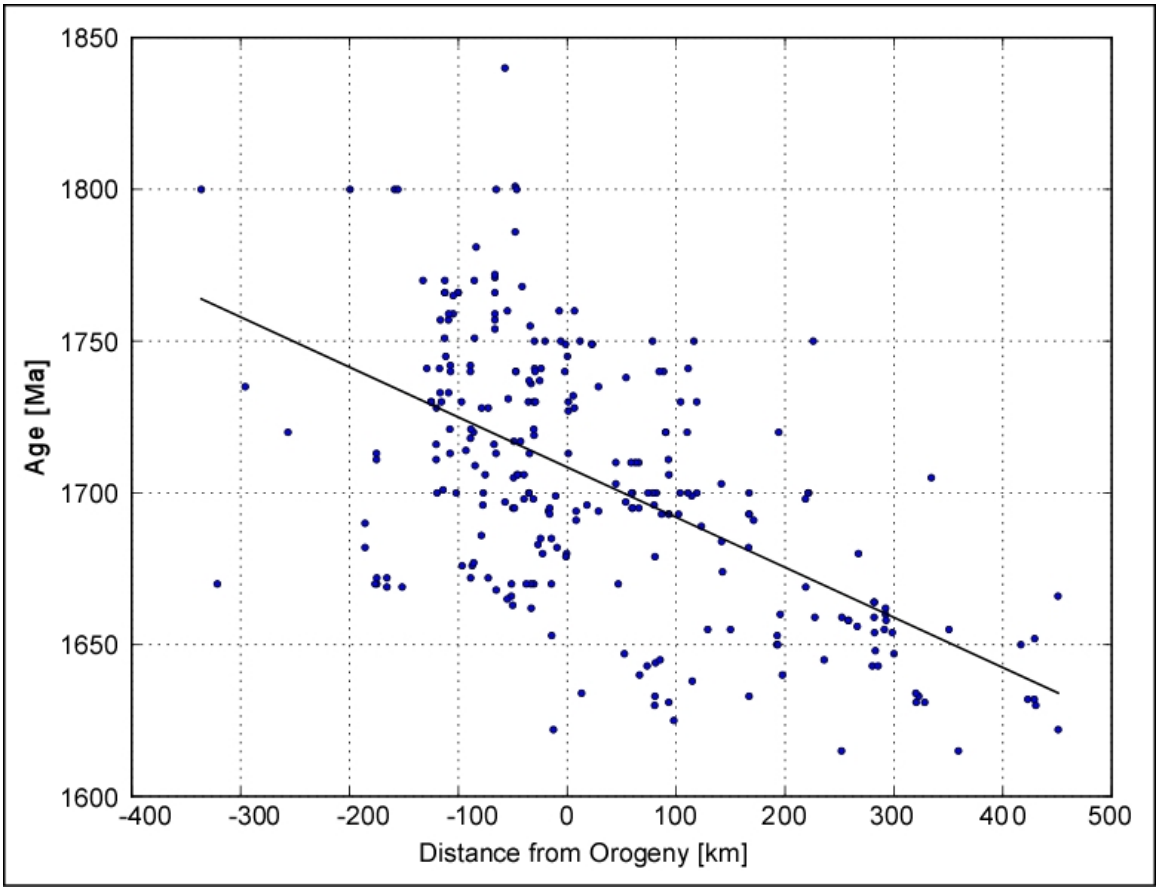

Figure 4-5: A scatter plot showing age [Ma] on the y-axis and distance from the PO [km] on the x-axis for plutons of ages over 1600 Ma. Shown dashed in black is the linear regression of the data set, with a slope of -0.17 Ma/km and an intercept of 1708 Ma. Negative distances are to the north and west, and positive distances to the south and east.

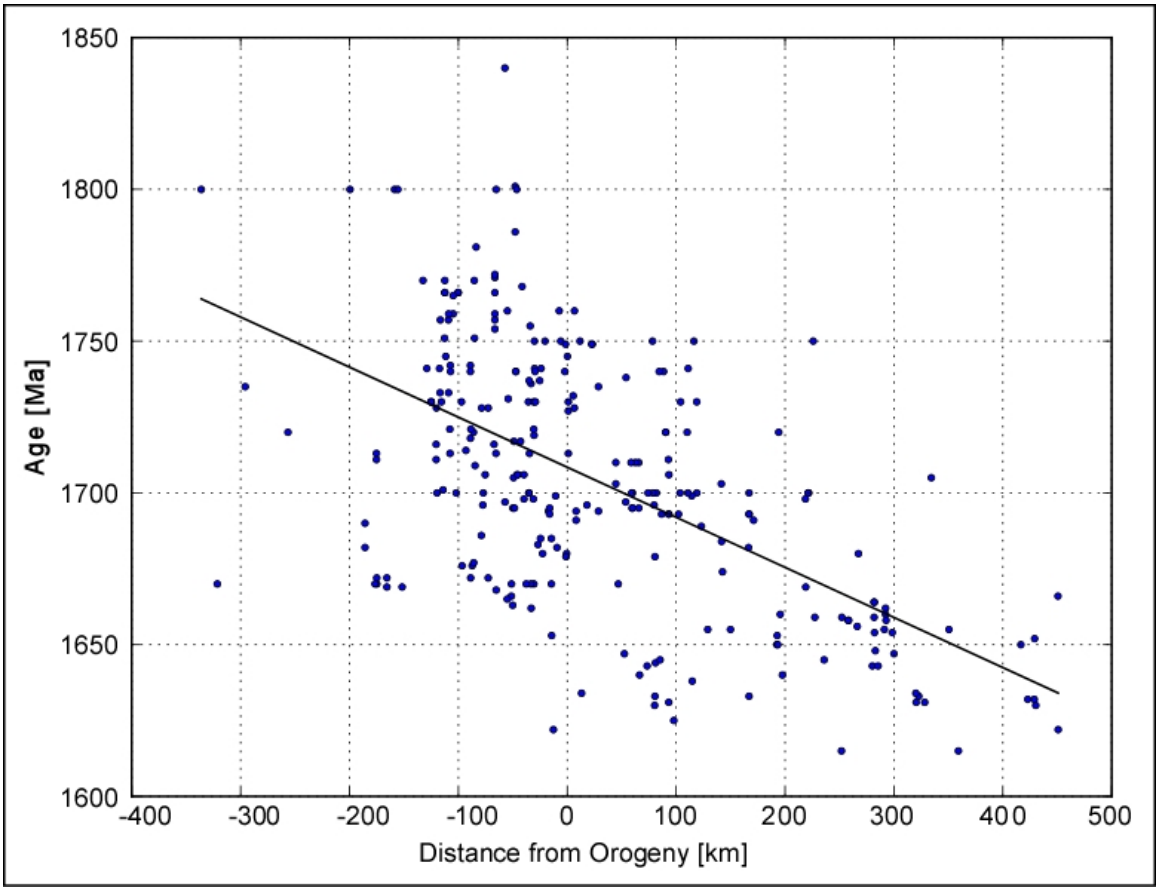

Figure 4-6: A scatter plot showing age [Ma] on the y-axis and distance from the PO [km] on the x-axis for plutons of ages over 1600 Ma. Shown dashed in black is the linear regression of the data set, with a slope of -0.17 Ma/km and an intercept of 1708 Ma. Negative distances are to the north and west, and positive distances to the south and east.

In order to test whether or not two distinct trends are present within the dataset, we divided the data into two groups: one to the northwest of the potential break in the regression line, which will be called population 1 throughout the remainder of the paper, and one to the southeast of the regression line, which will be called population 2 throughout the remainder of the paper. In map view, population one corresponds to all ages that are to the northwest of the PO, whereas population 2 corresponds to all samples that are to the south east of the PO. We then evaluated the statistical significance of the two resulting populations. Without knowing the exact location of the break in the regression, we analyzed a range of possible values to locate the boundary between the two populations. The cutoff within the dataset of coupled ages and distances from the PO was shifted in increments of 5 km between -20 and 20 km (Figure 4-7; Table 1). Linear regressions were then run on the resulting pairs of populations. The slopes, intercepts, p-values and standard errors for these regressions are shown in Table 1. P-values for the slopes and intercepts of population 2 indicate that this trend is significant regardless of the location of the cutoff. In contrast, P-values for the slopes of population 1 never reach significance, while the P-value for the intercept is significant regardless of the cutoff location. This unconstrained slope is due to the increasingly large spread in age versus distance to the northwest. However, we suggest that these are in fact two distinct trends if a cutoff of 15 km is chosen for several reasons. First, the slopes of the two populations are not within error. Second, the P-values drop precipitously at a cutoff distance of -5 km. Third, the intercepts of the two populations are statistically unique. Finally, these observations corroborate a visual assessment of the location of the break between populations. Based on these assertions, we identify an approximate cutoff location

between the two populations at 15 km. Dividing the dataset of ages and distances from the PO into two populations at the cutoff distance of 15 km, population 1 has a slope of -0.09+/-0.05 Ma/km and a y-intercept of 1716+/-5 Ma, whereas population 2 has a slope of -0.17+/-0.02 Ma/km and a y-intercept of 1706+/-5 Ma (Figure 4-8).

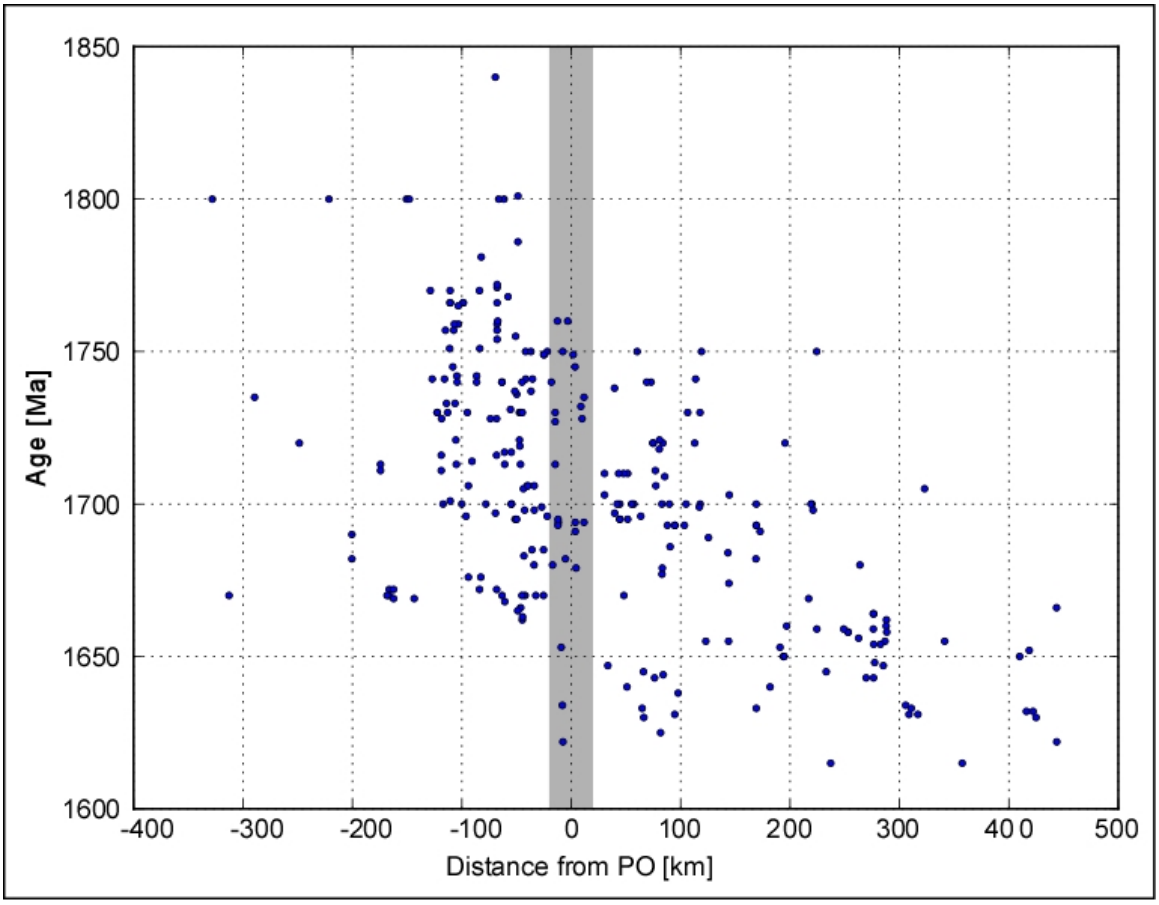

Figure 4-7: A scatter plot showing age [Ma] on the y-axis and distance from the PO [km] on the x-axis for plutons of ages over 1600 Ma. The gray box represents the region of interest across which a potential break in trend was identified.

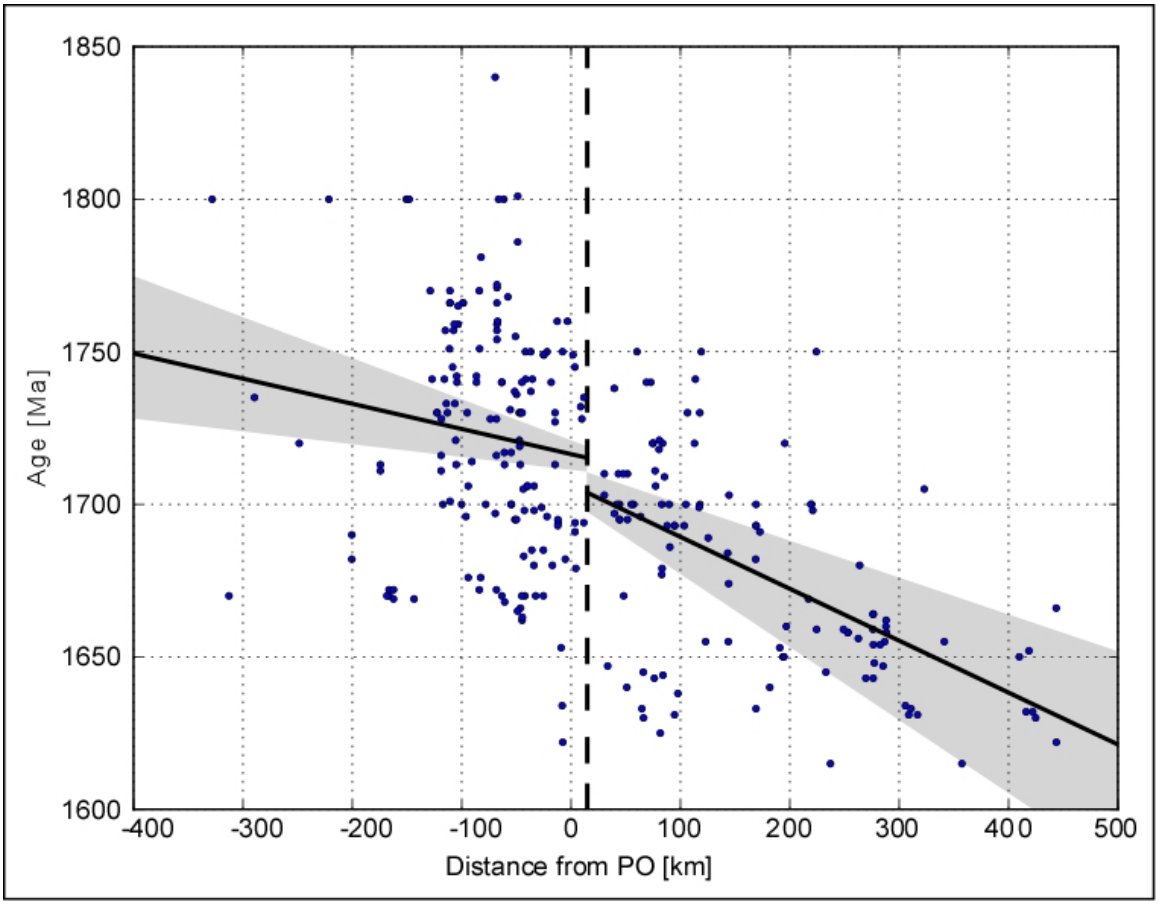

Figure 4-8: A scatter plot showing age [Ma] on the y-axis and distance from the PO [km] on the x-axis for plutons of ages over 1600 Ma. The dashed black line marks the break in plutonism at 15 km. The solid black lines represent the linear regressions for pluton populations one , at distances less than 15 km, and two, at distances greater than 15 km from the orogeny. The slope for the regression of population one is -0.09+/-0.05 Ma/km and the intercept is 1716+/-5 km. The shaded gray regions correspond to the envelope of error on each regression.

Younger Plutons

Looking at the younger dataset, it is clear that there are clusters of ages divided by a ~25 Ma gap in age, with plutons between 1400 and 1500 Ma trending younger to the southeast, and plutons younger than 1400 Ma showing a large spread in age (Figure 4-9). This time period corresponds to the Picuris Orogeny, as constrained by Monazite, Lu/Hf garnet and detrital zircon geochronology (Daniel and Pyle, 2006; Aronoff et al., 2012; Jones et al., 2011; Doe et al., 2012; Daniel et al., in press). Furthermore, plutons of this age are largely of A-type chemistry (e.g. Anderson, 1983). Spatially, plutons of ages between 1400 and 1500 Ma have a slope of 0.05 Ma/km and an intercept of 1434 Ma when plotted against their distance from the PO. This trend has a PCC of 0.47 and a PCCp of $2.6x10^{-5,}$ implying a moderately strong, statistically significant correlation between distance from the PO and age of the pluton.

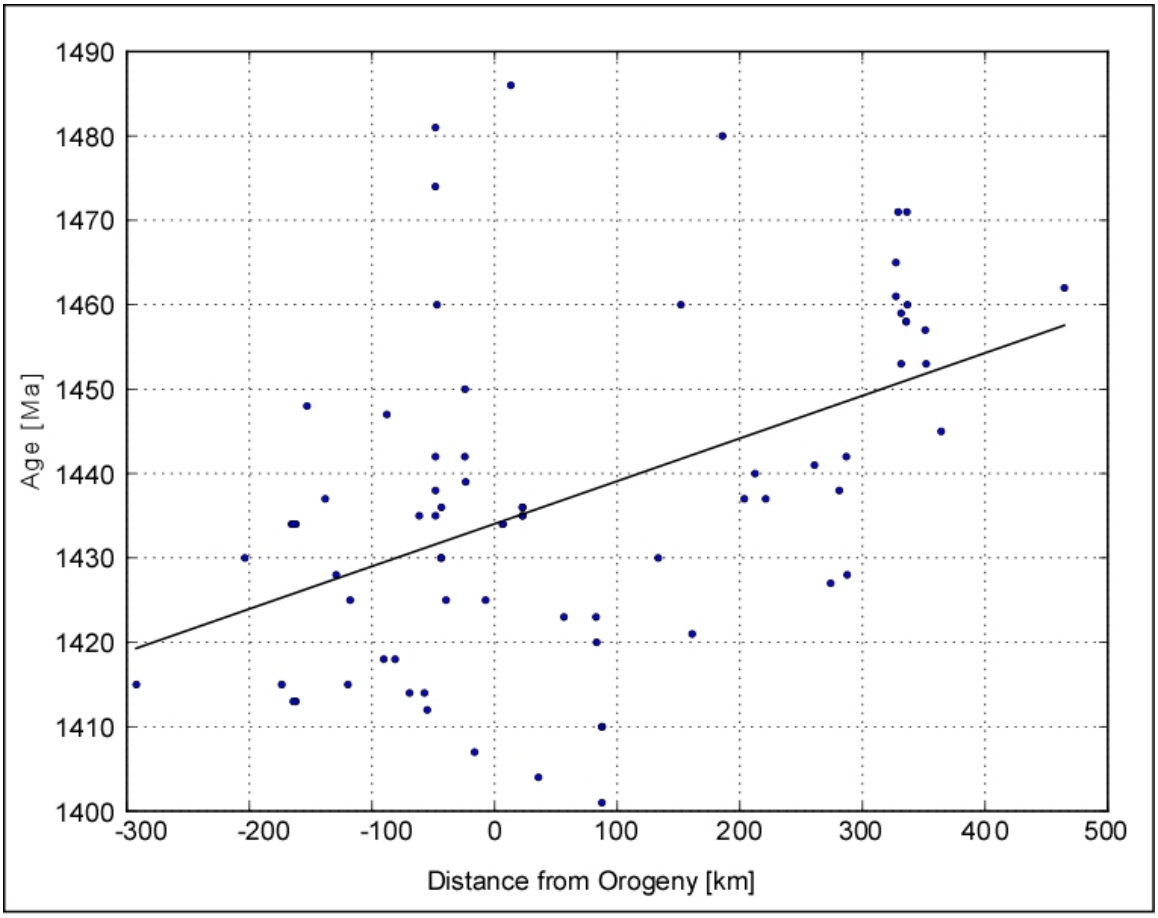

Figure 4-9: A scatter plot showing age [Ma] on the y-axis and distance from the PO [km] on the x-axis for 78 264 plutons of ages between 1400 and 1500 Ma. Shown dashed in black is the linear regression of the data set, with a slope of 0.05 Ma/km and an intercept of 1434 Ma.

Discussion

Spatial Trends

By plotting igneous U/Pb zircon crystallization ages against their distance from a reference line, we can determine the rate at which magmatism progressed toward or away from that line. In the case populations 1 and 2 of the U/Pb ages over 1600 Ma, the slopes determined by linear regression correspond to rates of motion of 11 km/Ma and 6 km/Ma respectively. The lack of statistical significance for the slope of population one underscores the observation that plutonism to the northwest becomes more spatially diffuse. For this reason, we do not make any assertions explicitly relying on the change in trajectory of these trends across the PO. However, in aggregate, these rates correspond to a movement of ~6-11 cm/year, broadly consistent with arc migration, and possibly associated slab rollback (e.g. Copley *et al.*, 2010; Sobel *et al.*, 2013). Here, it is important to note that the width of this volcanic arc cannot be estimated by measuring how far apart igneous bodies of any given age are on the plots of age and distance herein (e.g. Figure 4-6). The PO does not perfectly reflect the geometry of the orogeny, and thus by projecting all of the ages and corresponding distances onto a single axis, all errors in the geometry are integrated into the figure, giving the appearance of an impossibly wide arc.

Although the change in slope between the two trends cannot be proven statistically, the difference between the two intercepts is statistically more robust. This break in volcanism is 15 km southeast of the PO line and corresponds to a discontinuity of ~9 Ma in the migration of the continental arc along the southern margin of Laurentia. This break in volcanism roughly coincides with the location of the orogeny as initially

identified by the spatial extent of 1.4 Ga basins and 1.4 Ga metamorphism (Figure 4-3). Furthermore, this discontinuity defined by the break in volcanism can readily be explained as a localized shortening along the margin of the orogenic belt. Assuming horizontal shortening and that this shortening remains largely un-tilted by subsequent events, the break in volcanism corresponds to a localized crustal shortening of ~54-99 km based on the slopes of the trend lines. The assumptions stated in the previous sentence are supported by the vertical orientation of deformation fabrics reported in locations such as the Picuris and Tusas Mountains (e.g. Grambling, 1979; Williams, 1990; Williams et al., 1999; Daniel and Pyle, 2006; Aronoff et al., 2012). These fabrics have been constrained by cross-cutting relationships and Lu/Hf geochronology to be associated with ~1.4 Ga tectonism (e.g. Aronoff et al., 2012; Hunter et al., 2012).

In contrast with the trends observed in the dataset of older plutons, there is no observable discontinuity in the spatial distribution of plutons between of ages between 1400 and 1500 Ma. Based on their U/Pb concordia zircon crystallization ages and Lu/Hf garnet geochronology ages (Aronoff et al., 2012), these plutons were being emplaced contemporaneously with the amphibolite facies metamorphism that was used to identify the Picuris Orogeny. The spatial trend in these ages was moderately strong, as shown by the Pearson coefficient of 0.45, and corresponds to a rate of progressive northwest directed motion of ~20 km/Ma. The contemporaneous nature of this igneous and orogenic activity suggests an intimate link between the plutonism and orogeny in this case.

Evaluating the Pluton – Orogeny Relationship

In explaining this link between the Picuris Orogeny and A-type pluton ages, two observations must be explained. First, these plutons are primarily A-type in composition and are not traditionally thought to be associated with mountain building. Second, in aggregate, the slope of the trend of this dataset is within error of zero Ma/km.

The A-type composition of many ~1.4 Ga plutons in the region is well documented (e.g. Loiselle and Wones, 1979; Anderson, 1983; Anderson and Bender 1989; Eby, 1990; Gonzales, 1997; Smith et al., 1999; Goodenough et al., 2000; Dall'Agnol and Oliveira, 2007); however, a consensus on their origin remains elusive. Such melts are high in Fe/(Fe+Mg), high in total K as well as K/(K/Na), and are also high in incompatible trace elements and low in trace elements compatible with feldspars and mafic silicates (Frost and Frost, 2011). Geochemical models of melt production aiming to explain such chemical characteristics have shown that such compositions cannot simply be achieved by partial melting of the mantle (e.g. Loiselle and Wones, 1979; Collins et al., 1982; Anderson, 1983; Creaser et al., 1991; Skjerlie and Johnston, 1993; Frost and Frost, 1997).

Ultimately, the goal is to understand what tectonic processes drove the production of these plutons. From the new observations presented herein, as well as the recent identification of the Picuris Orogeny, we can contribute several additional pieces of information toward this goal. First, the model proposed by Vigneressee (2005) is contradicted by two observations. In the model proposed by Vigneressee (2005), the addition of heat to the lower crust requires that this metamorphism occurred at ~1700 Ma, followed by 300 Ma residence at midcrustal levels. The first observation that

contradicts this model is that the sediments in basins associated with the PO received sedimentary input as late as 1460 Ma and subsequently experienced rapid burial and metamorphism. Second, the finding that metamorphism in the region occurred between 1456 and 1399 Ma (Aronoff et al., 2012) requires that these rocks did not experience temperatures the metamorphic conditions for garnet growth until 1456 Ma.

Second, the slope of the trend reported above in this dataset is slightly negative and within error of zero. This suggests either a rapid northwest-ward progression of plutonism or contemporaneous plutonism across the area of interest. This contemporaneous plutonism producing A-type plutonic compositions requires a significant heat input to produce melt from the lower crust can be acquired by over thickened crust experiencing thermal relaxation (e.g. Thompson, 1999), a conclusion supported by the rapid burial and metamorphism of ~1.4 Ga basins associated with the PO.

Summary and Conclusions

Examination of plutonism across the southwest United States with the newly developed tectonic context of the Picuris Orogeny lends insight into multiple facets of the tectonic history of Proterozoic North America. Here, we identify an approximate regional extent and orientation for the Picuris Orogeny using a combination of multiple previously published geochronologic studies. We then use this line as a datum to evaluate spatial trends in the age of Proterozoic plutons. From this exercise, there are several prominent results. First, plutonic ages, divided into two datasets by a gap in age between 1500 and 1600 Ma, show trends relating age to distance from the orogeny. In the older dataset,

plutons increase in age to the northwest, while in the younger dataset, plutons decrease in age to the northwest. Further analysis of the older dataset suggests a break in the trend at 15 km southeast from the line of the Picuris Orogeny.

From these results, we make several conclusions. First, the distribution of plutons in the older dataset preserves evidence for arc migration during the accretion of the Mazatzal terrane at a rate of 5-10 cm/year and further suggests that this arc migration is broadly consistent with rates associated with slab rollback. Second, a break in the trend observed in this older dataset occurs at 15 km southwest of the estimated northern most extent of the Picuris Orogeny. This break in the trend is interpreted as localized shortening of crust within the orogeny. However, the shallow slope of this trend is within error of zero, implying that this episode of plutonism occurred relatively rapidly across the entire region. This observation, combined with recent geochronologic evidence disproving any long-lived midcrustal residence for this crustal material helps to further the debate over the origins of these chemically unique plutons. Here, we suggest that active tectonism, over thickening of the crust and thermal relaxation is a viable mechanism by which the heat and subsequent melting of the lower crust could be produced, ultimately leading to the emplacement of these enigmatic A-type plutons.

References

Aleinikoff, J.N., Reed, J.C., Jr., DeWitt, E., 1993. The Mount Evans batholith in the Colorado Front Range: Revision of its age and reinterpretation of its structure. Geological Society of America Bulletin 105 (6), 791–806.

Amato, J.M., Heizler, M.T., Boullion, A.O., Sanders, A.E., Toro, J., McLemore, V.T., Andronicos, C.L., 2011. Syntectonic 1.46 Ga magmatism and rapid cooling of a gneiss dome in the southern Mazatzal Province: Burro Mountains, New Mexico. Geological Society of America Bulletin 123 (9), 1720–1744.

Anderson, J.L., 1983. Proterozoic inorganic granite plutonism of North America. Geological Society of America Memoir 161, 133-154.

Anderson, J. L., Bender, E. E., 1989. Nature and origin of Proterozoic A-type granitic magmatism in the southwestern United States of America. Lithosphere 23, 19–52.

Anderson, C.A., Silver, L.T., 1976. Yavapai Series, a greenstone belt. Arizona Geological Society Digest 10, 13–26.

Aronoff, R.F., Vervoort, J.D., Andronicos, C.L., Hunter, R.A., 2012. Lu-Hf garnet geochronology and microstructural analysis constrain the timing of crustal assembly in southwestern North America. Geological Society of America Abstracts with Programs 44 (7), 525.

Barnes, M.A., Anthony, E.Y., Williams, I., Asquith, G.B., 2002. Architecture of a 1.38-1.34 Ga granite-rhyolite complex as revealed by geochronology and isotopic and elemental geochemistry of subsurface samples from west Texas, USA. Precambrian Research 119, 9–43.

Bauer, P.W., Karlstrom, K.E., Bowring, S.A., Smith, A.G., Goodwin, L.B., 1993. Proterozoic plutonism and regional deformation - new constraints from the southern Manzano Mountains, central New Mexico. New Mexico Geology 15 (3), 49–56.

Bell, D. A., 1985. Structural and age relationships in the Embudo granites, Picuris Mountains, New Mexico: M.S. Thesis, Dallas, University of Texas, 175.

Bennett, V.C., DePaolo, D.J., 1987. Proterozoic crustal history of the western United States as determined by neodymium isotopic mapping. Geological Society of America Bulletin 99, 647–685.

Bickford, M. E., Cullers, R. L., Shuster, R. D., Premo, W. R., Van Schmus, W. R., 1989a. U-Pb zircon geochronology of Proterozoic and Cambrian plutons in the Wet Mountains and southern Front Range, Colorado, Proterozoic geology of the southern Rocky Mountains. Geological Society of America, Special Paper 235, 33–48.

Bickford, M. E., Shuster, R. D., Boardman, S. J., 1989b. U-Pb geochronology of the Proterozoic volcano-plutonic terrane in the Gunnison and Salida area, Colorado, Proterozoic geology of the southern Rocky Mountains. Geological Society of America, Special Paper 235, 33–48.

Bickford, M. E., Soegaard, K., Nielsen, K. C., McLelland, J. M., 2000. Geology and geochronology of Grenville-age rocks in the Van Horn and Franklin Mountains area, west Texas: Implications for the tectonic evolution of Laurentia during the Grenville. Geological Society of America Bulletin 112, 1134–1148.

Bickford, M.E., Boardman, S.J., 1984. A Proterozoic volcano-plutonic terrane, Gunnison and Salida areas, Colorado. The Journal of Geology 92 (6), 657–666.

Bickford, M.E., Mueller, P.A., Kamenov, G.D., Hill, B.M., 2008. Crustal evolution of southern Laurentia during the Paleoproterozoic: Insights from zircon Hf isotopic studies of ca. 1.75 Ga rocks in central Colorado. Geology 36, 555–558.

Blacet, P.M., Silver, L.T., Stern, T.W., Anderson, C.A., 1971. Precambrian evolution of the Big Bug Group (Yavapai Series) and associated rocks in the northern Bradshaw Mountains, central Arizona. Geological Society of America Abstracts with Programs 3, 84.

Bowring, S. A. Condie, K. C., 1982. U-Pb zircon ages from northern and central New Mexico. Geological Society of America, Abstracts with Programs 8, 304.

Bowring, S. A., Housh, T. B., Van Schmus, W. R., Podosek, F. A., 1992. A major Nd isotopic boundary along the southern margin of Laurentia. EOS Transactions of the American Geophysical Union 73 (14), 333.

Bowring, S. A., Kent, S. C., Sumner, W., 1983. Geology and U-Pb geochronology of Proterozoic rocks in the vicinity of Socorro, New Mexico. New Mexico Geological Society, 34th Field Conference, Guidebook 1, 37–142.

Bowring, S. A., Reed, J. C., Jr., Condie, K. C., 1984. U-Pb geochronology of Proterozoic volcanic and plutonic rocks, Sangre de Cristo Mountains, New Mexico. Geological Society of America Abstracts with Programs 16 (4), 216.

Bowring, S., Karlstrom, K.E., Chamberlain, K., 1986. U-Pb zircon constraints on Proterozoic tectonic evolution in central Arizona. Geologic Society of America Abstracts with Programs 16, 343.

Bryant, B., Wooden, J.L., 1986. Early and middle Proterozoic crustal history of the Poachie Range, Arizona. Geological Society of America Abstracts with Programs 18, 344

Bryant, B., Wooden, J.L., Nealey, L.D., 2001. Geology, geochronology, geochemistry and Pb-isotopic compositions of Proterozoic rocks, Poachie region, west-central Arizona - A study of the east boundary of the Proterozoic Mojave crustal province. USGS Professional Paper 1639, 54.

Buda, A., Jarynowski, A., 2010. Life-time of correlations and its applications. Andrzej Buda, Wydawnictwo Niezależne.

Chamberlain, K.R., Bowring, S.A., 1990. Proterozoic geochronologic and isotopic boundary in NW Arizona. The Journal of Geology 98 (3), 399–416.

Clemens, J.D., Holloway, J.R., White, A.J.R., 1986. Origin of an A-type granite: experimental constraints. Am. Mineral. 71, 317–324.

Copley, A., Avouac, J.-P., Royer, J.-Y., 2010. India-Asia collision and the Cenozoic slowdown of the Indian plate: implications for the forces driving plate motions. Journal of Geophysical Research, 115.

Collins, W.J., Beams, D., White, J.R., Chappell, B.W., 1982. Nature and origin of A-type granites with particular reference to south-eastern Australia. Contributions to Mineralogy and Petrology 80, 189 – 200.

Condie, K. C., Latysh, N., Van Schmus, W. R., Kozuch, M., and Selverstone, J., 1999. Geochemistry, Nd and Sr isotopes, and U/Pb zircon ages of granitoid and metasedimentary xenoliths from the Navajo Volcanic Field, Four Corners area, southwestern United States. Chemical Geology 156, 95–133.

Conway, C.M., 1976. Petrology, Structure and evolution of a Precambrian volcanic and plutonic complex, Tonto Basin, Gila County, Arizona: PhD Thesis, California Institute of Technology, 920.

Copeland, P., Bowring, S. A., 1988. U-Pb and Ar-Ar ages from Proterozoic rocks, west Texas. Geological Society of America Abstracts with Programs 20 (2), 95–96.

Creaser, R. A., Price, R. C., Wormald, R. J., 1991. A-type granites revisited: assessment of a residual-source model. Geology 19, 163 – 166.

Dall'Agnol, R., Oliveira, D.C., 2007. Oxidized, magnetite-series, rapakivi-type granites of Carajás, Brazil: implications for classification and petrogenesis of A-type granites. Lithosphere 93, 215 – 233.

Daniel, C.G., Pyle, J, 2006. Monazite-Xenotime Thermochronometry and Al_2SiO_5 Reaction Textures in the Picuris Range, Northern New Mexico, USA: New Evidence for a 1450-1400 Ma Orogenic Event. Journal of Petrology 47, 97–118.

Daniel, C.G., Pfeifer, L.S., Jones, J., McFarlane, C., in press. Detrital zircon evidence for non-Laurentian provenance, Mesoproterozoic (ca. 1490–1450 Ma) deposition and

orogenesis in a reconstructed orogenic belt, northern New Mexico, USA: defining the Picuris Orogeny. Geological Society of America Bulletin.

Davis, B., Williams, M. L., Bowring, S. A., and Ramezani, J., 2001. Implications of new age constraints on the structural and petrologic evolution of middle Proterozoic rocks in the central Tusas Mountains of northern New Mexico, Geological Society of America Abstracts with Programs 33 (5), A11.

Davis, P., Williams, M., Karlstrom, K., 2011. Structural evolution and timing of deformation along the Proterozoic Spring Creek shear zone of the northern Tusas Mountains, New Mexico. New Mexico Geological Society Guidebook 62, 177–190.

DePaolo, 1981. Neodymium isotopes in the Colorado Front Range and crust-mantle evolution in the Proterozoic. Nature 291, 193-196.

DePaolo, D.J., Linn, A.M., Schubert, G., 1991. The Continental Crustal Age Distribution: Methods of Determining Mantle Separation Ages from Sm-Nd Isotopic Data and Application to the Southwestern United States. Journal of Geohpysical Research 96, B2, 2071–2088.

Doe, M.F., Jones, J.V. III, Karlstrom, K.E., Thrane, K., Frei, D., Gehrels, G., and Pecha, M., 2012. Basin formation near the end of the 1.60–1.45 Ga tectonic gap in southern Laurentia: Mesoproterozoic Hess Canyon Group of Arizona and implications for ca. 1.5 Ga supercontinent configurations. Lithosphere 4, 77–88

Duebendorfer, E.M., Christensen, C., 1995. Synkinematic (?) intrusion of the "anorogenic" 1425 Ma Beer Bottle Pass pluton, southern Nevada. Tectonics 14, 168–184.

Duebendorfer, E.M., Chamberlain, K.R., Jones, C.S., 2001. Paleoproterozoic tectonic history of the Cerbat Mountains, northwestern Arizona: Implications for crustal assembly in the southwestern United States. Geological Society of America Bulletin 113 (5), 575 – 590.

Duchesne, J.C., Li´egeois, J.P., Vander Auwera, J., Longhi, J., 1999. The crustal tongue melting model and the origin of massive anorthosites. Terra Nova 11, 100 – 105.

Eby, G. N., 1990. The A-type granitoids: A review of their occurrence and chemical characteristics and speculations on their petrogenesis. Lithosphere 26, 115 – 134.

Eisele, J., Isachsen, C.E., 2001. Crustal Growth in Southern Arizona: U-Pb geochronologic and Sm-Nd isotopic evidence for addition of the Paleoproterozoic Cochise Block to the Mazatzal Province. American Journal of Science 301, 773–797.

Ferguson, C.B., Duebendorfer, E.M., Chamberlain, K.R., 2004. Synkinematic Intrusion of the 1.4-Ga Boriana Canyon Pluton, Northwestern Arizona: Implications for Ca. 1.4-Ga Regional Strain in the Western United States. The Journal of Geology 112, 165–183. Journal of Petrology 52, 39 – 53.

Foley, S.F., Venturelli, G., Green, D.H., Toscani, L., 1987. The ultrapotassic rocks: characteristics, classification and constraints for petrogenetic models. Earth Sci. Rev. 24, 81–134.

Frost, C.D., Frost, B.R., 1997. Reduced rapakivi-type granites: the tholeiite connection. Geology 25, 647–650.

Frost, C.D., Frost, B.R., 2011. On Ferroan (A-type) Granitoids: their Compositional Variability and Modes of Origin. Journal of Petrology 52, 39 – 53.

Fulp, M. S., 1982. Precambrian geology and mineralization of the Dalton Canyon volcanic center, Santa Fe County, New Mexico: M.S. Thesis, University of New Mexico, 199.

Gonzales, D.A., 1997. Crustal evolution of the Needle Mountains Proterozoic complex, Southwestern Colorado. Doctoral Dissertation. University of Kansas, Lawrence, Kansas, p. 190.

Gonzales, D.A., VanSchmus, W.R., 2007. Proterozoic history and crustal evolution in southwestern Colorado: Insight from U/Pb and Sm/Nd data. Precambrian Research 154, 31–70.

Goodenough, K.M., Upton, B.G.J., Ellam, R.M., 2000. Geochemical evolution of the Ivgtut granite, South Greenland: a fluorine-rich ‘A-type’ intrusion. Lithosphere 51, 205 – 221.

Grambling, J. A., 1979. Precambrian geology of the Truchas Peaks region, north-central New Mexico, and some regional implications. New Mexico Geological Society Guidebook, 30th Field Conference, 135–143.

Grambling, J.A., 1981. Prerssures and temperatures in Precambrian metamorphic rocks. Earth and Planetary Science Letters 53, 63 – 68.

Grambling, J. A., Dallmeyer, R. D., 1993. Tectonic evolution of Proterozoic rocks in the Cimarron Mountains, northern New Mexico, USA. Journal of Metamorphic Geology 11, 739–755.

Hawkins, D.P., Bowring, S.A., Ilg, B.R., Karlstrom, K.E., Williams, M.L., 1996. U-Pb geochronologic constraints on the Paleoproterozoic crustal evolution of the Upper Granite Gorge, Grand Canyon, Arizona. Geological Society of America Bulletin 108 (9), 1167–1181.

Hawkins, D.P., Bowring, S.A., 1997. U-Pb systematics of monazite and xenotime: case studies from the Paleoproterozoic of the Grand Canyon, Arizona. Contributions to Mineralogy and Petrology 127, 87–103.

Hoffman, P.F., 1989. Precambrian geology and tectonic history of North America. *In*: Bally, A.W., and Palmer, A.R. (Eds.), The geology of North America–An overview: Boulder, Colorado, Geological Society of America, 447–512.

Hunter, R.A., Andronicos, C.L., Vervoort, J.D., Aronoff, R.F., 2012. Refining the Proterozoic history of North America through combined use of Lu-Hf geochronology and Petrologic Analysis. Geological Society of America Abstracts with Programs 44 (7), 526.

Isachsen, C.E., Gehrels, G.E., Riggs, N.R., Spencer, J.E., Ferguson, C.A., Skotnicki, S.J., Richard, S.M., 1999. U-Pb Geochronologic Data from Zircons from Eleven Granitic Rocks in Central and Western Arizona. Arizona Geological Survey Open-File Report 99-5, 30.

Jessup, M.J., Karlstrom, K.E., Connelly, J.N., Williams, M.L., Livaccari, R., Tyson, A., Rogers, S.A., 2005. Complex Proterozoic crustal assembly of southwestern North America in an arcuate subduction system: The Black Canyon of the Gunnison, southwestern Colorado. *In*: Karlstrom, K.E., Keller, G.R. (Eds.), The Rocky Mountain Region: An Evolving LithosphereTectonics, Geochemistry and Geophysics, American Geophysical Union monograph 154, 21–38.

Jessup, M.J., Jones, J.V.III, Karlstrom, K.E., Williams, M.L., Connelly, J.N., Heizler, M.T., 2006. Three Proterozoic Orogenic Episodes and an Intervening Exhumation

Event in the Black Canyon of the Gunnison Region, Colorado. The Journal of Geology 114, 555–576.

Jones, J.V. III, 2005. Proterozoic tectonic evolution of southern Laurentia: New constraints from field studies and geochronology in southern Colorado and northern New Mexico, U.S.A.: Ph.D. thesis, Austin, University of Texas, 204.

Jones, J.V., Connelly, J.N., Karlstrom, K.E., Williams, M.L., Doe, M.F., 2009. Age, provenance, and tectonic setting of Paleoproterozoic quartzite successions in the southwestern United States. Geological Society of America Bulletin 121, 247–264.

Jones, J.V.III, Rogers, S.A., Connelly, J.N., 2010a. U-Pb geochronology of Proterozoic granites in the Sawatch Range central Colorado, U.S.A.. Rocky Mountain Geology 45 (1), 1–22.

Jones. J.V. III, Siddoway, C.S., Connelly, J.N., 2010b. Characteristics and implications of ca. 1.4 Ga deformation across a Proterozoic mid-crustal section, Wet Mountains, Colorado, USA. Lithosphere 2, 119–135.

Jones, J.V. III, Daniel, C.G., Frei, D., Thrain, K., 2011. Revised regional correlations and tectonic implications of Paleoproterozoic and Mesoproterozoic metasedimentary rocks in northern New Mexico, USA: New Findings from detrital zircon studies of the Hondo Group, Vadito Group, and Marqueñas Formation. Geosphere 7 (4), 974–991

Karlstrom, K.E., Bowring, S.A., Conway, C.M., 1987. Tectonic significance of an Early Proterozoic two-province boundary in central Arizona. Geological Society of America Bulletin 99, 529–538.

Karlstrom, K.E., Bowring, S.A., 1993. Proterozoic orogenic history of Arizona, *in* Van Schmus, W.R., Bickford, M.E., and 23 others, Transcontinental Proterozoic provinces. *In* Reed, J.C., Jr., and 6 others (Eds.), Precambrian: Conterminous U.S.: Boulder Colorado, Geological Society of America, The Geology of North America C-2, 188-211.

Karlstrom, K.E., and Daniel, C.G., 1993. Restoration of Laramide right-lateral strike slip in northern New Mexico by using Proterozoic piercing points; tectonic implications from the Proterozoic to the Cenozoic. Geology 21, 1139–1142.

Karlstrom, K.E., Williams, M.L., 1996. Looping *P-T* paths and high-*T*, low-*P* middle crustal metamorphism: Proterozoic evolution of the southwestern United States. Geology 24, 1119–1122.

Karlstrom, K.E., Amato, J.M., Williams, M.L., Heizler, M., Shaw, C., Read, A., Bauer, J., 2004. Proterozoic tectonic evolution of the New Mexico region: A synthesis. *In*: Mack, G. H., and Giles, K. A. (Eds.), The Geology of New Mexico: A Geologic History: New Mexico Geological Society Special Publication 11, 11–34.

Keller, G.R., Hills, J.M., Baker, M.R., Wallin, E.T, 1989. Geophysical and geochronological constraints on the extent and age of mafic intrusions in the basement of West Texas and eastern New Mexico. Geology 17, 1049–1052.

Kirby, E., Karlstrom, K.E., Andronicus, C., 1995. Tectonic setting of the Sandia pluton: an orogenic 1.4 Ga granite in New Mexico. Tectonics 14, 185–201.

Landenberger, B., Collins,W.J., 1996. Derivation of A-type granites from a dehydrated charnockitic lower crust: evidence from the Chaelundi complex, eastern Australia. J. Petrol. 37, 145–170.

Leader, J.W., Jones, J.V.III, 2008. Age and tectonic significance of the ca. 1.4 Ga Brown Pass pluton, Collegiate Peaks Wilderness Area, Colorado. Geological Society of American Abstracts with Programs 40 (1), 69

Li, Y., Barnes, M.A., Barnes, C.G., Frost, C.D., 2007. Grenville-age A-type and related magmatism in southern Laurentia, Texas and New Mexico, U.S.A.. Lithosphere 97, 58–87.

Lipman, W. Reed, J.C., Jr., 1989. Geologic map of the Latir volcanic field and adjacent areas, northern New Mexico, U.S. Geological Survey, Map 1-1907, scale l :48,000.

Loiselle, M.C., Wones, D., 1979. Characteristics and origin of anorogenic granites. Geological Society of America, Abstracts with Programs 11, 468.

Lonsdale, P., Klitgord, K.D., 1978. Structure and tectonic history of the eastern Panama Basin. Geological Society of America Bulletin 89 (7), 981–999.

Ludwig, K., 1974. Precambrian geology of the central Mazatzal Mountains, Arizona, PhD Thesis, California Institute of Technology, 363.

Magnani, M.B., Miller, K.C., Levander, A., Karlstrom, K., 2004. The Yavapai-Mazatzal boundary: A long-lived tectonic element in the lithosphere of southwestern North America. Geological Society of America Bulletin 116 (9-10), 1137–1142.

Nelson, B.K., DePaolo, D.J., 1985. Rapid production of continental crust 1.7 to 1.9 b.y. ago: Nd isotopic evidence from the basement of the North American mid-continent. Geological Society of America Bulletin 96 (6), 746–754.

Nyman, M.W., Karlstrom, K.E., Kirby, E., Graubard, C.M., 1994. Mesoproterozoic contractional orogeny in western North America: evidence from 1.4 Ga plutons. Geology 22, 901–904.

Nyman, M.W., Karlstrom, K.E., 1997. Pluton emplacement processes and tectonic setting of the 1.42 Ga Signal batholith, SW USA: important role of crustal anisotropy during regional shortening. Precambrian Research 82, 237–263.

Pedrick, J.M., Karlstrom, K.E., Bowring, S.A., 1998, Reconciliation of conflicting models for Proterozoic rocks of northern New Mexico. Journal of Metamorphic Geology 16, 687–707.

Pollock, T.R., Goodwin, L.B., Bauer, P.W., Bowring, S. A., 1994. Evidence for the relative timing and character of Proterozoic deformation and metamorphism in the Ladron Mountains, New Mexico. New Mexico Geology 16 (4), 82-83.

Ramo, O.T., McLemore, V.T., Hamilton, M.A., Kosunen, P.J., Heizler, M., Haapala, I., 2003. Intermittent 1630-1220 Ma magmatism in central Mazatzal province: New geochronologic piercing points and some tectonic implications. Geology 31, 335–338.

Read, A., Karlstrom, K. E., Grambling, J.A., Bowring, S. A., Heizler, M., Daniel, C., 1999. A mid-crustal cross section from the Rincon Range, northern New Mexico: Evidence for 1.68 Ga pluton-influenced tectonism and 1.4 Ga regional metamorphism. Rocky Mountain Geology 34 (1), 67–91.

Reed, J.C., Jr., 1984. Proterozoic rocks of the Taos Range, Sangre de Cristo Mountains, New Mexico. New Mexico Geological Society, 35th Field Conference, Guidebook, 179–185.

Reed, J.C. Jr., Bickford, M.E., Premo, W.R., Aleinikoff, J.N., Pallister, J.S., 1987. Evolution of the Early Proterozoic Colorado province: Constraints from U-Pb geochronology. Geology 15, 861–865.

Reese, J.F., Mosher, S., Connelly, J., Robacks, R., 2000. Mesoproterozoic chronostratigraphy of the southeastern Llano uplift, central Texas. Geological Society of America Bulletin 112, 278–291.

Renshaw, J.L., 1984. Precambrian geology of the Thompson Peak area, Sante Fe County, New Mexico: Masters Thesis, University of New Mexico, 197.

Robertson, J.M. and Condie, K.C., 1989. Geology and geochemistry of early Proterozoic volcanic and subvolcanic rocks of the Pecos greenstone belt, Sangre de Cristo Mountains, New Mexico. Geological Society of America Special Paper 235, 119–146.

Rodgers, J.L., Nicewander, W.A., 1988. Thirteen ways to look at the correlation coefficient. The American Statistician 42, 59 – 66.

Roths, P., 1991. Geology of Proterozoic outcrops in Dead Man and Little San Nicholas Canyons, southern San Andres Mountains, New Mexico. New Mexico Geologic Society, 42nd Field Conference, Guidebook, 91–96.

Sabin, T.G., 1994. Geochronology and isotope geochemistry of Early Proterozoic rocks exposed in portions of the Twin Peaks and Blanca Peak quadrangles, Alamosa, Costillo, and Huerfano Counties, Colorado: M.S. thesis, University of Kansas, 94.

Shastri, L. L., 1993. Proterozoic geology of the Los Pinos Mountains, central New Mexico: timing of plutonism, deformation, and metamorphism: M.S. Thesis, University of New Mexico, 82.

Shaw, C.A., Karlstrom, K.E., 1999. The Yavapai- Mazatzal crust boundary in the Southern Rocky Mountains. Rocky Mountain Geology 34 (1), 37–52.

Shaw, C.A., Heizler, M.T., and Karlstrom, K.E., 2005, 40Ar/301234 Ar thermochronologic record of 1.45-1.35 Ga intracontinental tectonism in the southern Rocky Mountains: Interplay of conductive and advective 1236 heating with intracontinental deformation, *in* Karlstrom, K.E. and Keller, G.R., eds., The Rocky Mountain Region: An Evolving Lithosphere. Washington D.C., American Geophysical Union Geophysical Monograph 154, p. 163–184.

Silver, L.T., 1965. Mazatzal orogeny and tectonic episodicity. Geological Society of America Special Paper 82, 185–186.

Silver, L.T., 1967. U-Pb isotope relations in Precambrian zircons from Bagdad, Arizona. Geological Society of America Special Paper 101, 420.

Silver, L.T., Barker, F., 1968. Geochronology of Precambrian rocks of the Needle Mountains, southwestern Colorado. Geological Society of America, Special Paper 115, 204–205.

Silver, L.T., Bickford, M.E., Van Schmus, W.R., Anderson, J.L., Anderson, T.H., Medaris, L.G., Jr., 1977. The 1.4–1.5 b.y. transcontinental anorogenic plutonic perforation of North America. Geological Society of America Abstracts with Programs 9 (7), 1176–1177.

Silver, L.T., 1984. Observations on the Precambrian evolution of northern New Mexico and adjacent regions. Geological Society of America Abstracts with Programs 16, 256.

Silver, L.T., Conway, C.M., Ludwig, K.R., 1986. Implications of a precise chronology for Early Proterozoic crustal evolution and caldera formations in the Tonto Basin-Mazatzal Mountains region, Arizona. Geological Society of America Abstracts with Programs 18, 413.

Skjerlie, K.P., Johnston, A.D., 1993. Fluid-absent melting behavior of an F-rich tonalitic gneiss at mid-crustal pressures: Implications for the generation of anorogenic granites. Journal of Petrology 34, 785 – 815.

Smith, D.R., Noblett, J., Wobus, R.A., Unruh, D., Douglass, J., Beane, R., Davis, C., Goldman, S., Kay, G., Gustavson, B., Saltoun, B., Stewart, J., 1999. Petrology and geochemistry of late-stage intrusions of the A-type, mid-Proterozoic Pikes Peak batholith (Central Colorado, USA): implications for petrogenetic models. Precambrian Research 98, 271 – 305.

Sobel, E.R., Chen, J., Schoenbohm, L.M., Thiede, R., Stockli, D.F., Sudo, M., Strecker, M.R., 2013. Oceanic-style subduction controls late Cenozoic deformation of the Northern Pamir orogen. Earth and Planetary Science Letters 363, 204–218.

Stacey, J.S., Hedlund, D.C., 1983. Lead-isotopic compositions of diverse igneous rocks and ore deposits from southwestern New Mexico and their implications for Early

Proterozoic crustal evolution in the western United States. Geological Society of America Bulletin 94, 43–57.

Stewart, J.H., Gehrels, G.E., Barth, A.P. Link, P.K., Christie-Block, N., Wrucke, C.T., 2001. Detrital zircon provenance of Mesoproterozoic to Cambrian arenites in the western United States and northwestern Mexico. Geological Society of America Bulletin 113 (10), 1343–1356.

Thompson, A.B., 1999. Some time-space relationships for crustal melting and granitic intrusion at various depths. *In* Castro, A., Fernandez, C., Vigneresse, J.L. (Eds.), Understanding Granites: Integrating New and Classical Techniques, vol. 168. Geological Society [London] Special Publication 168, 7–25.

Tikoff, B., Benford, B., and Giorgis, S., 2008. Lithospheric control on the initiation of the Yellowstone hotspot: Chronic reactivation of lithospheric scars. International Geology Review 50, 305-324.

Van Schmus, W.R., and Bickford, M.E., 1981. Proterozoic chronology and evolution of the midcontinent region, North America. *In*: Kröner, A. (Ed.), Precambrian plate tectonics: Amsterdam, Elsevier, Developments in Precambrian Geology, 261–296.

Van Schmus, W.R., Bickford, M.E., Lewry, J.F., Macdonald, R., 1987. U–Pb geochronology of the Trans–Hudson orogen in northern Saskatchewan, Canada. Canadian Journal of Earth Sciences 24, 407–424.

Van Schmus, W.R., Bickford, M.E., Condie, K.C., 1993. Early Proterozoic crustal evolution, *in* Reed, J.C., Jr., and 6 others, eds., Precambrian: Conterminous U.S.: Boulder, Colorado, Geological Society of America, The Geology of North America C-2, 270–281.

Vigneresse, J.L., 2005. The specific case of Mid-Proterozoic rapakivi granites and associated suite within the context of the Columbia supercontinent. Precambrian Research 137 (1-2), 1–34.

Vollbrecht, K.M., 1997. Constraints on the timing and character of Proterozoic deformation and metamorphism in the San Andres Mountains of south-central New Mexico, M.S. thesis, New Mexico Tech, 85.

Williams, M., 1990. Sigmoidal inclusion trails, punctuated fabric development, and interactions between metamorphism and deformation. Journal of Metamorphic Geology 12, 1–21.

Williams, M.L., Karlstrom, K.E., Lanzirotti, A., Read, A.S., Bishop, J.L., Lombardi, C.E., Pedrick, J.N., Wingstead, M.B., 1999. New Mexico middle-crustal cross sections: 1.65-Ga macroscopic geometry, 1.4-Ga thermal structure, and continued problems in understanding crustal evolution. Rocky Mountain Geology 34, 53 – 66.

Woodward, L.A., 1987. Geology and mineral resources of Sierra Nacimiento and vicinity, New Mexico. New Mexico Bureau Mines Mineral Resources Memoir 42, 84.

Tables

					Population 2				
Break Location	-20	-15	-10	-5	0	5	10	15	20
Intercept	1706	1706	1705	1710	1708	1708	1707	1706	1706
Error	3.99	4.01	4.43	4.4	4.42	4.7	4.8	5	5
P	~0	~0	~0	~0	~0	~0	~0	~0	~0
Slope	-0.17	-0.17	-0.16	-0.18	-0.18	-0.17	-0.17	-0.17	-0.17
Error	0.2	0.02	0.02	0.023	0.02	0.02	0.02	0.02	0.02
P	~0	~0	~0	~0	~0	~0	~0	~0	~0
					Population 1				
Intercept	1720	1720	1720	1714	1716	1715	1716	1716	1716
Error	6.3	6.2	5.7	5.6	5.6	5.3	5.2	5	5
P	~0	~0	~0	~0	~0	~0	~0	~0	~0
Slope	-0.05	-0.05	-0.06	-0.1	-0.09	-0.09	-0.09	-0.09	-0.09
Error	0.06	0.06	0.06	0.06	0.06	0.05	0.05	0.05	0.05
P	0.43	0.36	0.31	0.09	0.11	0.09	0.1	0.09	0.09

Table 4-1: A table of the statistical properties of the regressions of populations 1 and two within the older dataset of pluton age and pluton distance from the PO when the break between populations is moved to the break location.

Appendix 1

Ref	Age	Rock Type	Latitude	Longitude
1	1448	Granite	39.57	-105.63
2	1730	Rhyolite	38.56	-107.00
3	1735	Rhyolite	34.88	-114.08
3	1694	Two mica granite	34.88	-114.08
3	1690	Granite	36.97	-114.03
3	1682	Monzogranite	36.97	-114.03
3	1727	Dacite	35.29	-113.63
3	1713	Granite	35.29	-113.63
3	1730	Granodiorite	35.29	-113.63
4	1786	Metavolcanic	37.51	-107.54
4	1801	Metavolcanic	37.51	-107.54
4	1754	Twilight Gneiss	37.62	-107.80
4	1759	Twilight Gneiss	37.62	-107.80
4	1771	Twilight Gneiss	37.62	-107.80
4	1757	Twilight Gneiss	37.62	-107.80
4	1766	Twilight Gneiss	37.62	-107.80
4	1772	Twilight Gneiss	37.62	-107.80
4	1716	Grantie	37.66	-107.68
4	1731	Granite	37.51	-107.79
4	1695	Granite	37.47	-107.80
4	1695	Granite	37.46	-107.79
4	1435	Gabbro	37.58	-107.79
4	1481	Granite	37.50	-107.61
4	1435	Granite	37.50	-107.61
4	1438	Granite	37.50	-107.61
4	1442	Granite	37.50	-107.61
5	1736	Dacite	35.46	-114.13
5	1768	Granite	35.55	-114.10
5	1737	Granite	35.48	-114.13
5	1719	Granite	35.43	-114.14
5	1721	Granite	35.43	-114.14
5	1683	Granite	35.43	-114.03
6	1735	Quartz Diorite	40.50	-106.83
6	1720	Quartz Monzonite	40.50	-106.00
6	1672	Quartz Monzonite	40.00	-105.25
6	1670	Quartz Monzonite	40.00	-105.25
6	1669	Quartz-feldspar Gneiss	39.75	-105.25
6	1700	Rhyolite	35.25	-106.17
6	1750	Granodiorite	35.25	-106.08
6	1669	Unknown	39.00	-107.00
6	1672	Unknown	39.00	-107.00
7	1404	Granite	34.83	-114.00
8	1750	Porphyroclastic gneiss	36.09	-112.04
8	1741	Quartzofeldspathic schist and gneiss	36.05	-111.97
8	1840	Quartz Diorite	36.23	-112.42
8	1741	granodiorite	36.09	-112.04

8	1737	Granite	36.05	-112.00
8	1730	Granodiorite	36.11	-112.15
8	1717	Amphibolite	36.19	-112.31
8	1717	Granodiorite	36.14	-112.26
8	1713	Quartz Diorite	36.10	-112.14
8	1698	Two mica granite	36.09	-112.06
8	1697	Pegmatite	36.24	-112.38
8	1685	Two mica granite	36.05	-111.98
8	1680	Granite	36.04	-111.94
8	1662	two mica granite	36.10	-112.09
9	1430	Pegmatite	38.46	-105.51
9	1436	Amphibolite	37.92	-105.17
9	1435	Granite	37.92	-105.17
9	1749	Granite	37.92	-105.17
10	1453	Granodiorite	32.72	-108.51
10	1458	Amphibolite	32.66	-108.54
10	1471	Granodiorite	32.64	-108.55
10	1631	Gabbro	32.73	-108.70
10	1471	Granodiorite	32.72	-108.56
10	1458	Granite	32.64	-108.57
10	1460	Granite	32.64	-108.54
10	1459	Granite	32.72	-108.51
10	1453	Granite	32.49	-108.51
10	1457	Granite	32.46	-108.58
11	1447	Granodiorite	38.51	-106.33
11	1437	Granite	38.90	-106.63
11	1428	Granite	38.73	-106.76
12	1434	Unknown	39.00	-107.00
13	1741	Amphibolite	38.49	-107.21
13	1713	Granite	38.65	-107.85
13	1711	Granite	38.65	-107.85
13	1434	Granite	38.58	-107.72
13	1413	Granite	38.58	-107.72
13	1741	Amphibolite	38.33	-107.27
14	1656	Granodiorite	34.58	-106.50
14	1427	Quartz Monzonite	34.50	-106.50
15	1781	Granite	38.08	-107.05
15	1770	Rhyolite	38.10	-107.05
15	1766	Rhyolite	38.20	-107.17
15	1766	Rhyolite	38.20	-107.17
15	1759	Rhyolite	38.25	-107.17
15	1757	Granite	38.31	-107.14
15	1751	Granite	38.11	-107.03
15	1742	Rhyolite	38.30	-106.75
15	1740	Rhyolite	38.30	-106.75
15	1733	Rhyolite	38.50	-106.78
15	1730	Rhyolite	38.50	-106.92
15	1730	Quartz Diorite	38.30	-106.92
15	1721	Granite	38.42	-106.92
15	1714	Tonalite	38.30	-106.83

15	1700	Granite	38.30	-107.02
15	1676	Granite	38.67	-106.02
15	1672	Granite	38.52	-106.00
15	1728	Dacite	38.52	-106.00
16	1685	Granite	36.05	-111.67
16	1670	Granite	36.05	-111.67
17	1693	Granite	36.55	-106.08
17	1693	Granite	36.55	-106.08
17	1631	Granite	36.55	-106.08
17	1700	Granite	36.00	-105.50
17	1693	Granite	36.00	-105.50
17	1693	Granite	36.00	-105.50
17	1633	Granite	36.00	-105.50
18	1770	Rhyolite	38.33	-107.17
18	1766	Rhyolite	38.33	-107.17
18	1766	Rhyolite	38.33	-107.17
18	1765	Rhyolite	38.25	-107.17
18	1757	Granite	38.33	-107.25
18	1751	Granite	38.30	-107.23
18	1745	Rhyolite	38.63	-106.60
18	1742	Rhyolite	38.50	-106.75
18	1740	Rhyolite	38.50	-106.75
18	1730	Quartz Diorite	38.56	-107.00
18	1728	Dacite	38.63	-105.92
18	1728	Rhyolite	38.38	-107.25
18	1713	Tonalite	38.46	-106.83
18	1713	Rhyodacite	38.50	-105.88
18	1701	Granite	38.63	-106.63
18	1676	Granite	38.38	-106.75
18	1672	Granite	38.72	-105.95
18	1668	Rhyodacite	38.49	-105.90
19	1770	Rhyolite	38.83	-106.63
19	1759	Rhyolite	38.38	-107.02
19	1733	Rhyolite	38.56	-106.83
19	1706	Granite	38.58	-105.32
19	1705	Granite	38.55	-105.45
19	1700	Granite	38.51	-106.98
19	1694	Charnokite	38.27	-105.33
19	1666	Granodiorite	38.48	-105.62
19	1665	Granodiorite	38.72	-105.25
19	1663	Leucogranite	38.55	-105.47
19	1653	Tonalite	38.22	-105.37
19	1622	Tonalite	38.21	-105.35
19	1615	Granite	34.21	-105.35
19	1486	Granite	38.00	-105.21
19	1474	Monzogranite	38.47	-105.59
19	1460	Quartz Monzonite	38.40	-105.70
19	1442	Granite	38.38	-105.27
19	1441	Granite	35.20	-105.17
19	1439	Granite	38.38	-105.25

19	1371	Granite	38.08	-105.05
19	1362	Granite	38.10	-105.08
19	1359	Granite	38.22	-105.28
20	1720	Quartz Monzonite	36.55	-105.43
21	1694	Granite	36.63	-108.90
21	1412	Granite	37.08	-109.42
21	1691	Granite	36.63	-108.90
22	1755	Granodiorite	30.52	-106.13
22	1700	Unknown	36.12	-106.62
22	1700	Rhyolite	36.62	-106.25
22	1460	Quartz Monzonite	35.76	-106.62
22	1120	Diabase	33.52	-110.88
23	1700	Granite	36.46	-106.06
23	1693	Granite	36.59	-106.17
23	1693	Granite	36.47	-106.08
23	1751	Granodiorite	30.52	-106.13
24	1750	Quartz Diorite	36.50	-105.40
24	1741	Gabbro	36.53	-105.47
24	1730	Quartz Monzonite	36.57	-105.60
24	1699	Quartz Monzonite	36.53	-105.38
24	1679	Granodiorite	36.80	-105.55
24	1644	Quartz Monzonite	36.83	-105.39
25	1749	Quartz Diorite	37.58	-105.50
25	1745	Diorite	37.56	-105.52
25	1732	Quartz Diorite	37.51	-105.53
25	1728	Gabbro	37.51	-105.49
25	1696	Gneiss	37.82	-105.47
26	1716	Granodiorite	38.38	-107.25
26	1711	Pegmatite	38.38	-107.25
26	1434	Monzogranite	38.58	-107.75
26	1413	Pegmatite	38.58	-107.75
27	1730	Quartz Monzonite	36.11	-106.63
28	1720	Rhyolite	35.67	-105.82
28	1650	Granite	35.68	-105.78
28	1480	Granite	35.75	-105.80
29	1703	Grantie	36.30	-105.25
29	1423	Pegmatite	36.78	-105.53
29	1420	Amphibolite	36.78	-105.52
29	1380	Amphibolite	36.62	-105.52
30	1700	Granite	37.75	-107.70
31	1691	Quartz Porphyry	35.90	-105.75
32	1682	Granite	36.02	-105.45
32	1421	Migmatite	36.08	-105.38
33	1689	Granodiorite	36.39	-105.58
34	1684	Granite	36.15	-105.86
34	1674	Quartz Monzonite	36.14	-105.86
35	1680	Rhyolite	34.60	-106.45
35	1664	Rhyolite	34.12	-107.03
35	1664	Rhyolite	34.12	-107.03
35	1659	Granite	34.11	-107.05

35	1654	Granite	34.10	-107.06
35	1648	Granite	34.10	-107.04
36	1662	Rhyolite	34.28	-106.53
36	1660	Amphibolite	34.25	-106.60
36	1658	Granite	34.25	-106.58
36	1655	Granite	34.26	-106.60
37	1660	Quartz Porphyry	35.65	-105.83
38	1658	Quartz Monzonite	34.36	-107.06
38	1658	Granite	34.36	-107.06
39	1655	Granite	32.97	-107.73
39	1445	Granite	32.32	-108.58
40	1655	Quartz Monzonite	35.17	-108.13
40	1655	Granite	35.00	-108.02
41	1650	Granite	35.70	-105.75
42	1650	Metavolcanic	32.92	-106.57
42	1630	Granite	33.05	-106.07
43	1643	Quartz Monzonite	36.88	-105.52
44	1633	Gabbro	32.68	-108.73
44	1465	Minette	32.68	-108.65
44	1461	Granite	32.68	-108.65
44	1231	Anorthosite	32.72	-108.73
44	1223	Anorthosite	32.72	-108.73
44	1220	Anorthosite	32.72	-108.73
45	1632	Quartz Monzonite	32.82	-106.51
45	1462	Granite	32.50	-106.39
45	1111	Rhyolite	31.25	-105.00
46	1437	Granite	35.08	-106.48
47	1430	Quartz Monzonite	36.38	-105.25
48	1382	Rhyolite	31.25	-105.00
48	1333	Rhyolite	31.25	-105.02
48	1325	Rhyolite	31.25	-105.02
48	1272	Rhyolite	31.25	-105.03
48	1260	Rhyolite	31.25	-105.02
48	1256	Rhyolite	31.25	-105.02
48	1251	Rhyolite	31.25	-105.02
48	1243	Rhyolite	31.25	-105.02
48	1120	Granite	31.25	-105.00
49	1380	Rhyolite	31.26	-105.00
50	1366	Gneiss	31.20	-103.50
50	1272	Gneiss	31.17	-103.50
51	1163	Amphibolite	32.42	-104.00
52	1700	Rhyolite	35.20	-106.27
52	1669	Granite	35.23	-106.25
52	1659	Granite	35.01	-106.50
52	1659	Granite	34.78	-106.42
52	1653	Granite	35.42	-106.43
52	1645	Granite	34.95	-106.43
52	1643	Granite	34.43	-106.50
52	1438	Granite	34.43	-106.48
53	1110	Alkali-feldspar granite	31.85	-106.55

53	1078	Alkali-feldspar granite	32.75	-99.50
53	1080	Quartz Diorite	35.37	-102.30
54	1380	Quartz Monzonite	35.67	-101.75
54	1372	Quartz Monzonite	35.68	-101.77
54	1355	Quartz Monzonite	35.73	-101.80
54	1370	Granite	32.38	-103.10
54	1372	Granodiorite	36.50	-103.57
54	1369	Granite	36.50	-103.57
54	1359	Granite	35.78	-101.83
54	1363	Rhyolite	35.78	-101.83
54	1383	Granite	33.00	-101.50
54	1359	Granite	35.78	-101.83
54	1348	Granite	35.67	-101.63
54	1341	Granite	35.67	-101.63
54	1339	Quartz Syenite	35.67	-101.75
54	1320	Meta-arkose	35.10	-104.10
55	1706	Granodiorite	38.58	-105.30
55	1698	Granodiorite	35.56	-105.30
55	1436	Pegmatite	38.56	-105.30
56	1740	Unknown	34.57	-113.25
56	1720	Rhyolite	34.55	-113.25
56	1720	Granodiorite	34.55	-113.25
57	1709	Rhyolite	34.43	-113.28
57	1706	Granodiorite	34.24	-113.42
57	1696	Granite	34.27	-113.42
58	1800	Rhyolite	34.75	-112.10
58	1755	unknown	34.30	-112.59
58	1750	Granodiorite	34.28	-112.37
58	1740	Granodiorite	34.55	-112.11
58	1740	Quartz Diorite	34.53	-112.47
59	1750	Granodiorite	34.28	-112.13
59	1740	Granodiorite	34.25	-112.09
59	1699	Quartz Monzonite	34.25	-112.25
60	1720	Quartz Diorite	34.45	-113.28
61	1680	Quartz Monzonite	34.13	-112.27
62	1738	Unknown	34.13	-111.28
62	1710	unknown	34.12	-111.08
62	1700	Rhyolite	33.93	-111.50
62	1703	Rhyolite	34.25	-111.25
62	1697	Rhyolite	34.23	-111.13
63	1710	unknown	34.00	-111.33
63	1710	unknown	33.94	-111.50
63	1695	Rhyolite	33.93	-111.50
63	1695	Rhyolite	33.93	-111.50
64	1695	Rhyolite	34.12	-111.08
64	1710	Granite	34.25	-111.25
64	1630	Grantie	34.04	-110.95
65	1640	Granite	33.85	-111.50
66	1638	Monzogranite	33.18	-111.70
66	1625	Monzogranite	33.47	-111.54

66	1633	Monzogranite	33.69	-111.50
66	1423	Granite	33.74	-111.85
66	1400	Granodiorite	33.77	-113.35
66	1400	Granite	33.79	-113.41
66	1634	Orthogneiss	33.09	-113.63
67	1328	Rhyolite	33.52	-110.89
68	1695	Monzogranite	38.05	-105.73
68	1693	Tonalite	38.05	-105.73
68	1407	Pegmatite	38.05	-105.74
68	1682	Quartz Monzonite	38.00	-105.68
68	1760	Amphibolite	37.99	-105.66
68	1425	Amphibolite	37.99	-105.66
68	1434	Quartz Monzonite	37.92	-105.50
68	1434	Pegmatite	37.92	-105.50
68	1706	Granodiorite	38.55	-105.25
68	1698	Granodiorite	38.55	-105.25
68	1430	Pegmatite	38.45	-105.52
68	1679	Granite	38.18	-105.17
68	1436	Amphibolite	37.92	-105.17
68	1435	Granite	37.92	-105.17
68	1749	Granite	37.92	-105.17
69	1718	Rhyolite	34.48	-113.28
69	1721	Rhyolite	34.48	-113.28
69	1711	Gabbro	34.46	-113.43
69	1706	Granite	34.46	-113.43
69	1696	Granite	34.56	-113.52
69	1686	Granite	34.41	-113.22
69	1677	Tonalite	34.47	-113.25
69	1410	Granite	34.45	-113.63
69	1410	Granodiorite	34.49	-113.53
69	1418	Granite	34.41	-113.25
69	1414	Granite	34.28	-113.04
69	1414	Granite	34.45	-112.98
69	1418	Granite	34.47	-113.32
70	1705	Migmatite	32.68	-108.52
70	1666	Quartz Monzonite	32.61	-106.46
70	1652	Gneiss	32.15	-107.65
70	1632	Granite	32.84	-106.57
70	1622	Gneiss	32.60	-106.47
70	1631	Metavolcanic	32.72	-108.57
71	1401	granite	34.28	-114.15
71	1700	granite gneiss	33.85	-115.68
71	1400	granite	35.02	-114.95
71	1700	biotite schist	33.62	-115.45
71	1200	syenite	33.78	-115.57
71	1750	augen gneiss	34.32	-114.32
71	1750	augen gneiss	34.67	-115.20
71	1800	augen gneiss	36.07	-117.12
71	1760	schist	34.75	-115.10
71	1700	gneiss	34.20	-114.78

71	1450	granite	35.22	-114.60
71	1425	granite	36.25	-114.22
71	1425	granite	35.32	-114.75
71	1367	granite	35.10	-113.90
71	1367	granite	34.90	-114.00
71	1670	diorite	36.20	-112.33
71	1670	granite	36.08	-112.07
71	1760	granite gneiss	36.20	-112.45
71	1670	2-mica granite	36.10	-112.10
71	1740	granodiorite	34.55	-112.43
71	1740	gneiss	34.62	-113.22
71	1730	granodiorite	34.55	-112.13
71	1730	granodiorite	34.53	-112.13
71	1700	gneiss	34.57	-114.12
71	2400	granite	41.32	-106.75
71	1800	gneiss	41.10	-106.52
71	1800	rhyodacite	39.78	-105.33
71	1800	tholeite	39.68	-105.47
71	1800	dacite	37.63	-107.72
71	1670	granodiorite	36.93	-106.30
71	1670	granodiorite	39.95	-105.38
71	1670	granodiorite	38.42	-105.47
71	1670	granite	41.10	-106.20
71	1430	2-mica granite	40.23	-105.40
71	1415	2-mica granite	38.50	-107.00
71	1415	2-mica granite	41.23	-105.30
71	1415	granite	39.68	-105.85
71	1440	monzogranite	32.65	-110.80
71	1700	biotite gneiss	35.07	-115.37
71	1700	garnet gneiss	35.07	-115.37
71	1437	granite	35.30	-106.43
71	1360	granite	34.63	-113.15
71	1400	granite	34.60	-112.42
72	1634	Quartz Porphyry	32.23	-109.54
72	1647	Rhyolite	32.30	-109.78
72	1615	Granite	32.68	-110.04
72	1640	Granite	32.84	-110.76
72	1654	Rhyolite	32.11	-110.11
72	1643	Granodiorite	32.19	-110.22
72	1442	Granite	32.05	-110.42
72	1428	Quartz Monzonite	32.05	-110.41
72	1645	Granite	32.99	-112.52
72	1647	Granite	33.28	-112.65

Appendix 2

Ref		
1	Aleinikoff *et al.*	1993
2	Bickford *et al.*	2008
3	Chamberlain and Bowring	1990
4	Gonzales and Van Schmus	2007
5	Duebendorfer *et al.*	2001
6	Reed *et al.*	1987
7	Ferguson *et al.*	2004
8	Hawkins *et al.*	1996
9	Jones *et al.*	2010a
10	Amato *et al.*	2011
11	Jones *et al.*	2010b
12	Leader and Jones	2008
13	Jessup *et al.*	2006
14	Bauer *et al.*	1993
15	Bickford and Boardman	1984
16	Hawkins and Bowring	1997
17	Davis *et al.*	2011
18	Bickford *et al.*	1989a
19	Bickford *et al.*	1989b
20	Bowring *et al.*	1992
21	Condie *et al.*	1999
22	Silver	1984
23	Davis *et al.*	2001
24	Bowring *et al.*	1984
25	Sabin	1994
26	Jessup *et al.*	2005
27	Woodward	1987
28	Robertson and Condie	1989
29	Pedrick *et al.*	1998
30	Silver and Barker	1968
31	Grambling and Dallmeyer	1988
32	Read *et al.*	1999
33	Reed	1984
34	Bell	1985
35	Bowring *et al.*	1983
36	Shastri	1993
37	Renshaw	1984
38	Pollock *et al.*	1994
39	Stacey and Hedlund	1983
40	Bowring and Condie	1982
41	Fulp	1982
42	Vollbrecht	1997
43	Lipman and Reed	1989
44	Ramo *et al.*	2003
45	Roths	1991
46	Kirby *et al.*	1995
47	Grambling and Dallmeyer	1992
48	Bickford *et al.*	2000

49	Copeland and Bowring	1988
50	Reese *et al.*	2000
51	Keller *et al.*	1989
52	Karlstrom *et al.*	2004
53	Li *et al.*	2007
54	Barnes *et al.*	2002
55	Jones *et al.*	2009
56	Silver	1967
57	Bryant and Wooden	1986
58	Anderson and Silver	1976
59	Karlstrom *et al.*	1987
60	Bowring *et al.*	1986
61	Blacet *et al.*	1971
62	Silver *et al.*	1986
63	Ludwig	1974
64	Conway	1976
65	Silver	1965
66	Isachsen *et al.*	1999
67	Stewart *et al.*	2001
68	Davis *et al.*	2005
69	Bryant *et al.*	2001
70	Amato *et al.*	2008
71	DePaolo *et al.*	1991
72	Eisele and Isachsen	2001

Appendix 3

```
import matplotlib.pyplot as plt
import mpl_toolkits.basemap as bm
import numpy as np
import os
import scipy
from scipy import stats
import csv
from scipy.stats.stats import pearsonr

os.chdir(u'C:\\Documents and Settings\\Sander\\My Documents\\Dropbox\\age_plot')

def distance_haversine(point1, point2, radius=6371e3):
    """ calculate the haversine distance between points (lon,lat)
    ~3m accuracy over 1km
    distance formulas from:
    http://www.movable-type.co.uk/scripts/latlong.html
    """
    #NOTE: can probably use gdal or google earth api's as well, GE apparently uses Re=6,378,137m
    lon1, lat1 = np.radians(point1)
    lon2, lat2 = np.radians(point2)

    dlat = lat2 - lat1
    dlon = lon2 - lon1
    a = np.sin(dlat/2)**2 + (np.cos(lat1) * np.cos(lat2) * np.sin(dlon/2)**2)
    distance = 2 * radius * np.arctan2(np.sqrt(a), np.sqrt(1-a))

    return distance


def distance_cyl(point1, point2, radius=6371e3):
    """ equirectangular projection (pythogorean theorem w/ effective cartesian
    coordinates. Fine for 'small' distances (depends also on bearing & latitude)
    Basemap 'cyl' projection
    """
    #NOTE: km2mi = 1/1.609344
    #km2Nmi = 1/1.852 #nautical mile
    lon1, lat1 = np.radians(point1)
    lon2, lat2 = np.radians(point2)

    x = (lon2 - lon1) * np.cos((lat1+lat2)/2)
    y = lat2 - lat1

    distance = np.hypot(x,y) * radius

    return distance


def bearing(point1, point2):
    """ Calculate initial bearing (forward azimuth) of great circle arc
    bearing from true North (theta=0)"""
    lon1, lat1 = np.radians(point1)
    lon2, lat2 = np.radians(point2)
    dlat = lat2 - lat1
```

```
    dlon = lon2 - lon1

    y = np.sin(dlon)*np.cos(lat2)
    x = np.cos(lat1)*np.sin(lat2) - np.sin(lat1)*np.cos(lat2)*np.cos(dlon)
    bearing = np.arctan2(y, x) #in radians (-pi, pi)

    bearingDeg = (np.degrees(bearing) + 360) % 360
    #NOTE back azimuth conversion backDeg = (bearing + 180) % 360

    return bearingDeg


def cross_track(start, end, point, radius=6371e3, dist='cyl'):
    """ distance from point to great circle path (aka 'cross-track error')
    start = p1, end = p2, point = p3 (lon,lat) degrees
    NOTE: negative implies to the west of the line
    """
    if dist=='haversine':
        d13 = distance_haversine(start, point,radius=radius)
    elif dist=='cyl':
        d13 = distance_cyl(start,point,radius=radius)

    theta13 = np.radians(bearing(start,point))
    theta12 = np.radians(bearing(start,end))

    distance = radius * np.arcsin(np.sin(d13/radius)* sin(theta13-theta12))

    return distance

# Load data
ages,errors,lats,lons = np.loadtxt('con_ages2.csv',delimiter=',',skiprows=1,unpack=True)

"""
now repeat the routine, but first build lists for age and distance separated by: 1. age (over 1500 or under
1500)
and 2. distance (in Arizona vs NM)
"""

ages_under_1500 = []
ages_over_1500 = []
distances_under_1500ma = []
distances_over_1500ma = []
lons_under_1500 = []
lons_over_1500 = []
lats_under_1500 = []
lats_over_1500 = []
errors_over_1500 = []
errors_under_1500 = []

"""
Define points for Picuris Orogeny
"""

popt1 = (-114.0,33.0)
popt2 = (-107,37.2)
popt3 = (-104.5,37.8)
```

```
"""
Determine distance from each portion of the Orogeny line defined above
"""

dis1_2 = []
dis2_3 = []

for i in range (ages.size):
   point = (lons[i], lats [i])
   dis1_2.append(cross_track(popt1,popt2,point) / 1e3)
   dis2_3.append(cross_track(popt2,popt3,point) / 1e3)

dis = np.zeros_like(ages)

"""
Make array of the shortest distances from the Orogeny
"""

for i in range(size(ages)):
   A = [] #reset A each time. Just in case.
   A = [dis1_2[i], dis2_3[i]]
   B = [] #reset B each time. Just in case.
   B = [abs(dis1_2[i]), abs(dis2_3[i])]
   for j in range(size(A)):
      if B[j] == min(B):
         dis[i] = A[j]

"""
Now separate out the ages by those over 1500 Ma and those under 1500 Ma
"""

ind_ov_1500 = (ages >= 1500)
ind_un_1500 = (ages < 1500)
distances_over_1500ma = dis[ind_ov_1500]
distances_under_1500ma = dis[ind_un_1500]
ages_under_1500 = ages[ind_un_1500]
ages_over_1500 = ages[ind_ov_1500]
lats_under_1500 = lats[ind_un_1500]
lats_over_1500 = lats[ind_ov_1500]
lons_under_1500 = lons[ind_un_1500]
lons_over_1500 = lons[ind_ov_1500]
errors_under_1500 = errors[ind_un_1500]
errors_over_1500 = errors[ind_ov_1500]

"""
Index for ages between 1400 and 1500 Ma
"""
ind_bet = (ages > 1400)&(ages < 1500)
dis_bet = dis[ind_bet]
ages_bet = ages[ind_bet]
lats_bet = lats[ind_bet]
lons_bet = lons[ind_bet]
errs_bet = errors[ind_bet]

"""
```

```
Plot Everything
"""

"""
All data
"""
#Data on US map
plt.figure()
LL = (min(lons)-1, min(lats)-1)
UR = (max(lons)+1, max(lats)+1)
bmap = bm.Basemap(projection='cyl',
            llcrnrlat=LL[1],
            urcrnrlat=UR[1],
            llcrnrlon=LL[0],
            urcrnrlon=UR[0],
            resolution='i',
            suppress_ticks=False)
bmap.drawcountries(linewidth=1.5)
bmap.drawstates()
sc = bmap.scatter(lons,lats,c=ages,cmap=plt.cm.gray)
bmap.colorbar(sc)
plt.title('Plutons in SW United States with Picuris Orogeny')
bmap.plot([popt1[0], popt2[0]], [popt1[1], popt2[1]], 'r.-', label='MZ def front 1')
bmap.plot([popt2[0], popt3[0]], [popt2[1], popt3[1]], 'r.-', label='MZ def front 2')

# plot separated ages vs distance from orogeny
plt.figure()
plt.plot(dis, ages,'b.')
plt.ylabel('Age [Ma]')
plt.xlabel('Distance from deformation Orogeny [km]')
plt.title('All ages vs Orogeny')
plt.grid()

"""
Ages Over 1500
"""
#Data on US map
plt.figure()
LL = (min(lons)-1, min(lats)-1)
UR = (max(lons)+1, max(lats)+1)
bmap = bm.Basemap(projection='cyl',
            llcrnrlat=LL[1],
            urcrnrlat=UR[1],
            llcrnrlon=LL[0],
            urcrnrlon=UR[0],
            resolution='i',
            suppress_ticks=False)
bmap.drawcountries(linewidth=1.5)
bmap.drawstates()
sc = bmap.scatter(lons_over_1500,lats_over_1500,c=ages_over_1500,cmap=plt.cm.gray)
bmap.colorbar(sc)
plt.title('Plutons over 1500 Ma in SW United States with Picuris Orogeny')
bmap.plot([popt1[0], popt2[0]], [popt1[1], popt2[1]], 'r.-', label='MZ def front 1')
bmap.plot([popt2[0], popt3[0]], [popt2[1], popt3[1]], 'r.-', label='MZ def front 2')

# plot separated ages vs distance from Orogeny
```

```
# distances over 1500
plt.figure()
plt.plot(distances_over_1500ma, ages_over_1500,'b.')
plt.ylabel('Age [Ma]')
plt.xlabel('Distance from deformation Orogeny [km]')
plt.title('Ages over 1500 ma vs distance from Orogeny')
plt.grid()
slope_ov, intercept_ov, r_value_ov, p_value_ov, std_err_ov =
stats.linregress(distances_over_1500ma,ages_over_1500)
r_sq_ov_1500 = r_value_ov**2
x1=min(distances_over_1500ma)
x2=max(distances_over_1500ma)
x = np.r_[x1:x2:6*1j]
plt.plot(x,slope_ov*x + intercept_ov,'k-')

"""
Ages between 1400Ma & 1500Ma
"""
#Data on US map
plt.figure()
LL = (min(lons_bet)-1, min(lats_bet)-1)
UR = (max(lons_bet)+1, max(lats_bet)+1)
bmap = bm.Basemap(projection='cyl',
            llcrnrlat=LL[1],
            urcrnrlat=UR[1],
            llcrnrlon=LL[0],
            urcrnrlon=UR[0],
            resolution='i',
            suppress_ticks=False)
bmap.drawcountries(linewidth=1.5)
bmap.drawstates()
sc = bmap.scatter(lons_bet,lats_bet,c=ages_bet,cmap=plt.cm.gray)
bmap.colorbar(sc)
plt.title('Plutons between 1400 and 1500 Ma in SW United States with Picuris Orogeny')
bmap.plot([popt1[0], popt2[0]], [popt1[1], popt2[1]], 'r.-', label='PO def front 1')
bmap.plot([popt2[0], popt3[0]], [popt2[1], popt3[1]], 'r.-', label='PO def front 2')

# plot separated ages vs distance from Orogeny
# distances under 1500
plt.figure()
plt.plot(dis_bet, ages_bet,'b.')
plt.ylabel('Age [Ma]')
plt.xlabel('Distance from deformation Orogeny [km]')
plt.title('Ages under 1500 ma vs distance from Orogeny')
plt.grid()
slope_bet, intercept_bet, r_value_bet, p_value_bet, std_err_bet = stats.linregress(dis_bet,ages_bet)
r_sq_bet = r_value_bet**2
x1=min(dis_bet)
x2=max(dis_bet)
x = np.r_[x1:x2:6*1j]
plt.plot(x,slope_bet*x + intercept_bet,'k-')

# Determine the statistical significance of the relationship between the ages and distances
ov_1500_PCC,ov_1500_PCCp = pearsonr(distances_over_1500ma,ages_over_1500) #ages over 1500 and
distances from the PO
```

```
bet_1500_PCC,bet_1500_PCCp = pearsonr(dis_bet,ages_bet) #ages betwee 1500 and 1400 Ma and distances from the PO

bet_PO = zip(dis_bet,ages_bet)
all_PO = zip(dis, ages)
```